UNIVERSITÀ DEGLI STUDI DI MILANO
FACOLTÀ DI SCIENZE MATEMATICHE, FISICHE E NATURALI
DIPARTIMENTO DI FISICA

CORSO DI DOTTORATO DI RICERCA IN
FISICA, ASTROFISICA E FISICA APPLICATA
CICLO XIX

TESI DI DOTTORATO DI RICERCA

DESIGN AND INTEGRATION OF SUPERCONDUCTING UNDULATORS FOR THE LHC BEAM DIAGNOSTICS

DOTT.SSA SIMONA BETTONI

SETTORE DISCIPLINARE FIS/01

TUTORE: PROF. GIOVANNI BELLOMO

COORDINATORE: PROF. GIANPAOLO BELLINI

ANNO ACCADEMICO 2005/2006

CONTENTS

INTRODUCTION

This work has been developed in the context of the studies for the Nb_3Sn upgrade of the superconducting undulator for the CERN Large Hadron Collider (LHC) beam diagnostics. In LHC the two-dimensional proton beam profile in the full energy range will be measured by a synchrotron light monitor system based on a dipole and a 5 T, 280 mm, two periods NbTi undulator. In case of lead ions beams this undulator is not suitable, because the emitted radiation would fall into the far infrared part of the electromagnetic spectrum and it couldn't be revealed by detectors. An undulator with a period of 140 mm would allow moving the emitted radiation in the near IR and in the visible part of the spectrum, making possible the measurement also on the lead ions beams. It has then been decided to design a new undulator to be used with a 280 mm period for protons and a 140 mm period for lead ions beams.

In the first chapter, after a brief remind to the synchrotron radiation theory and its use in the accelerators, the motivations which led to the specifications of the LHC undulator are presented.

In the second chapter the magnetic design of the undulator is presented. A first design with the coil axis parallel to the longitudinal dimension of the magnet has been discharged, because it does not allow to insert the undulator in a standard LHC dipole cryostat. The final design has the coils superimposed in two rows; the upper one producing a 280 mm and the lower a 140 mm period configuration. The optimization has been done in 2D and thereafter the 3D model has been simulated to take into account the finite dimensions of the coils and the yoke, to verify the impact of the field uniformity on the beam dynamics and to determine the fringe field seen by the other circulating beam.

Designing and building such magnet represent a challenge, because to provide 5 T in the 60 mm gap with the long period configuration requires field higher than 10 T on

the conductor at 4.2 K. At the operating temperature of 4.2 K it is impossible the use of NbTi (and also at 1.9 K with a safety margin), and therefore Nb_3Sn has been chosen as superconductor.

The ordered crystallographic structure, responsible of the superconducting properties of the Nb_3Sn, confers to it also brittleness. This imposes, except in rare cases, that the coils must be wound before the superconductor is formed by means of a heat treatment, which may also strongly influence the final strand properties. A description of the most important characteristics of this material, the manufacturing processes and the heat treatment to react the composite are presented in the third chapter.

The state of the art of this composite is the 0.8 mm diameter Restacked Rod Process, a kind of Internal Tin wire produced by the Oxford Instruments Superconducting Technology (OI-ST). This strand has been chosen as a reference for the upgrade of the LHC undulator. Because of the dependence of the final superconducting properties of the Nb_3Sn strand on the heat treatment, a consistent part of the experimental work, described in the fourth chapter, was about the calibration of the system to form the superconductor. In particular measurements of Residual Resistivity Ratio (RRR) and critical current density (J_C) have been performed at CERN in collaboration with the section AT/MAS-SC.

High critical current superconductors may suffer of flux jump instability, which can provoke they quench well below the critical surface of the material in the high J_C region. It is then mandatory to check that no part of the coils of the undulator fall in a region of instability during the ramping of the current or at the working points. The measurements to determine the region of instability eventually present have been performed at Laboratorio Acceleratori Superconduttività Applicata (LASA - INFN laboratory). This test indicated the presence of a region instable for flux jumping, which would not allow to manufacture the coils of the short period configuration of the undulator. The possibilities to modify the heat treatment to obtain a more stable strand and an alternative design limiting the current below the instability values have been considered.

As mini dipole split coils has been designed, manufactured and tested to verify the feasibility of the coil using the OI-ST wire (fifth chapter). The magnetic design has been optimized to reproduce the operational conditions of the coils of the undulator (similar magnetic field on the conductor, current and radius of curvature) and to test the connections, using a reasonably small amount of wire. During the first test

numerous quenches have been observed. The cause has been identified into the heat treatment to form the superconductor and a second test has been performed to verify this hypothesis and possibly solve the problem. During this test no mechanical or flux jumping instabilities have been detected, but a limitation in the quenching current did not allow to explore the region in the magnetic field-current plane necessary to demonstrate the feasibility of the coils of the undulator. The design of the undulator has been modified in case future measurements on the wire will evidence points of instability in the not-explored zone.

For all the considered design it was necessary to preview the behavior of the coils in case of quench, the transition from the superconducting to the normal conducting state. During this process a magnet can reach very high values of temperatures and voltages, because of the large energy stored in the coil. For this reason superconducting coils are normally inserted into a circuit of protection, a system of resistances and diodes, where a part of the energy is extracted and dissipated during a quench. To optimize and analyze the behavior of the entire system of protection I developed a finite difference simulating code. This program produces a mesh of the quenching coil and for each element solves the heat equation to find out the 3D temperature map, knowing the 3D map at the previous iteration. The code is capable of computing the current, the voltage developed and the dissipated energies in each element of the circuit of protection, the quench resistance and the propagation velocity in the longitudinal and in transverse directions. A detailed description of this code is given in the appendix A.

In parallel to this work I took part to collaboration, described in the appendix B, with the Laboratorio Nazionale Frascati (LNF - INFN Laboratory) for the reduction of the integrated octupole with respect to the beam trajectory of the eight normal conducting wigglers of the main ring in DAΦNE. The model I proposed and optimized, starting from an idea of the team of Frascati, allows to reduce the integrated octupole to the 3% of the present configuration. The optimized solution will be implemented on a spare wiggler this year and, if the field map will be confirmed, the solution will be implemented on the wigglers of the main ring before the end of 2007.

CHAPTER 1

LHC BEAM PROFILE MEASUREMENT BY SYNCHROTRON RADIATION MONITOR

"On April 24 1947 (Robert) Langmuir and I (Herb Pollock) were running the machine and as usual were trying to push the electron gun and its associated pulse transformer to the limit. Some intermittent sparking had occurred and we asked the technician to observe with a mirror around the protective concrete wall. He immediately signaled to turn off the synchrotron as "he saw an arc in the tube." The vacuum was still excellent, so Langmuir and I came to the end of the wall and observed … soon became clearer that we were seeing Ivanenko and Pomeranchuk radiation." [1]

The synchrotron radiation, experimentally observed for the first time in a 70 MeV General Electric electron synchrotron at New York in 1947, after having being theoretically foreseen in 1944 by Ivanenko and Pomeranchuk, has been regarded for several years only as a limiting factor for the construction of the circular machines for electrons, because of the energy loss. After that it has been realized that the synchrotron radiation can be also used to investigate the intrinsic properties of the materials and more than fifty "light sources" have been built worldwide .

Synchrotron radiation can also be a valid instrument in beam diagnostics. In LHC a monitor based on synchrotron radiation will be used to measure the 2D beam profile, useful to determine the beam emittance. A superconducting undulator will be used together with a dipole to perform the measurement on the protons beams in the whole

energy range. This undulator is not suitable for similar measurements on the lead ions beams, because the emitted radiation would fall in the far infrared part of the electromagnetic spectrum, and it couldn't be revealed. A way to overcome this limitation is to move the emitted radiation towards the visible part of the spectrum building a shorter period undulator. It has then be decided to design a new undulator to be used with a long period for the protons and a short period for the lead ions beams measurement.

After a brief remind to the synchrotron radiation theory, its use for the beam diagnostics and in particular for the LHC beams is presented.

1.1. The beam emittance

A beam oscillates around its nominal orbit according to the Hill equation:

$$u''+K(s)u=0 \qquad (1)$$

where s is the curvilinear coordinate, u is one of the transverse dimensions and *K*(s) is a periodic function given by the magnetic field gradient at the reference orbit.

The solution of eq. (1) is of the form:

$$u(s)=a\sqrt{\beta(s)}\cos[\mu(s)-S] \qquad (2)$$

where $\beta(s)$ and $\mu(s)$ are the betatron and the phase function respectively, a and S are two constants.

Starting from eq. (2) it can be proved that the quantity [2]:

$$\gamma(s)u^2(s)+2\alpha(s)u(s)u'(s)+\beta(s)u'^2(s)=a^2 \qquad (3)$$

is an invariant of the movement, where $\alpha(s)$, $\beta(s)$ and $\gamma(s)$ are the Twiss parameters. For a given position $\bar{s}$ the eq. (3) defines an ellipse of area πa^2 in the phase space $(u(\bar{s}),u'(\bar{s}))$, where $u'(\bar{s})$ is the derivative of $u(\bar{s})$ with respect to s. The ellipse of parameter a is the one which contains all the particles having an amplitude of betatron oscillation, at the specified s, less or equal to a. The quantity $\varepsilon \equiv a^2$, in case the ellipse of parameter a contains all the beam, is called edge-beam emittance. In the case of a gaussian , or gaussian like, distribution for the beam phase the rms beam emittance is normally defined.

In a non-dispersive region the root mean square of the beam dimension in horizontal (vertical), σ_H (σ_V), projection of the ellipse of the phase space, is related to the horizontal (vertical) betatron function and rms emittances by the relation:

$$\sigma_{H,V} = \sqrt{\beta_{H,V}\varepsilon_{H,V}} \tag{4}$$

Along the beam trajectory the ellipse in the phase space continuously changes shape and orientation, but the value of its area remains constant. It is then sufficient to measure the beam profile in a point of the machine to determine the emittance from eq. (4), knowning the betatron function.

As discussed in section 1.3.1. the beam profile will be measured by a synchrotron radiation monitor. Before describing it in details, a brief remind to the synchrotron radiation theory and the description of the several insertion devices to produce it will be given.

1.2. The synchrotron radiation

In this section only a short summary of the main steps in the derivation of the synchrotron radiation theory in case of point-like charge is described. A more detailed description can be found in several references, as [3], [4] for example. This simplified description is sufficient to determine the most important characteristics of the insertion devices useful to produce synchrotron radiation (short and long magnets and undulators and wigglers) and to discriminate their most important differences.

1.2.1. Theorical remind

An accelerated charge emits an electromagnetic radiation which propagates and is received by an observer in P, as schematically shown in Figure 1.

The magnetic and the electric field, $\vec{B}$ and $\vec{E}$ respectively, can be expressed in function of their potentials Φ and $\vec{A}$ as:

$$\begin{aligned} \vec{B} &= \vec{\nabla} \times \vec{A} \\ \vec{E} &= -\nabla\Phi - \frac{1}{c}\cdot\frac{\partial \vec{A}}{\partial t} \end{aligned} \tag{5}$$

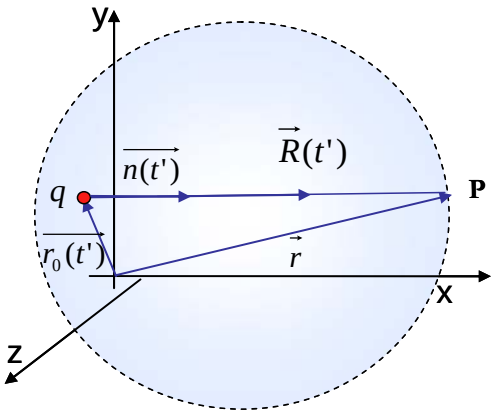

Figure 1. The accelerated charge q emits radiation received by an observer in P.

where c is the speed of the light and assuming the Lorentz gauge:

$$\nabla \cdot \vec{A} + \frac{1}{c^2} \cdot \frac{\partial \Phi}{\partial t} = 0 \tag{6}$$

from the Maxwell equations it can be derived that:

$$\begin{aligned} \nabla^2 \Phi - \frac{1}{c^2} \cdot \frac{\partial^2 \Phi}{\partial t^2} &= -\frac{\rho}{\varepsilon_0} \\ \nabla^2 \vec{A} - \frac{1}{c^2} \cdot \frac{\partial^2 \vec{A}}{\partial t^2} &= -\mu_0 J \end{aligned} \tag{7}$$

where c is the speed of light, μ_0 the permeability, ε_0 the permittivity in vacuum and the terms on the right represent the fields sources (charge and current densities).

In case of a point-like charge they are given by:

$$\begin{aligned} \rho(r,t) &= q \cdot \delta(\vec{r} - \overrightarrow{r_0(t')}) \\ J(r,t) &= q \cdot \overrightarrow{v(t')} \cdot \delta(\vec{r} - \overrightarrow{r_0(t')}) \end{aligned} \tag{8}$$

where $\delta(\vec{r} - \overrightarrow{r_0(t')})$ is the Dirac delta centered on the charge position at the emission time and $\overrightarrow{v(t')}$ is the charge velocity at the same time.

In this hypothesis the potentials (Lienard-Wiechert), given by:

$$\begin{aligned} \vec{A}(r,t) &= \frac{\mu_0}{4\pi} \cdot \left(\frac{q \cdot \vec{\beta}}{R - \vec{\beta} \cdot \vec{R}} \right)_{t'} \\ \Phi(r,t) &= \frac{1}{4\pi\varepsilon_0} \cdot \left(\frac{q}{R - \vec{\beta} \cdot \vec{R}} \right)_{t'} \end{aligned} \tag{9}$$

solve the eq. (8), where $\vec{\beta} \equiv \frac{\vec{v}}{c}$. The expressions on the right side of the eq. (9) are evaluated at the time t', given by:

$$t' = t - \frac{R}{c} \tag{10}$$

to take into account the time necessary for the emitted radiation to reach the observer in P at the time t. From the eq. (9) and by using the eq. (5) the fields can be expressed as:

$$\vec{E}(r,t) = \frac{q}{4\pi\varepsilon_0} \cdot \left[\frac{(n-\beta)\cdot(1-\beta^2)}{(1-\vec{n}\cdot\vec{\beta})^3 \cdot R^2} \right]_{t'} + \frac{q}{4\pi\varepsilon_0 c} \cdot \left[\frac{\vec{n} \times \left[(\vec{n}-\vec{\beta}) \times \dot{\vec{\beta}} \right]}{(1-\vec{n}\cdot\vec{\beta})^3 \cdot R} \right]_{t'} \tag{11}$$

$$\vec{B}(r,t) = \vec{n}(t') \times \frac{\vec{E}(r,t)}{c}$$

where $\dot{\vec{\beta}}$ is it's the time derivative of $\vec{\beta}$.

The emitted radiated power in the "far field" condition ($R \to \infty$) becomes:

$$\frac{dP}{d\Omega} = \frac{q^2}{16\pi^2\varepsilon_0 c} \cdot \left[\frac{\left| \vec{n} \times \left[(\vec{n}-\vec{\beta}) \times \dot{\vec{\beta}} \right] \right|^2}{(1-\vec{n}\cdot\vec{\beta})^6} \right]_{t'} \tag{12}$$

In relativistic case it can be shown that the radiation is emitted in a cone of opening angle equal to $1/\gamma$ around the charge velocity, where γ is the relativistic factor. This property is fundamental to understand the differences between the insertion devices presented in the next section.

1.2.2. Sources of synchrotron radiation

Synchrotron radiation can be produced making the charges traveling in a region where a magnetic field is generated by several kinds of magnets:

- Short magnets;
- Long magnets
- Periodic magnets, as undulators and wigglers.

For each kind of magnet the typical frequency of the emitted radiation in the relativistic limit will be determined.

A magnet is said long if its length L satisfies the condition:

$$L \geq \frac{2\rho}{\gamma} \tag{13}$$

where ρ is the radius of curvature of the beam trajectory. From simple geometric considerations it can be concluded that in this case an observer in P sees the radiation emitted when the charge travels in the central part of the magnet from A to A', subtended to an angle $1/\gamma$, as shown in Figure 2.

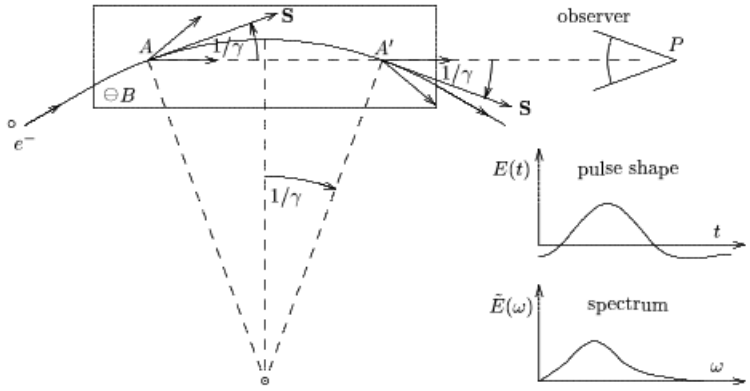

Figure 2. Emission of the radiation in a long magnet. The observer sees only the radiation emitted by the charge traveling between A and A'.

The time duration of the pulse, Δt, seen in P is given by the difference between the time that the electron spends to go from A to A', t_e, and the time which the radiation needs to reach the observer, t_{ph}, i.e. in relativistic condition:

$$\Delta t = t_e - t_{ph} \approx \frac{4\rho}{3c\gamma^3} \tag{14}$$

and the typical frequency can be estimated as:

$$\omega \approx \frac{2\pi}{\Delta t} = \frac{3\pi c\gamma^3}{2\rho} \tag{15}$$

In case of short magnet (Figure 3), i.e. a magnet which has a length $L < 2\rho/\gamma$, by analogous calculations it can be found that the typical frequency of emission is:

$$\omega \approx \frac{4\pi c\gamma^2}{L} \tag{16}$$

The bandwidth of the emitted radiation can then spread also over a very large range of frequencies, because of the dependence of ω on the third or the second power of the relativistic factor. In the case the power is broaden over a large range of frequencies the peak may be too small to be useful for the measurement.

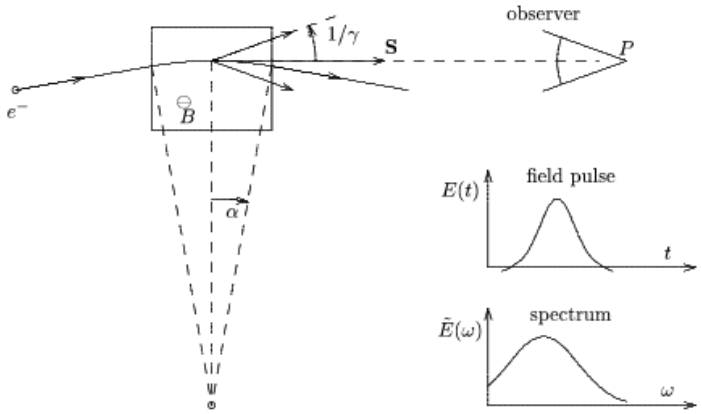

Figure 3. Emission of the radiation in a short magnet. The observer sees the radiation emitted by the charge traveling in the whole magnet.

A method to increase the power per unit of frequency is to reduce the spectral range by increasing the time duration of the collected radiation. A scheme to do this has been proposed by Motz in 1951: the undulator. It is a succession of magnets which produces a space sinusoidal field (Figure 4).

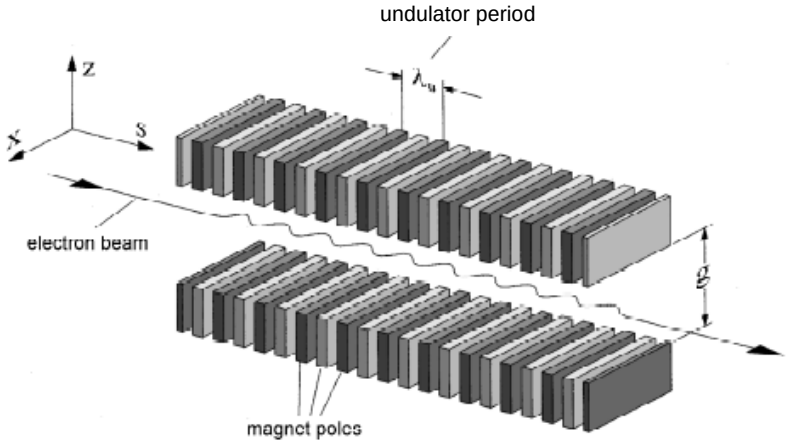

Figure 4. Typical layout of an undulator with a gap g and a period λ_U [5].

The motion of a relativistic charge in an undulator in the s-x plane, neglecting the vertical dimension, can be described by the equations:

$$\begin{cases} \ddot{x} = -\dot{s}\dfrac{q}{m\gamma}B_z(s) \\ \ddot{s} = -\dot{x}\dfrac{q}{m\gamma}B_z(s) \end{cases} \qquad (17)$$

where $B_z(s)$ is the vertical component of the magnetic field and the derivatives are respect to the time. The eq. (17) doesn't admit a simple analytic solution, but by

neglecting the variation of the longitudinal velocity $v_s >> v_x$, and assuming $v_s = \beta c = const.$, only the first equation of (17) is of interest, and it becomes:

$$\ddot{x} = -\dot{s}\frac{q}{m\gamma}B_z(s) = -\frac{\beta c q B_0}{m\gamma}\cos\left(\frac{2\pi}{\lambda_U}\cdot s\right) \qquad (18)$$

The magnetic field has been assumed a sinusoidal function of the space and B_0 is the maximum field along the axis of the undulator.

It is often more convenient to describe the motion of the charge as a function of the longitudinal coordinate s instead of the time, then eq. (18) becomes:

$$x'' = -\frac{qB_0}{m\beta c\gamma}\cos\left(\frac{2\pi}{\lambda_U}\cdot s\right) \qquad (19)$$

where x'' is the second order s-derivative of x. By integrating eq. (19) it is obtained that:

$$x' = -\frac{\lambda_U qB_0}{2\pi mc\gamma}\sin\left(\frac{2\pi}{\lambda_U}\cdot s\right) \qquad (20)$$

The maximum deflection angle of the particle, Θ_{MAX}, is then given by:

$$x'_{MAX} \equiv \Theta_{MAX} = \frac{\lambda_U qB_0}{2\pi mc}\cdot\frac{1}{\gamma} \equiv \frac{K}{\gamma} \qquad (21)$$

where the adimensional parameter K has been introduced.

It is used to discriminate undulators and wigglers: if K is less than 1 the magnet is an undulator, otherwise a wiggler.

In case of wiggler an observer on the axis sees the radiation emitted by the charge traveling only in the regions of the trajectory where the angle of deviation is smaller. The spectrum is a dipole-like one, but the intensity of the radiation is higher, because of the addition of the contributions of several poles.

In case of an undulator the maximum deflection angle of the particle trajectory is smaller than the opening one of the cone of the emitted radiation. An observer located on the axis then sees the radiation emitted by the charge traveling along the whole magnet. The radiation has a long time duration, which corresponds to a small spectral range with an intensity peak which can be also orders of magnitude higher than the one produced by the passage of the beam in a bending magnet.

The photons interfere at a wavelength which depends on the characteristics of the magnet and the beam. The wavelength of the constructive interference of the undulator can be determined from simply argumentations.

A charge moving at velocity $v = \beta c$ spends a time t_q, given by:

$$t_q = \frac{\lambda_U}{\beta c} \tag{22}$$

to cover a period of the undulator (Figure 5).

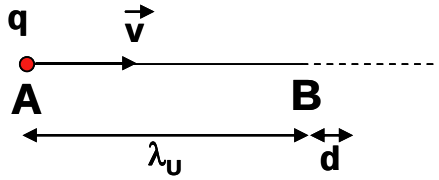

Figure 5. An electron moves from A to B, which corresponds to one period of the undulator.

During the same time the radiation emitted in A covers a distance z, given by:

$$z = c\,t_q = c\frac{\lambda_U}{\beta c} = \frac{\lambda_U}{\beta} \tag{23}$$

If the difference of the two path is equal to an integer numbers of wavelength λ, i.e.:

$$\frac{\lambda_U}{\beta} - \lambda_U = n\lambda \tag{24}$$

the radiation emitted in A at time t_0 constructively interferes with the one emitted in B at time $t_0 + t_q$.

In general if the observer is put at an angle θ with respect to the axis of the undulator, as shown in Figure 6, eq. (24) becomes:

$$\frac{\lambda_U}{\beta} - \lambda_U \cos(\theta) = n\lambda \tag{25}$$

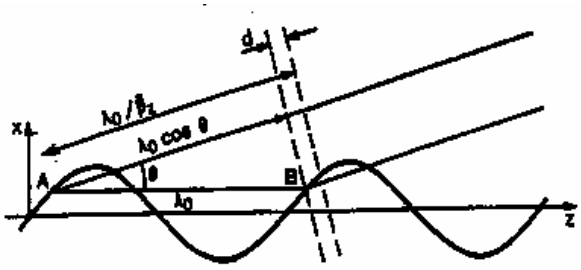

Figure 6. Interference in an undulator [6].

The wavelength can be expressed as [6]:

$$\lambda = \frac{\lambda_U}{2\gamma^2}\frac{1}{n}\left(1 + \frac{K^2}{2} + \gamma^2\theta^2\right) \tag{26}$$

where n is the harmonics number. The fundamental wavelength is very much shorter than the period of the undulator, because of the dependence on the factor γ^2, it is

function of both beam energy and the characteristics of the undulator (dependence on K), and it can be varied by changing the observation angle.

The angular spectral energy density is given by [6]:

$$\frac{d^2W}{d\Omega d\lambda} \propto B_0{}^2\left(\frac{\gamma}{1+\gamma^2\theta^2}\right)^6\left(1-\gamma^2\theta^2\right)^2\left(N_U\,\frac{\lambda_C}{\lambda}\right)^2 \sin c^2\left[\left(\frac{\lambda_C}{\lambda}-1\right)\pi N_U\right] \qquad (27)$$

It is proportional to the square of the magnetic field and decreases going away from the beam axis and the spectrum narrows when the number of periods N_U increases.

1.3. The beam diagnostics

Several kinds of beam diagnostics can be performed by using synchrotron radiation:

- Measurement of the beam cross section;
- Determination of the angular spread of the charges in the transverse dimension;
- Observation of the longitudinal charge distribution.

To measure the beam cross section the radiation emitted in a magnet passes through a lens, which forms an image of the source point on the detector (Figure 7).

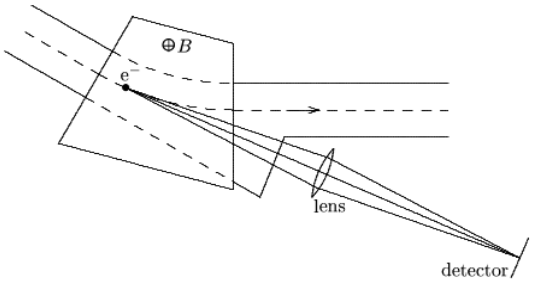

Figure 7. Measurement of the beam cross section by synchrotron radiation [7].

If a direct observation of the emitted radiation without using a lens is performed, also the angular distribution of the particles can be determined (Figure 8).

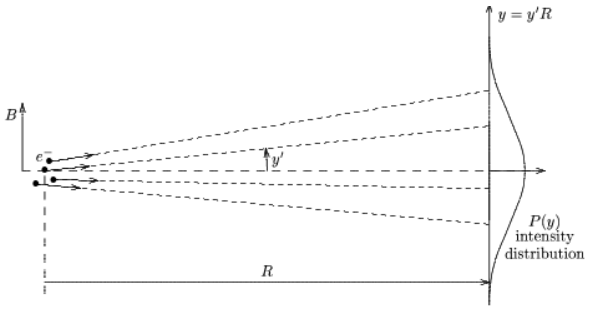

Figure 8. Determination of the angular charge distribution in the beam cross section by synchrotron radiation [7].

The longitudinal distribution of the particles can be instead determined by observing the temporal structure of the emitted radiation (Figure 9).

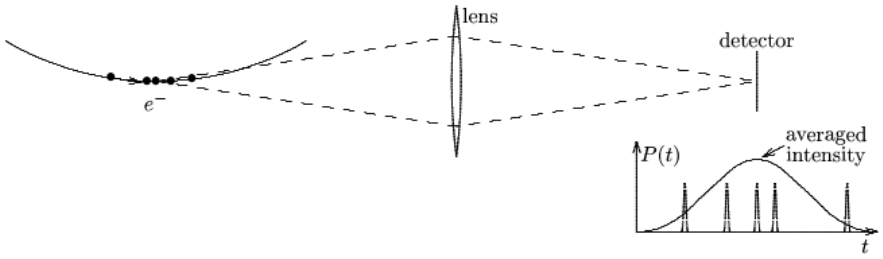

Figure 9. Observation of the longitudinal charge distribution by synchrotron radiation [7].

1.3.1. The beam diagnostics in LHC

The Large Hadron Collider (LHC) will be the world's largest and highest energy collider when opposite circulating proton beams will be accelerated from 450 GeV to 7 TeV. In the second operational phase heavy ions ($^{208}Pb^{82+}$) will be accelerate from 177.4 GeV/nucleon up to 2.78 TeV/nucleon. This collider should allow answering to some questions of the physics [8]:

- determine the existence of the Higg's boson, which would be able to proof the Higg's mechanism of the mass formation;
- give an indication of the rightness of the supersimmetry (SUSY) theory, recreating conditions similar to the ones of the Big Bang, allowing finding supersymmetric particles;
- help to solve the riddle of the antimatter.

The collider is contained in a 27 km circumference tunnel formerly used to house the LEP located underground at a depth ranging from 50 to 150 m and the trajectories of the two circulating beams will cross in four interaction points, in correspondence of the detectors indicated in Figure 10.

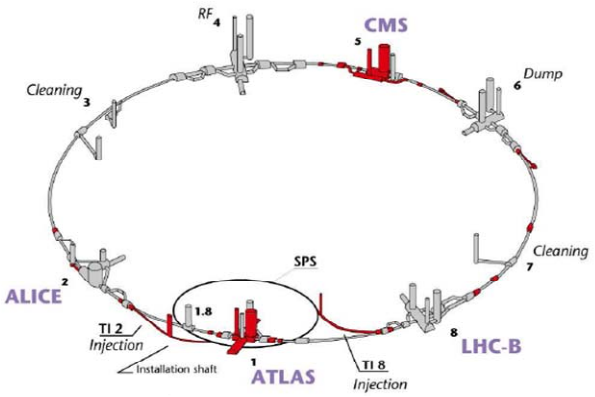

Figure 10. LHC layout. The location of the four detectors for the experiments is indicated.

Various methods have been considered to measure the beams transverse profile in LHC: the wire-scanners, the luminescence, the ionization and the synchrotron light profile monitors.

The wire-scanners exploit the low energy secondary electrons emitted by a wire crossed by the beam. These electrons can be measured from the generated current or by means of a scintillator. Study performed at CERN demonstrated that the LHC beams are too intense and their passage could cause the destruction of the wire [9].

In another method the beam is going through a vacuum chamber filled by a gas (nitrogen) [10]. As the beam passes in the chamber, the N_2 is ionized in N_2^+, which de-excite with the emission of photons of 391.4 nm wavelength. The observation of the photons allows measuring the beam profile, but it has a very low sensitivity.

A method which permits to have higher sensitivity is the Ionization Profile Monitor [11]. In this case the beam ionizes the residual gas (pressure10^{-10} mbar) of the vacuum chamber. The electrons and the ions, separated by an electric field, are guided by a magnetic field to a multichannel plate which multiplies the electrons, collected on a screen of phosphorus. This method may suffer of the space charge effect.

In LHC the beam profile measurement will be performed by means of a synchrotron radiation monitor. This system has also the advantages to be a not-intercepting device and the only one able to produce a 2D image of the beam, whereas the other ones give only its projection on the vertical or the horizontal dimension.

Two operational modes have been foreseen for the monitor: the “TV” and the “turn-by-turn” mode. In the first case the intensity of the emitted radiation is integrated over a long time (20 ms) to follow the evolution of the beam envelope. In this case the emitted radiation after the optics is directly revealed by a CCD camera. In the second

case the measurement is done at each turn, and then the evolution of a single bunch or batch can be determined. In this case an intensifier in front of the CCD camera will be used.

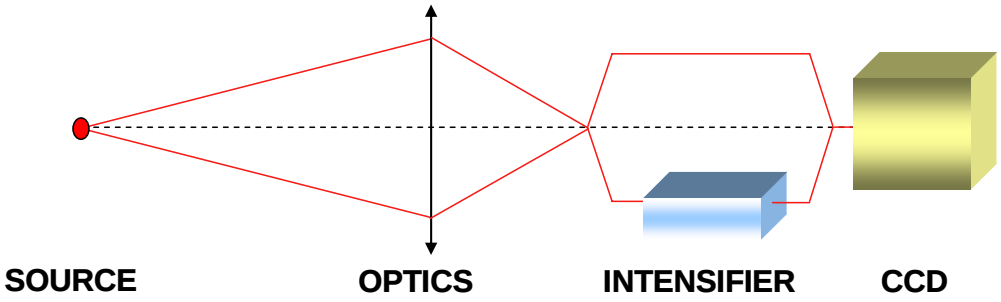

Figure 11. Experimental set-up for the two operational modes of the synchrotron radiation monitor.

The best placement of the transverse beam profile monitor is close to IR4 (Figure 11).

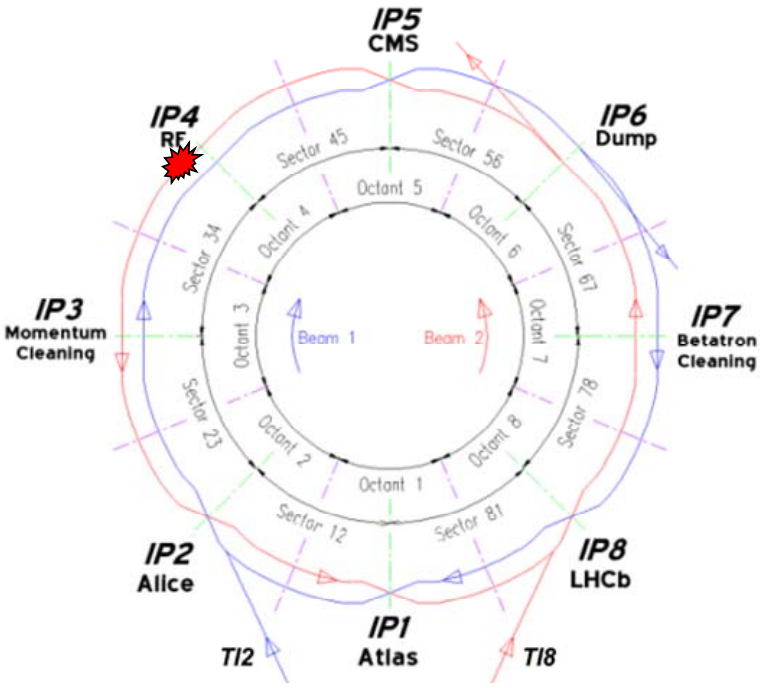

Figure 12. Location of the synchrotron radiation monitor for the LHC beam diagnostics.

This location has been chosen, because of the high value of the β function (β = 200 m) and because the beams are well separated (420 mm vs nominal 194 mm in the arc) for the insertion of RF system (Figure 14). The expected size at this location is σ_x = 1.2 mm for 450 GeV and σ_x = 300 μm for a 7 TeV beam.

From simulations the radiation emitted by the dipole (D3) in IR4 is sufficient to perform the measurement only for beam energy above 2 TeV. To cover the whole

energy range, a superconducting 5 T undulator, 280 mm of period had then been built (Figure 12).

Figure 13. NbTi undulator for the proton beam diagnostics.

The location of the NbTi undulator in the IR4 region is shown in Figure 14.

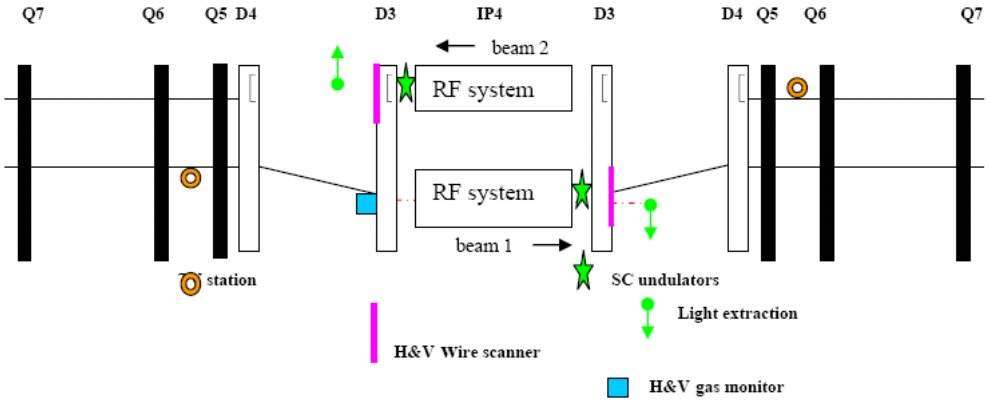

Figure 14. Layout for the transverse profile measurement (IR4) [12].

In Figure 15 the detail of the configuration is shown.

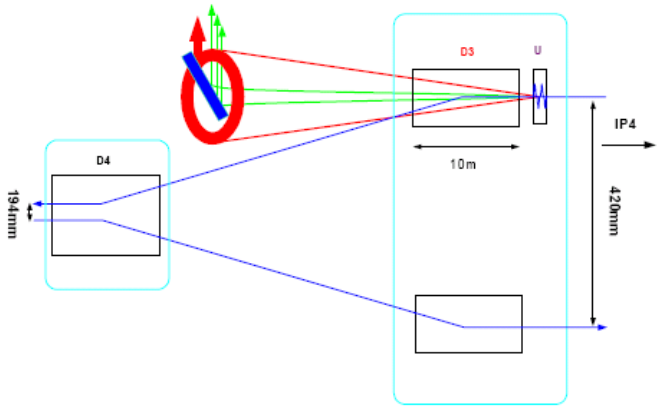

Figure 15. Detail of the layout for the profile beam measurement [13].

The D3 dipole and the undulator are inserted in the same cryostat to minimize their distance and then the extent of the light. The emitted radiation travels for 24 m before being intercepted by the detection system placed at a safe transverse distance from the beam ($15\sigma_H$).

For the lead ions beams at energy above 1 TeV/nucleon the radiation emitted by this undulator is below the sensor noise level (Figure 13), because the lead ions beams would emit in the far infrared.

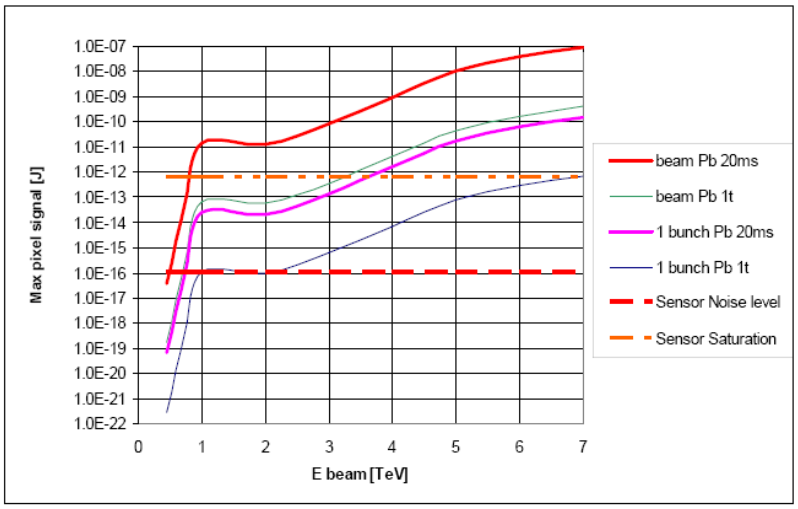

Figure 16. Estimated maximum synchrotron radiation signal emitted by lead ions beams in case of the use of the 280 mm, 5 T, 2 periods undulator for the beam and single bunch integrated over 20 ms, and single turn compared to the operational range of the detection system [14].

The strategy to overcome this is to consider a shorter period undulator. In particular by halving the period, the wavelength of the emitted radiation would be moved towards the visible part of the electromagnetic spectrum (Figure 17).

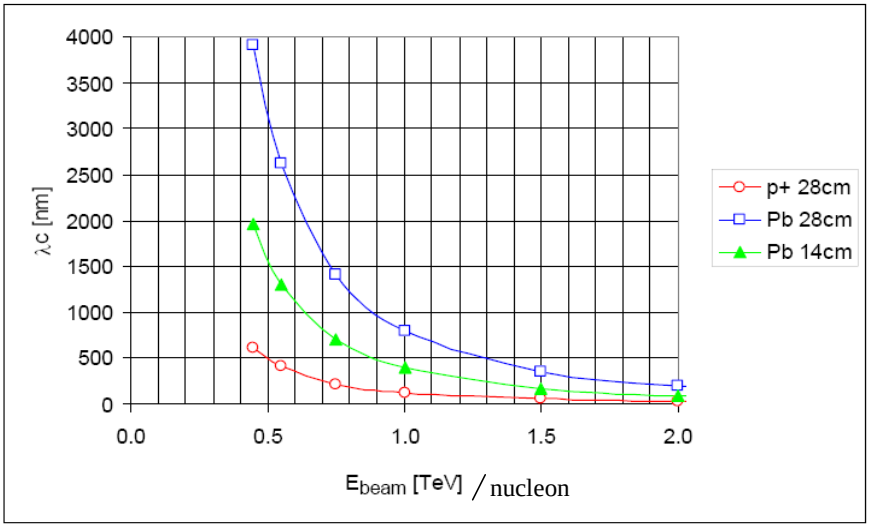

Figure 17. Wavelengths of the radiation emitted by protons and lead ions beams in a 140 mm and in a 280 mm period undulator. For the lead ions in abscissa the energy per nucleon is indicated.

Also with the 140 mm period undulator the proton CCD camera is able to reveal the emitted radiation only for energy above 600 GeV/nucleon. An upgrade of the camera will allow to make the measurement from the injection energy, but only integrated over 20 ms (Figure 18).

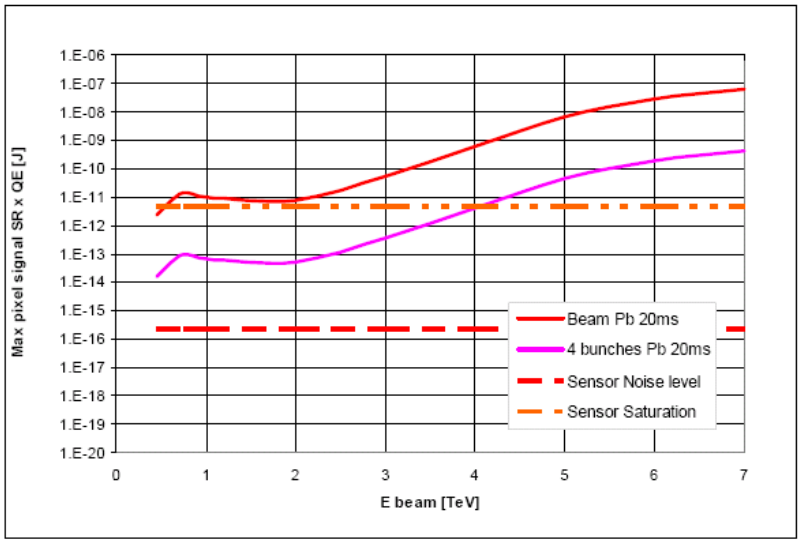

Figure 18. Estimated maximum synchrotron radiation signal emitted by lead ions beams in case of the use of an undulator of period = 140 mm [14].

An upgrade of the photocathode will allow to perform the 4 bunches and single turn beam measurement [15], but the single bunch turn-by-turn measurement is not yet possible.

In consideration of the fact that the NbTi undulator has to be substituted by a new one of half period length to perform the measurements on the lead ions beams, it has been decided to make a “versatile” undulator, which can be used as a 140 mm period for the lead ions beams and a 280 mm period for the protons beams.

The magnetic field for the long period configuration has to be the same of the NbTi undulator. Considerations about the detection system fixed the magnetic field of the 140 mm period to 3 T, a value sufficient to detect the radiation.

CHAPTER 2
MAGNETIC DESIGN OF THE UNDULATOR

Two designs have been considered to satisfy the request of making an undulator able to measure the profile of both protons and lead ions LHC beams. The first proposal consists in arranging the coils in such a way that their axis is parallel to the longitudinal beam axis. By this way a shorter period configuration suitable for protons is obtained by supplying all the coils, and a longer period one suitable for protons is obtained by energizing only one winding every two ones. This solution has been discarded for space limitations imposed by the fact that the undulator must be installed into a helium vessel able to be housed in a standard LHC dipole cryostat. The other proposed solution consists in arranging the coils in two superimposed rows; the upper one producing the longer, and the lower one, the shorter, period configuration. This solution has been optimized by 2D and 3D models, to take into account the finite dimensions in transversal direction of the coils and the yoke, to determine the field uniformity along this axis and to calculate the fringe field on the other circulating beam. The last part of the chapter is dedicated to the quench calculations made by the simulation code described in details in appendix A.

2.1. The electromagnetic design

The main requirements of both configurations of the undulator are summarized in Table 1.

The shorter the period the more challenging is to produce high magnetic fields in the mid-plane, because the flux lines tend to close from a pole to the next one without reaching the gap. At given gap, with smaller period it is then necessary to increase the

magnetic field on the conductor to obtain the same field in the mid-plane. Because of this effect it was possible to fabricate the 5 T, 280 mm undulator not exceeding 7 T on the conductor, making suitable the NbTi to manufacture it, whereas for the studied designs of the 3 T, 140 mm period configuration it is necessary to exceed 8 T on the wire. As a reference wire for the design the OI-ST, 0.8 mm of diameter which reaches 3000 A/mm^2 at 12 T and 4.2 K, described in details in chapter 4, has been used.

	λ = 140 mm	λ = 280 mm
Gap (mm)	60	
Number of periods	2	
B_0 (T)	3	5
Margin to quench (%)	> 15 %	
Operating temperature (K)	4.5	

Table 1. Main requirements for the two configurations of the undulator.

Several guidelines have been taken into account:

- Maximize the B_0/B_{coil} ratio;
- Minimize the iron yoke saturation, fixed the maximum dimensions imposed by the fact that the undulator will be positioned in the helium vessel able to be housed in a standard LHC dipole cryostat;
- Maximize the margin to quench, defined as the ratio:

$$Margin\ to\ quench\ (\%) = \frac{B_{CC} - B_{WP}}{B_{CC}} \cdot 100 \qquad (1)$$

  where B_{CC} is the field at the intersection between the load line and the critical curve at the operating temperature and B_{WP} is the maximum field in the coil at the working point;
- Design the coils in such a way that their radius of curvature is larger than the minimum one of the strand (10 mm).

The optimization of both configurations has been done using 2D models and after that, the 3D model has been made. The 3D model has been used to refine the results of the bi-dimensional model, to determine the field uniformity in the transversal dimension and to calculate the fringe field seen by the other circulating beam.

2.1.1. The 2D design

In this section both proposed designs are presented. Their optimization has been done with the Poisson code.

A scheme of the first proposed solution is shown in Figure 1.

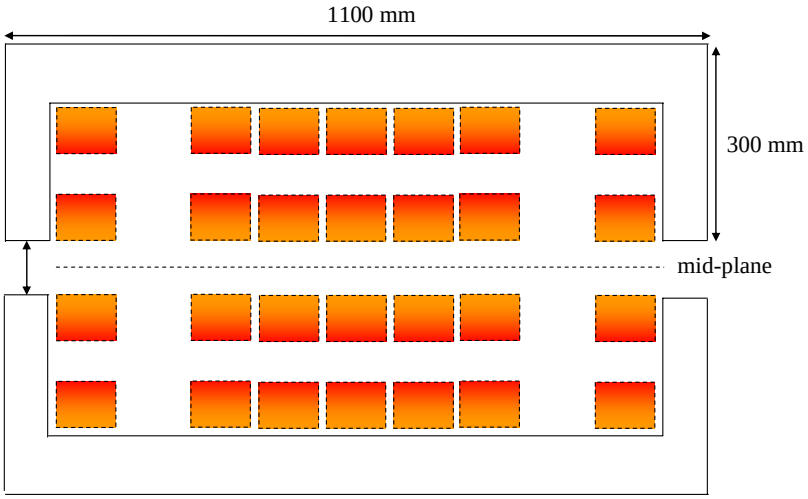

Figure 1. Scheme of the first proposed design of the undulator.

In this case the coils are positioned with their axis parallel to the longitudinal direction of the undulator. The two period configurations are obtained supplying the coils with appropriate currents. In particular the shorter period set-up is obtained supplying all the central coils, as indicated in Figure 2.

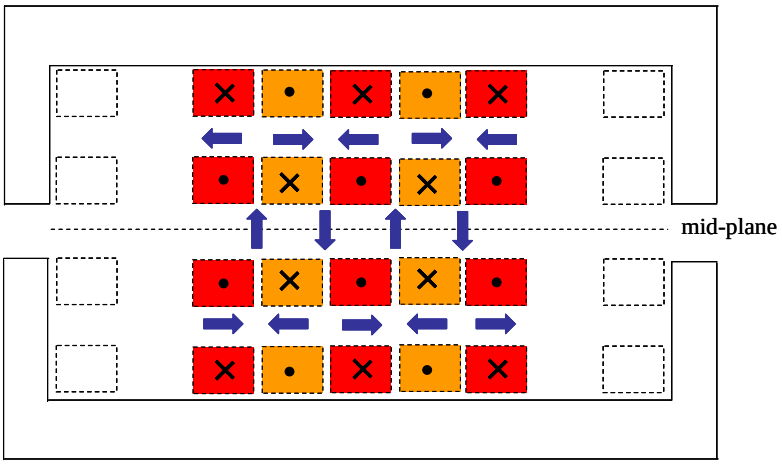

Figure 2. Schematic view of the 140 mm undulator configuration. The excitation of the coils and the direction of the produced magnetic fields are also indicated. The not-filled coils are switched off.

The longer period configuration is obtained supplying one coil each two ones, as indicated in Figure 3.

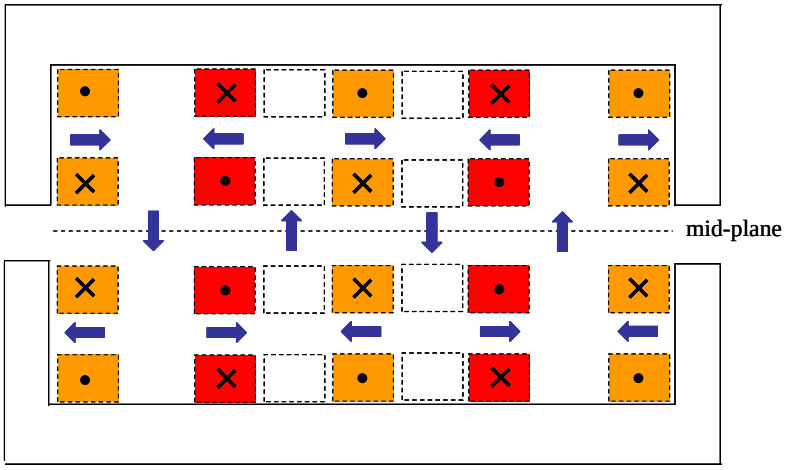

Figure 3. Schematic view of the 280 mm undulator configuration. The sense of the currents and the magnetic field are also indicated. The not-filled coils are the switched off ones.

This solution allows having a large margin to quench. For both the configurations the current in the coils are less than 500 A. The peak field on the conductor is about 13 T in the shorter period configuration and 10 T in the other case. In this solution the radius of curvature of the coils is a factor two more than the minimum one imposed by the technological limit indicated in section 2.1. . Nonetheless these aspects, this solution had to be discarded, because of the large yoke dimensions, which wouldn't allow positioning the magnet in helium vessel in a standard LHC dipole cryostat. Also using a larger yoke height, the flux is not completely contained by the yoke, which at the top saturates (2.4 T), like shown in Figure 4.

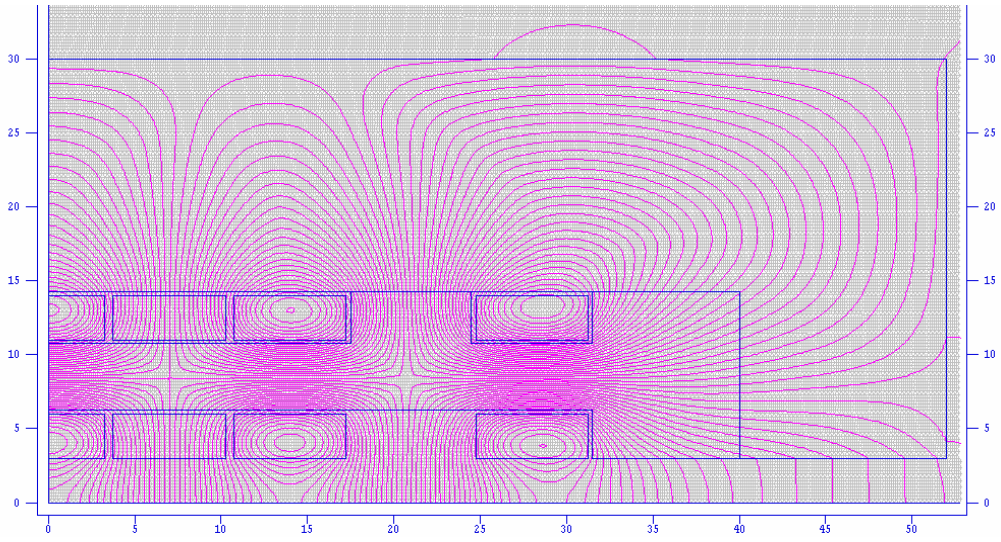

Figure 4. Flux lines distribution of the 280 mm period configuration. For symmetry only ¼ of the complete undulator is shown. At the top of the yoke 2.4 T are present. Dimensions are in mm.

The schematic view of the second proposed solution is shown in Figure 5.

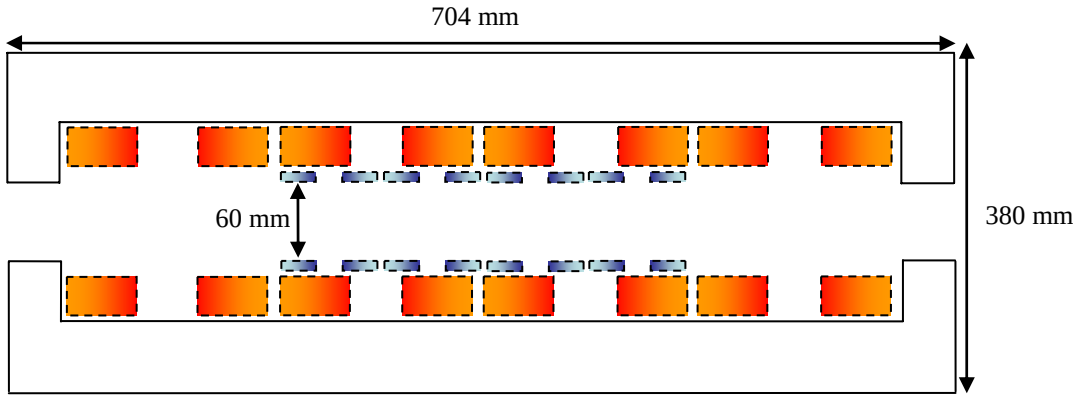

Figure 5. Complete layout of the undulator. The coils of the short period configuration are closer to the mid-plane (light blue) and the ones of the long period are above it (orange).

According to this design the coils are arranged in two superimposed rows. The coils closest to the mid-plane are used for the shorter period configuration, the farest ones for the longer period configuration. The coils have their axis perpendicular to the longitudinal dimension of the magnet. In particular in Figure 6 the shorter period configuration setting-up is shown.

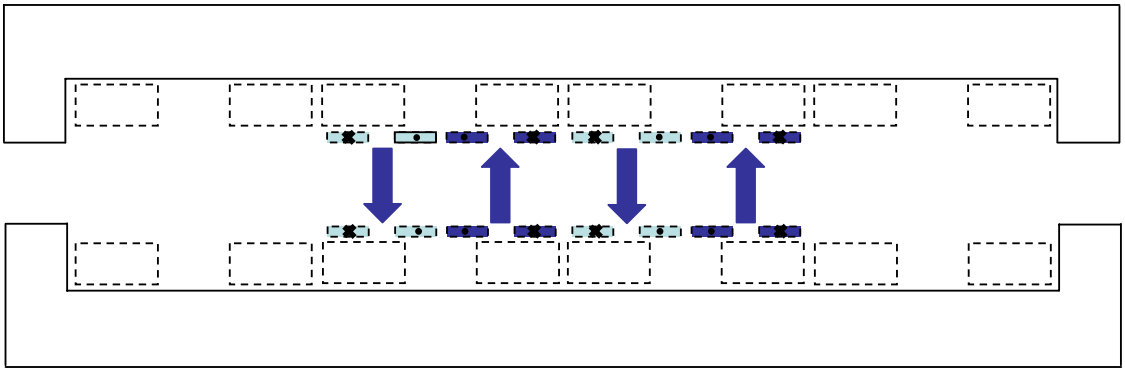

Figure 6. Schematic view of the 140 mm undulator configuration. The sense of the circulating current and the produced magnetic field are also indicated.

In this case only the coils closest to the mid-plane are supplied. Supplying the other coils the longer period configuration is obtained, as shown in Figure 7.

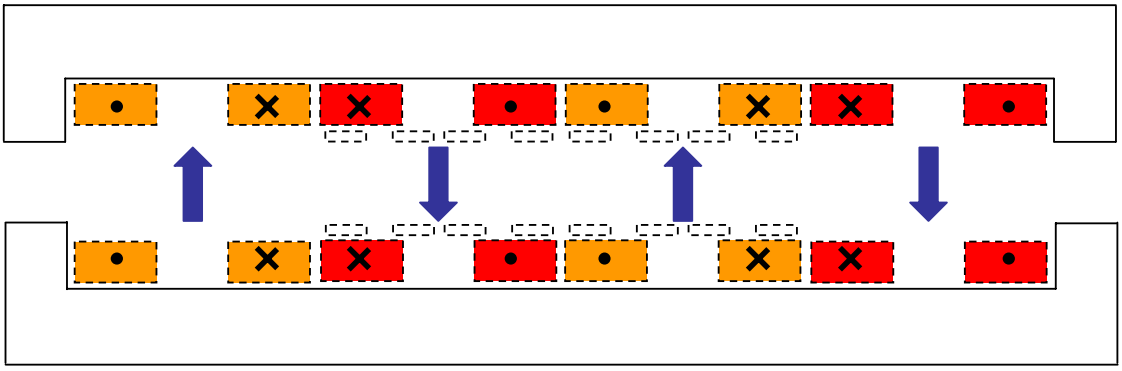

Figure 7. Schematic view of the 280 mm undulator configuration. The sense of the current and the magnetic field are also indicated.

The first part of the design was the optimization of the short period configuration. The goal was to produce the requested 3 T in the mid-plane, maintaining as small as possible the height of the coils, in order to place the coils of the long period configuration as close as possible to the centre of the gap. This is desirable for two reasons: it allows containing the saturation at the top of the yoke, and, at the same time, minimizing the gap of the longer period configuration.

Several solutions are possible for various heights of the coils to obtain the requested 3 T of the 140 mm period configuration. The height of the coil has been found by imposing the maximum dimension along the longitudinal axis of the magnet, according to the minimum radius of curvature of the Nb_3Sn strand and the requested field. The obtained results are shown in Table 2.

Current (A)	Coil height (mm)	B_{max} coil (T)	Margin to quench (%)
900	10.0	7.54	23.6
800	12.5	8.14	22.5
700	15.0	8.11	25.9
600	20.0	8.29	28.4

Table 2. Summary of the optimized solutions of the 140 mm undulator configuration.

The first solution has been chosen, because it gives the minimum height of the coils, maintaining a good margin for the power supply (max current of 1000 A).

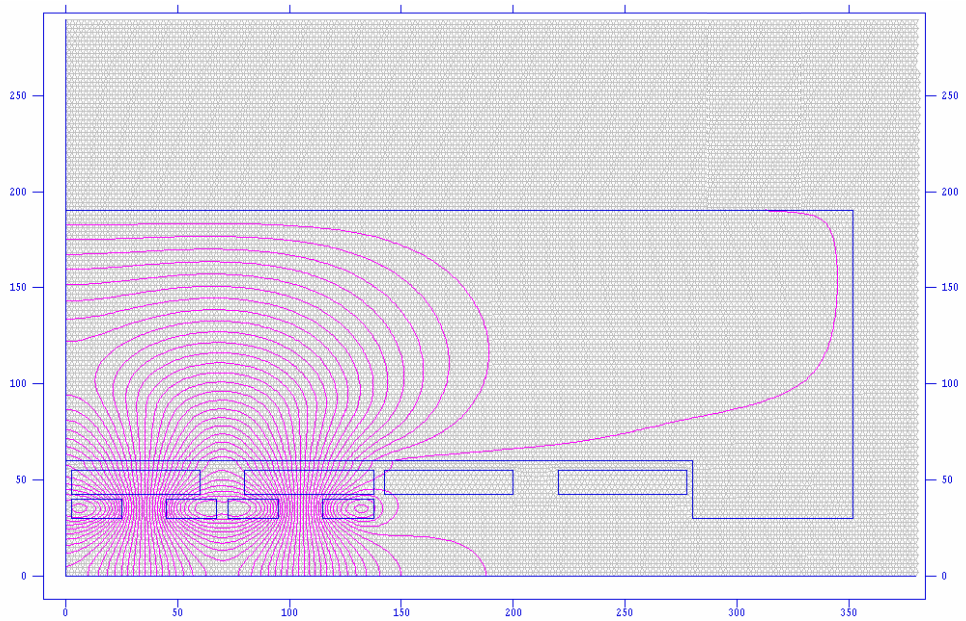

Figure 8. Distribution of the flux lines of the 140 mm period configuration. For reasons of symmetry only ¼ of the complete undulator is simulated. Dimensions are in mm.

The corresponding distribution of the field lines obtained in this case is shown in Figure 8.

In this configuration no saturation is present at the top of the yoke (magnetic field inside the iron is less than 2 T already for a distance of 80 mm from the mid-plane).

The magnetic field along the axis of the undulator along the longitudinal axis on the mid-plane is shown in Figure 9.

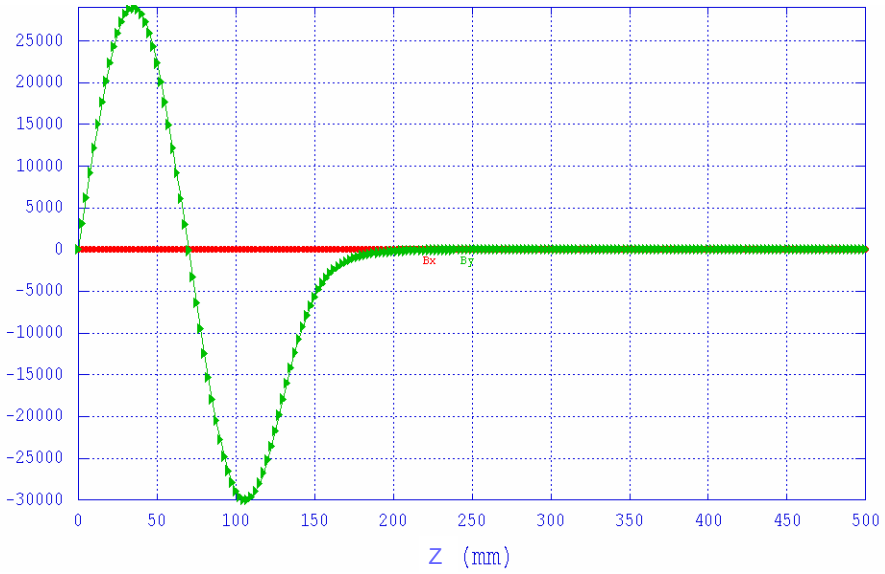

Figure 9. Magnetic field (Gauss) along the logitudinal axis of the undulator in the mid-plane. The figure represents one period of the complete magnet.

In Figure 10 the working point of the coils of the short period configuration of this solution and the critical curve are shown.

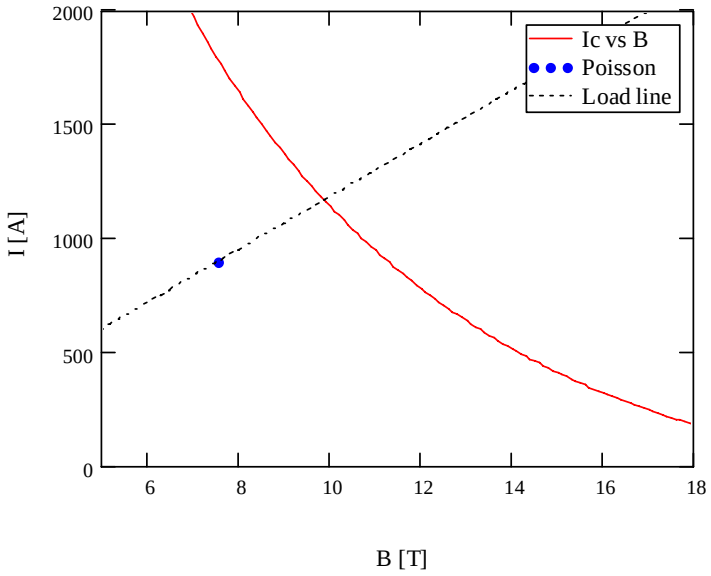

Figure 10. Margin to quench for the 140 mm period configuration. The working point (Poisson), the load line and the critical curve at the operating temperature are indicated.

In Table 3 the main characteristics of the 140 mm configuration are summarized.

	λ = 140 mm
Gap (mm)	60
Operating temperature (K)	4.5
Number of periods	2
Current (A)	900
B_0 outer pole (T)	3.0
B_0 central pole (T)	2.9
Margin to quench (%)	23.6
Number of layers	24
Number of turns	10

Table 3. Main parameters of the 140 mm undulator configuration.

The second step of the design was the optimization of the 280 mm configuration.
As in the previous case, given the minimum radius of curvature, the longitudinal dimension of the coils has been determined to obtain the requested magnetic field in the mid-plane. The distance between the coils and the yoke in the longitudinal dimension (2.5 mm) has been determined by the insulation, as for the 140 mm period configuration, whereas the separation between the coils and the yoke along the vertical axis has been optimized to maximize the margin to quench. Placing the coils close to the yoke, in fact, increases the field on the conductor, making Nb_3Sn closer to its critical curve without appreciably enhancing the field in the gap.
The main parameters of the optimized solution are shown in Table 4.

Current (A)	Coil height (mm)	B_{max} coil (T)	Margin to quench (%)
570	12.5	9.86	19.9

Table 4. Main parameters of the 280 mm undulator configuration.

The layout and the corresponding distribution of the flux lines are shown in Figure 11.

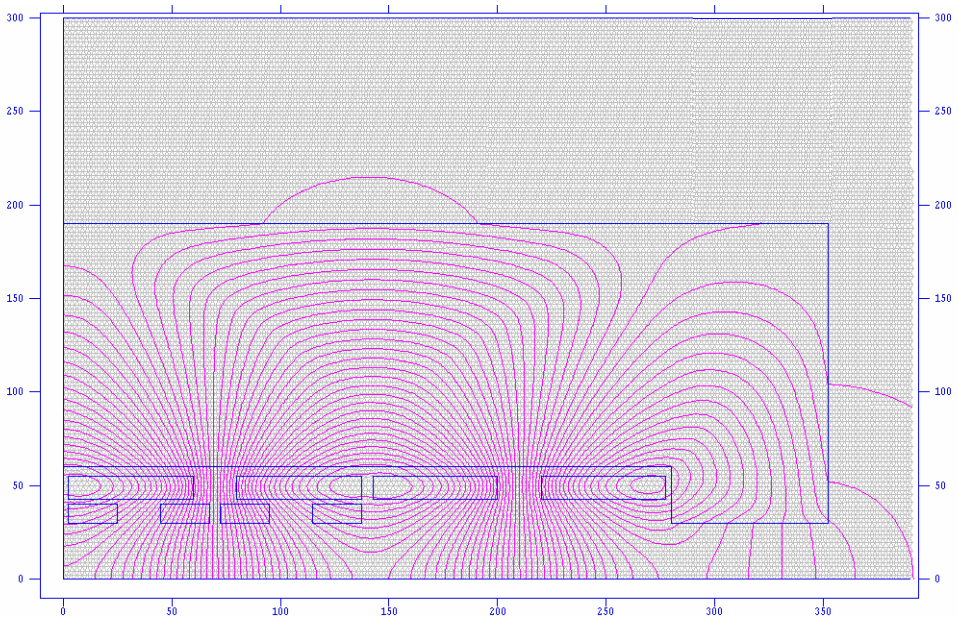

Figure 11. Distribution of the flux lines of the 280 mm period configuration. For reasons of symmetry only ¼ of the complete undulator is simulated. Dimensions are in mm.

The dimensions of the iron yoke are compatible with the insertion of the undulator into the standard LHC dipole cryostat. A saturated zone is present also in this case at the vertical boundary of the yoke (maximum field at the top is about 2.4 T). To reduce that it is being considering using the cobalt-iron alloy AFK1 which saturates at about 2.4 T [1].

The magnetic field along the longitudinal axis is shown in Figure 12.

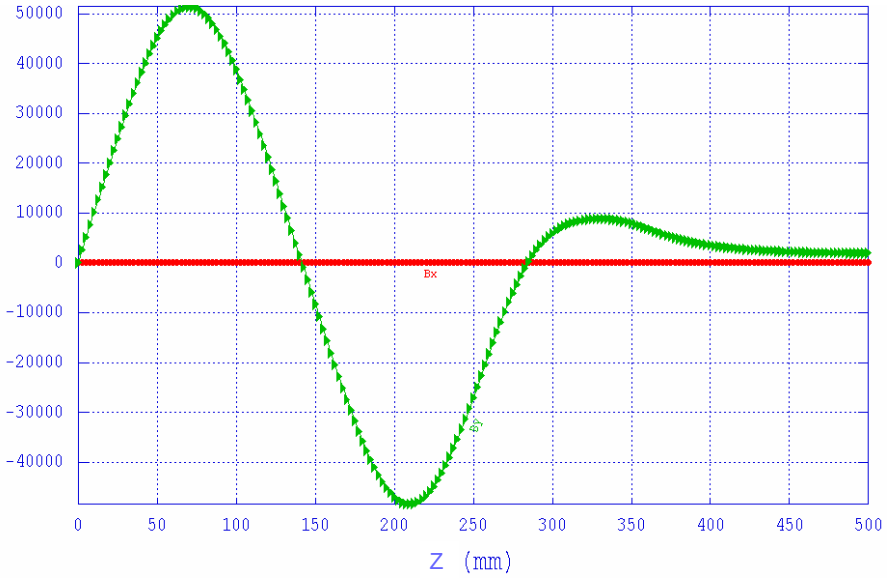

Figure 12. Magnetic field along the longitudinal axis of the undulator for 280 mm period. Magnetic field is in Gauss. The figure represents one period.

The working point of the coils of this configuration and the critical curve are shown in Figure 13.

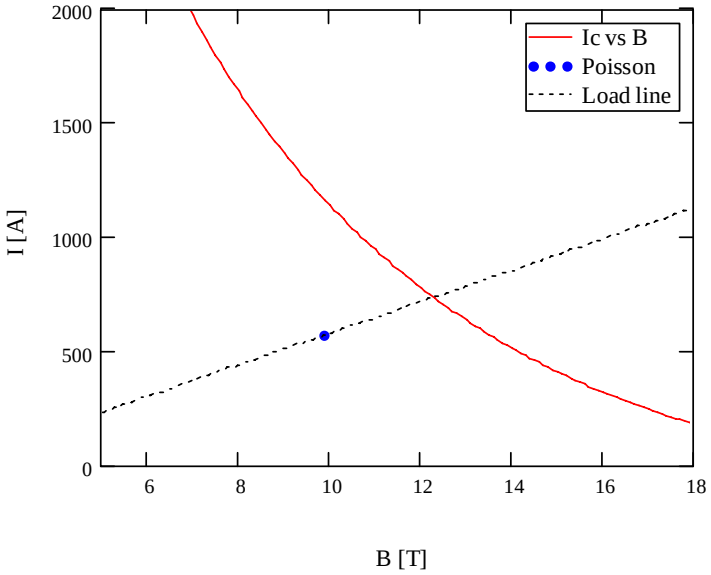

Figure 13. Margin to quench for the 280 mm period configuration. The working point (Poisson), the load line and the critical curve (Ic vs B) are indicated.

As in the 140 mm period configuration the margin to quench is about 20 %.

Having increased the distance in the vertical dimension between the coils of the longer period configuration and the iron yoke to maximize the margin to quench, it was necessary to increase the excitation current to 950 A for the short period configuration. The margin to quench of this configuration has been reduced, but, in any case, it remained close to 20%.

	λ = 140 mm	λ = 280 mm
Gap (mm)	60	
Operating temperature (K)	4.5	
Number of periods	2	
Current (A)	950	570
B_0 outer pole (T)	3.0	5.07
B_0 central pole (T)	2.9	4.78
Margin to quench (%)	19.1	19.9
Number of layers	24	61
Number of turns	10	13

Table 5. Summary of the geometrical and the magnetic characteristics of both 140 mm and 280 mm undulator configurations.

In Table 5 the main magnetic and geometrical characteristics of both configurations are summarized.

This design allows achieving the requested 3 T in the 140 mm configuration and 5 T in the 280 mm one, maintaining a margin to quench of about 20 % in both the setting-up and the dimensions of the iron yoke allow arranging the undulator in a standard LHC dipole cryostat. To more efficiently confine the magnetic flux lines it is being considering using an iron-cobalt alloy, which saturates at 2.4 T to make the yoke.

2.1.2. The 3D model

After the optimization of the undulator has been done in 2D, the 3D model has been made to take into account the finite transverse dimensions of the yoke and the coils, assumed infinite in the 2D model. This also allows determining the uniformity of the magnetic field along the horizontal transverse dimension and to calculate the fringe field seen by the other circulating beam at 420 mm from the axis of the magnet.

The 3D model of the complete undulator, made with the code Opera [2], is shown in Figure 14.

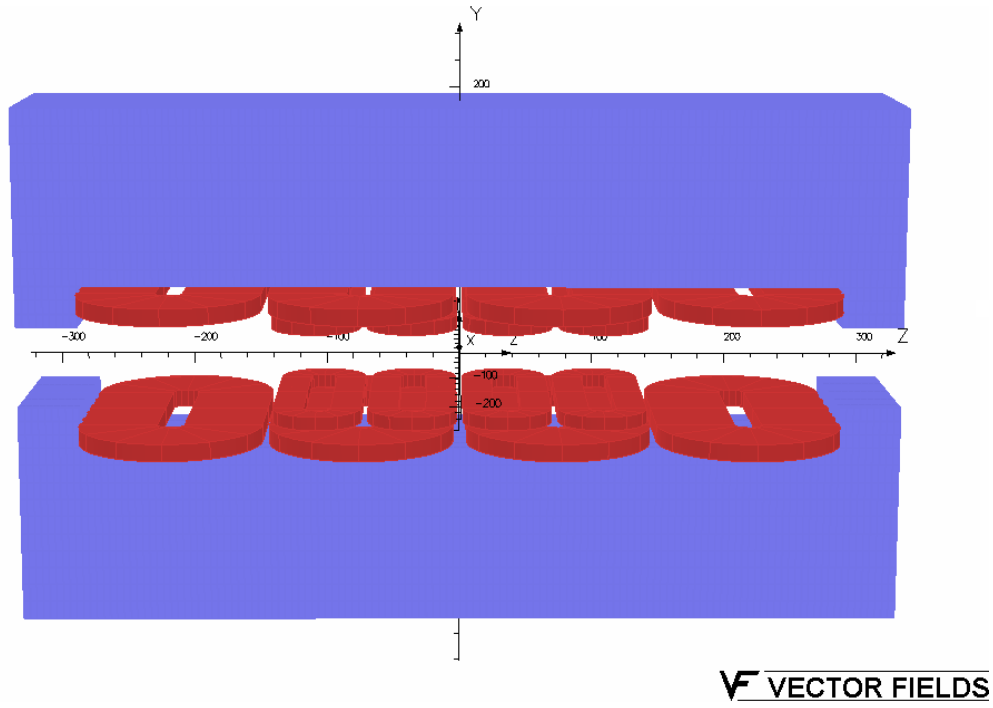

Figure 14. View of the 3D complete undulator. The 280 mm period undulator above 140 mm one is visible. Dimensions are in mm.

The y and the z axis correspond respectively to the vertical and the horizontal dimensions of the 2D model and x to the other transverse direction.

The coils are racetracks of straight length equal to 120 mm, as in the NbTi undulator [3]. This dimension has been chosen to produce a very uniform magnetic field along

the horizontal transversal dimension. In Figure 15 the geometry of the coils in both configurations is shown.

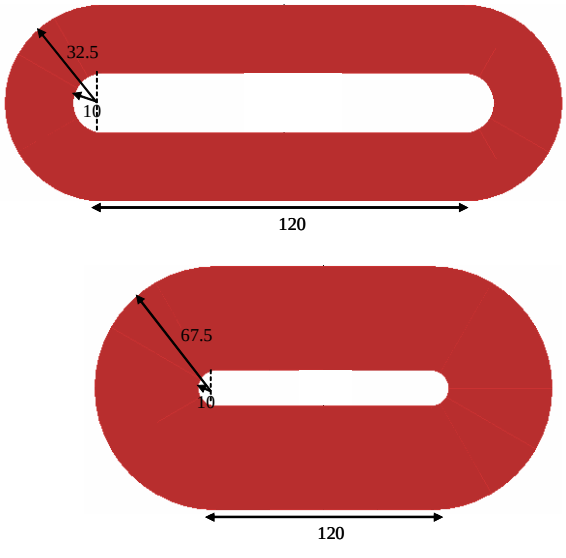

Figure 15. (a) 140 mm configuration coil geometry. (b) 280 mm configuration coil geometry. Dimensions are in mm.

In Figure 16 the vertical component of the magnetic field for the 140 mm period configuration obtained from the 3D model is shown.

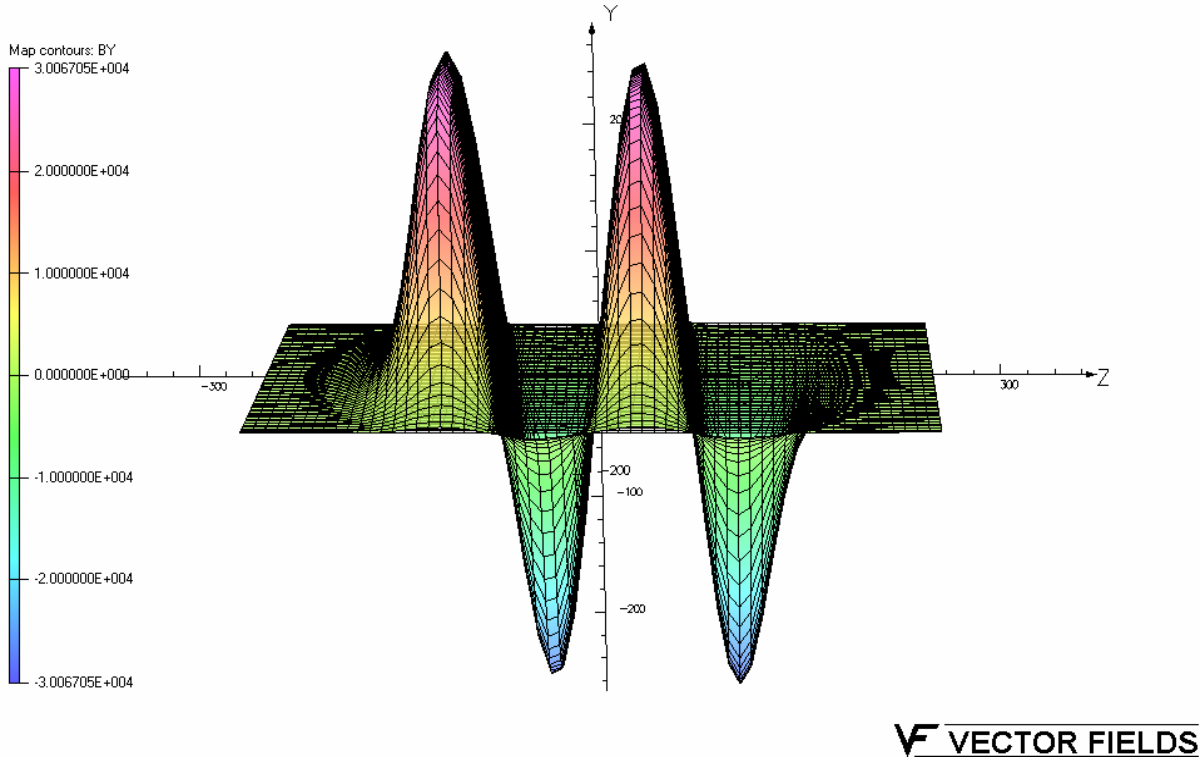

Figure 16. Vertical component of the magnetic field By simulated by Opera for the 140 mm period configuration.

The transversal finite dimensions of the coils and of the iron yoke do not produce a sensible difference on the magnetic field between the 2D and the 3D (difference in the mid-plane smaller than 0.4%), then it was not necessary to increase the current with respect to the 2D model.

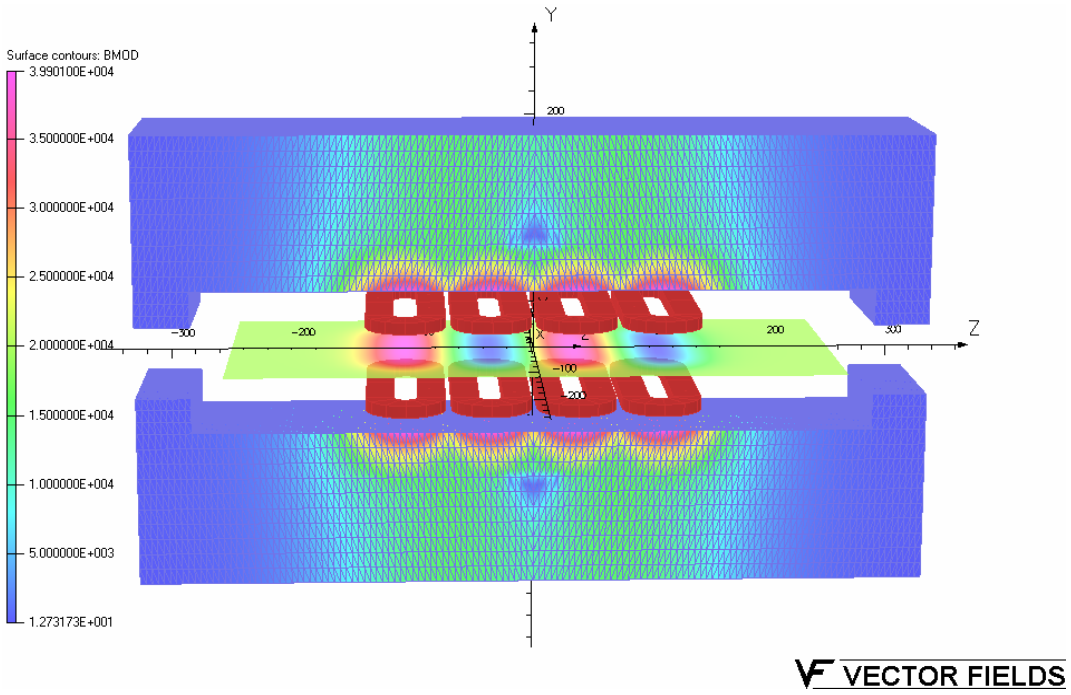

Figure 17. The magnetic field in the iron yoke and the vertical component in the mid-plane in the 140 mm configuration. The dimensions are in mm and the field in Gauss.

The module of B in the iron yoke and its vertical component in the mid-plane (y = 0 mm) are shown in Figure 17.

In Figure 18 the vertical component of the magnetic field for the 280 mm period configuration obtained from the 3D model is plotted.

In this case it was necessary to slightly increase the value of the current to 580 A to produce 5 T in the mid-plane, because of the finite dimensions of the yoke and of the coils. This decrease of the margin to quench, which, in any case, remained higher than 15% (18.7 % instead of 19.9 %).

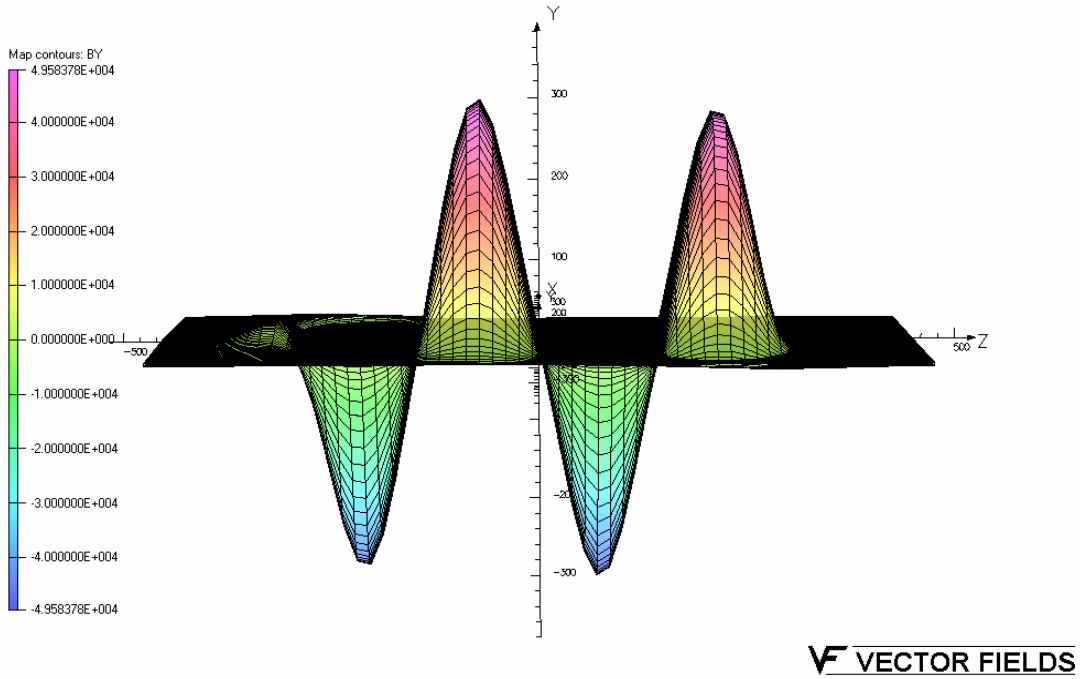

Figure 18. Vertical component of the magnetic field By on the plane y = 0 mm simulated by Opera for the 280 mm period configuration.

The second aspect to study with the 3D model is the field uniformity in the plane where the beam wiggles. The magnetic field has to be as uniform as possible in the transverse dimension to avoid that the undulator becomes a source of non-linearity for the beam dynamics.

In Figure 19 the vertical component of the magnetic field in the x-z plane at y = 0 mm is plotted for the 140 mm configuration.

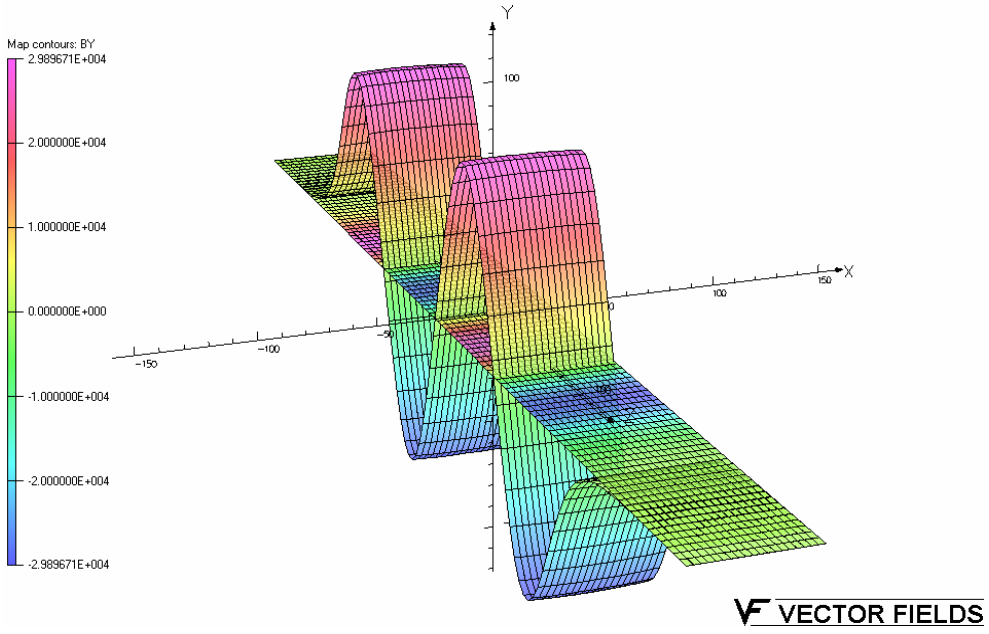

Figure 19. Transverse field in the 140 mm configuration. The dimensions are in mm and the magnetic field in Gauss.

The variation of the field between x = 0 mm and x = 25 mm on this plane is less than 0.7 % for both peaks. The deviation in x from the axis of the undulator of a particle entering on the axis of the undulator in the mid-plane is negligible with respect to the beam dimension at the injection energy (σ = 1.2 mm) and at the collision (σ = 318 μm). In Table 6 these values and the exit angle are shown.

	Δx (μm)	Δx' (μrad)
E = 177.4 GeV/nucleon	21.37	0.00
E = 2.759 TeV/nucleon	0.01	0.00

Table 6. Maximum deviation from the undulator axis, x and angle at the exit of a lead ion entering on the axis.

The graph of the vertical component of the magnetic field in the x-z plane at y = 0 mm is shown in Figure 20 for the 280 mm period configuration.

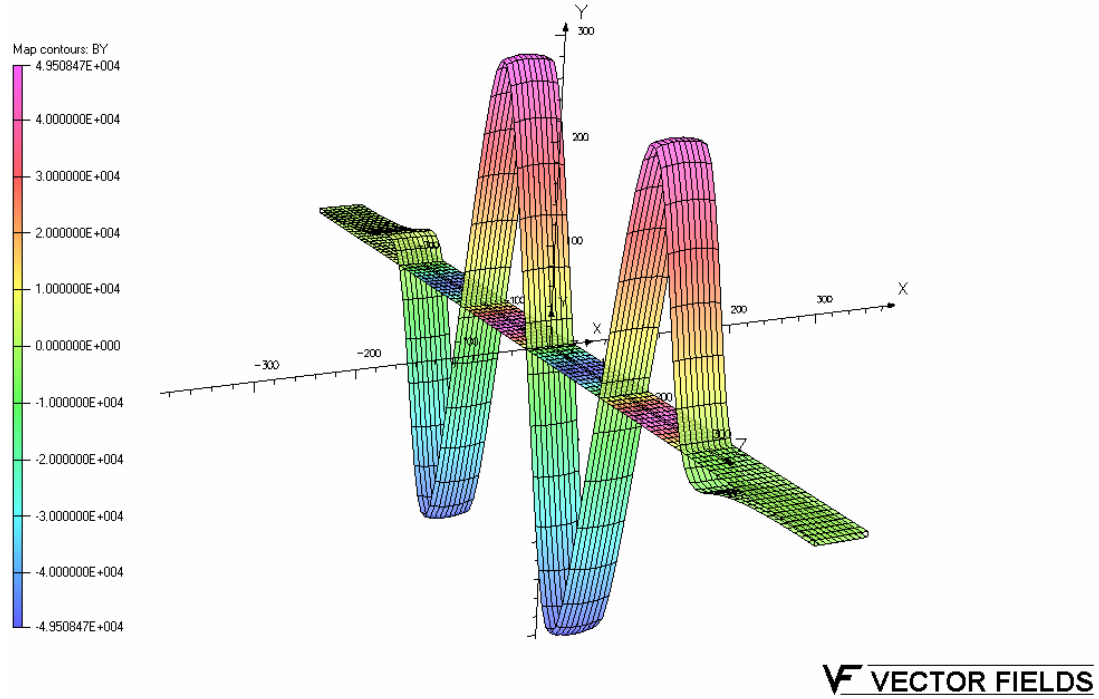

Figure 20. Transverse field in the 280 mm configuration. Dimensions are in mm and the magnetic field in Gauss.

In this case the variation of the field is less than 1.5 % for both the peaks. It is negligible for the proton beams dynamics. Also in this case the deviation in x from the axis of the undulator of a proton entering on the axis of the undulator in the mid-plane is negligible with respect to the beam dimension at the injection energy (σ = 1.2 mm) and at the collision (σ = 317 μm). In Table 7 these values and the exit angle are shown.

	Δx (μm)	Δx' (μrad)
E = 450 GeV	51.26	0.30
E = 7 TeV	3.30	0.02

Table 7. Maximum deviation from the undulator axis, x and angle at the exit of a lead ion entering on the axis.

In Figure 21 the schematic view of the region where the measurement will be performed is shown.

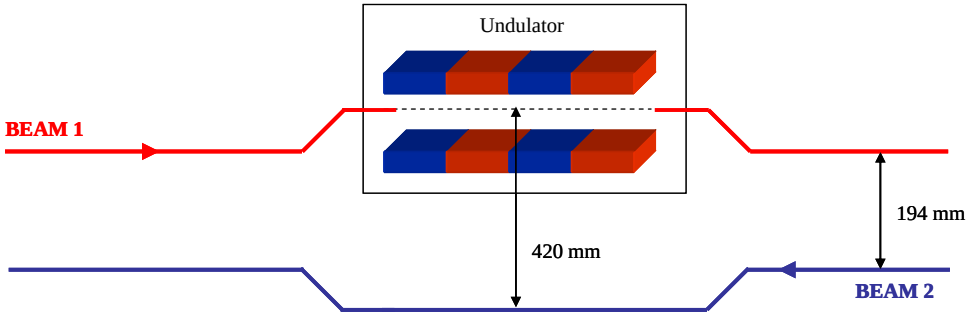

Figure 21. The beam 1 wiggles into the undulator and the beam 2 is at 420 mm from the axis of the magnet.

A dipole is used to deviate the beam 1 into the undulator, whereas the beam 2 circulates following the closed orbit, which is at 420 mm from the axis of the insertion device. It is then important to determine the fringe field seen by the beam 2. To investigate this aspect in Figure 22 the magnetic field for the 140 mm configuration is plotted.

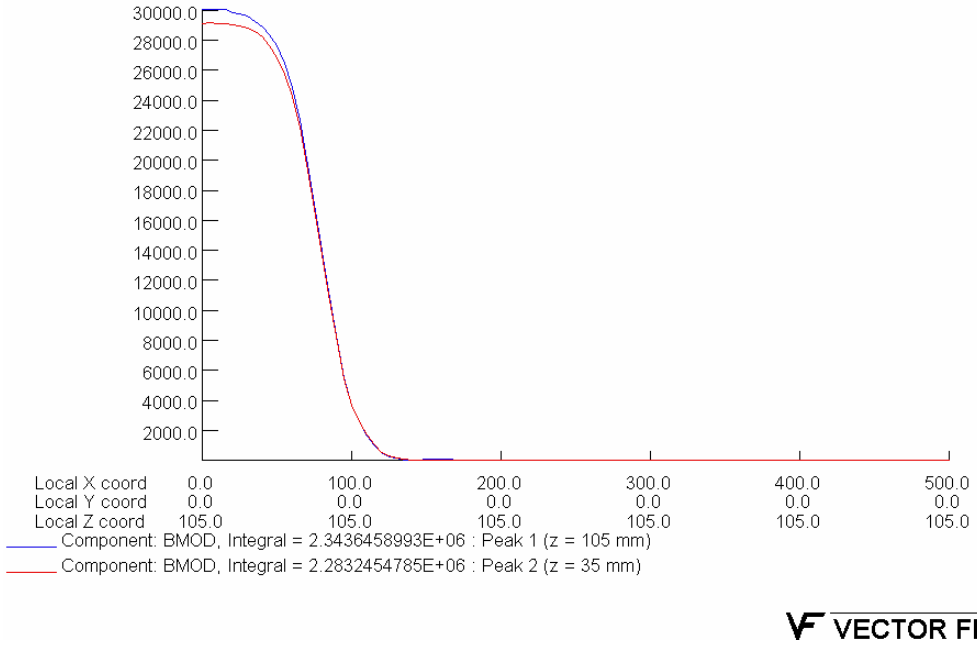

Figure 22. Magnetic field from the axis of the undulator (x = 0 mm) to 500 mm from it for both peaks of the 140 mm period configuration. Dimensions are in mm and field in Gauss.

The fringe field at 420 mm is less than 0.12 mT for both peaks.

In Figure 23 the analogous graph for the 280 mm period configuration is shown.

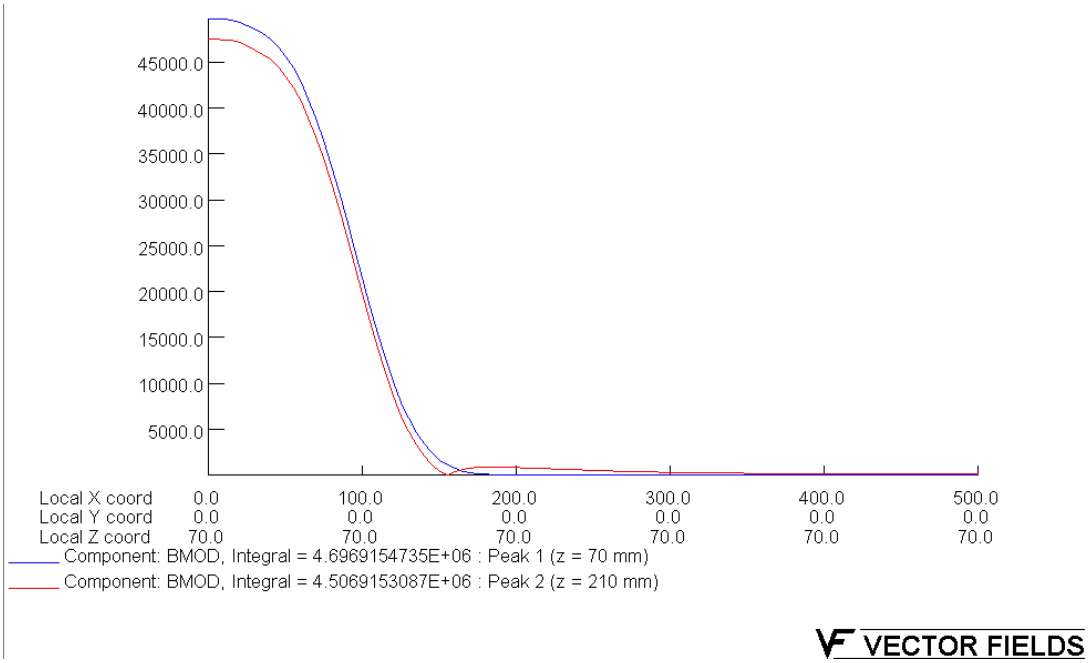

Figure 23. Magnetic field from the axis of the undulator (x = 0 mm) to 500 mm from it for the 280 mm period configuration for both peaks. Dimensions are in mm and field in Gauss.

In this configuration the magnetic field remains under 15 mT for both peaks.

It can then been concluded that in both configurations the fringe field is negligible for the beam dynamics.

Order	Sine term
n	A_n
0	0.00
1	-2.89
2	2.3×10^{-3}
3	3.0×10^{-2}
4	6.0×10^{-4}
5	3.9×10^{-3}
6	6.0×10^{-4}
7	-1.3×10^{-3}
8	8.2×10^{-4}
9	2.2×10^{-3}

Table 8. Fourier analysis result for the vertical component of the magnetic field By in the case of the 140 mm period configuration.

As it has been shown in the first chapter, the wavelength of the emitted radiation depends on the period of the magnetic field, then to have an estimation of the components of the harmonics of the synchrotron radiation, a Fourier analysis of the magnetic field along the longitudinal axis from z = -140 mm to z = 0 mm for the short period configuration and from z = -280 mm to z = 0 mm for the long period case, has been performed to determine the weight of its harmonics. As it can be seen from the Table 8, where the results obtained for the 140 mm period configuration are presented, the contribution of the harmonics different than the fundamental one is negligible for the emitted radiation.

In case of the longer period configuration the contributions of the higher order harmonics is not negligible with respect to the one of the fundamental, as can be seen in Table 9.

Order	Sine term
n	A_n
0	0.00
1	4.81
2	1.63
3	0.87
4	0.64
5	0.51
6	0.42
7	0.36
8	0.31
9	0.27

Table 9. Fourier analysis result for the vertical component of the magnetic field By in the case of the 280 mm period configuration.

This calculation allows giving a rough estimation of the weight of the several harmonics. A more precise calculation will be performed using ZGOUBI [4].

In Table 10 the main characteristics of the undulator for both configurations are summarized.

		λ = 140 mm	λ = 280 mm
Gap (mm)		60	
Number of periods		2	
Current (A)		950	580
B_0 1 (T)		2.91	4.97
B_0 2 (T)		3.00	4.75
Margin to quench (%)		19.1	18.7
ΔBy @ x = 25 mm / By @ x = 0 mm	Peak 1	0.69 %	1.4 %
	Peak 2	0.67 %	1.5 %
Fringe field (mT)	Peak 1	0.5	15
	Peak 2	0.12	5.3
Total stored energy (kJ)		32.19	159.85
Number of layers		24	61
Number of turns		10	13
Length of the strand for 8 coils (km)		0.86	3.42
Total length of the strand for both the configurations (km)		4.28	

Table 10. Main characteristics of the undulator magnetic design.

The 3D model allowed refining the results obtained from the 2D case, verifying that the field uniformity and the fringe field don't perturb the dynamics of the both beams.

2.2. The forces estimation

To make as large as possible the distance between the two circulating beams the undulator is not arranged at the center of the cryostat, as shown in Figure 24.

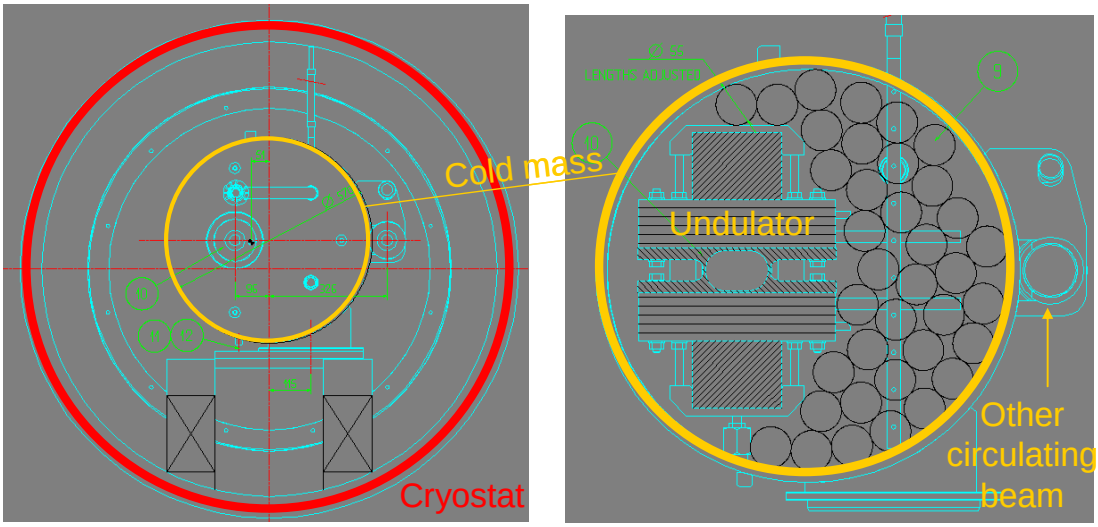

Figure 24. Drawing of the undulator in the cryostat. The z axis is perpendicular to the figure. The cold mass where the undulator is inserted and the position of the other circulating beam are indicated.

Because of the off centered position of the undulator in the cryostat transverse forces act between the magnet and the wall of the cryostat. In this section it is verified that they are negligible.

Let E is the magnetic energy, the magnetic force $\vec{F}$ is given by:

$$\vec{F} = -\nabla E \tag{2}$$

The horizontal and the vertical component of the force F_x and F_y are then respectively given by:

$$\begin{cases} F_x = -\dfrac{\partial E}{\partial x} \\ F_y = -\dfrac{\partial E}{\partial y} \end{cases} \tag{3}$$

The equations (3) can be discretized as:

$$\begin{cases} F_x = -\dfrac{\partial E}{\partial x} \approx -\dfrac{E_x - E_N}{\Delta x} \\ F_y = -\dfrac{\partial E}{\partial y} \approx -\dfrac{E_y - E_N}{\Delta y} \end{cases} \tag{4}$$

where E_N, E_x and E_Y are the energies of the system in the configuration of the undulator at its nominal position and shifted of 2 mm in the horizontal and in the vertical dimension respectively. To determine them the model of the undulator included in the cryostat, shown in Figure 25, has been done.

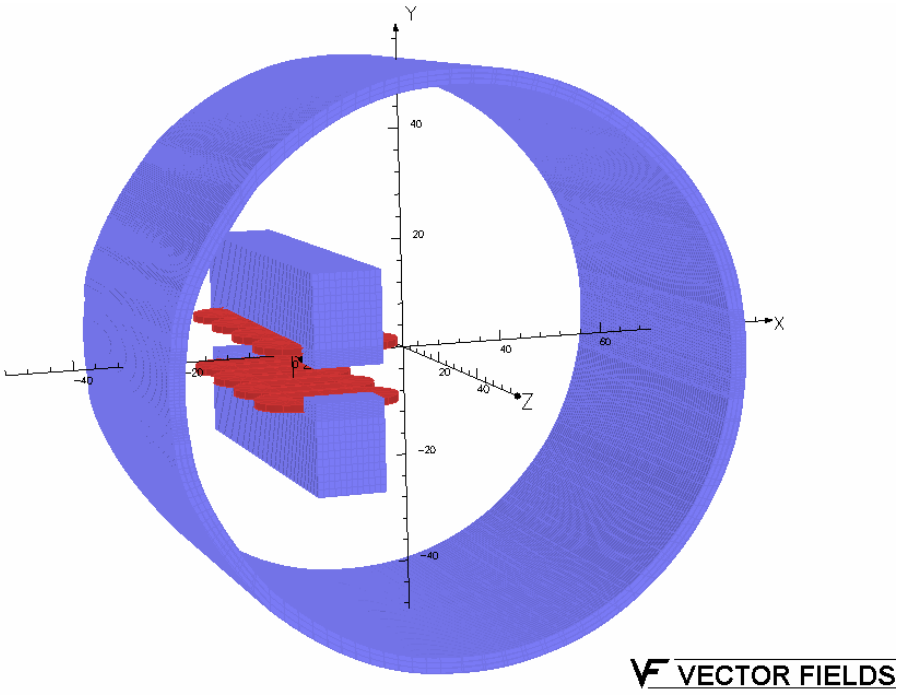

Figure 25. Model of the undulator in the cryostat.

In Table 11 the energies E_N, E_x and E_Y and the corresponding forces are indicated.

E_N (kJ)	E_X (kJ)	E_Y (kJ)	F_X (N)	F_Y (N)
159.78694	159.78695	159.78814	5	600

Table 11. Energies of the undulator included in the cryostat at its nominal position, shifted of 2 mm in the horizontal and in the vertical dimension. The resulting components of the forces are also indicated.

This simplified calculation allows demonstrating that the components of the force are negligible in both the transverse dimensions.

2.3. The quench calculations

The resistances of the system of protection of the undulator (Figure 26) have been optimized using the code described in Appendix A to minimize the hot spot temperature.

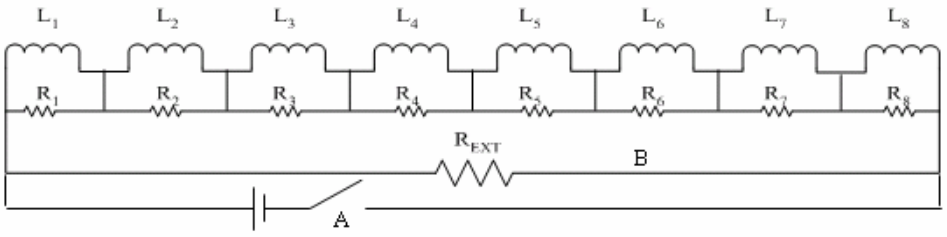

Figure 26. Scheme of the system of protection of the undulator. After the quench is detected the switch A opens isolating the power supply and B closes the circuit on the resistance R_{EXT}.

In Table 12 the inputs of the program are summarized.

		λ = 140 mm	λ = 280 mm
System	Input current (A)	950	580
	Bath temperature (K)	4.2	
Strand characteristics	Radius insulated (mm)	0.93	
	Non Cu fraction	53 %	
	RRR	89	
Coil characteristics	Number of layers	24	61
	Number of turns	10	13
Circuit of protection	Inductances	See Table 13	See Figure 28/Table 15
	Resistances	See Table 14	See Table 16

Table 12. Most important input of the quench simulation code.

The self-inductances L of the coils have been determined from the relation:

$$E_L = \frac{1}{2} L I^2 \qquad (5)$$

known the stored energy E_L when only one coil is energized at current I. The mutual inductances have been determined from the relation:

$$E_M = \frac{1}{2} L_1 I_1^{\,2} + \frac{1}{2} L_2 I_2^{\,2} + M_{12} I_1 I_2 \qquad (6)$$

known the stored energy E_M when a couple of coils are energized with currents I_1 and I_2.

To determine the stored energies a complete model of the undulator without any symmetry has been used.

2.3.1. The 140 mm period configuration

In Table 13 the values of the inductances used in the simulation are shown.

L (mH)	Mo (mH)	Mc (mH)
8	1	0.4

Table 13. Self (L) and mutual inductances of the central coil with the coil symmetric with respect to the mid-plane (Mo) and the close one (Mc).

In all the circuits of protection, simulated varying R_{EXT} and R_{PAR}, the hot spot temperature is less than 100 K (Table 14).

R_{EXT} (Ω)	R_{PAR} (Ω)	$T_{HOT\ SPOT}$ (K)
0.10	0.10	98
1.00	0.10	72
1.00	1.00	59

Table 14. Hot spot temperature of the coil of the long period configuration in case of quench for several values of the resistance in parallel to each coil (R_{PAR}) and the one in parallel to the whole magnet (R_{EXT}).

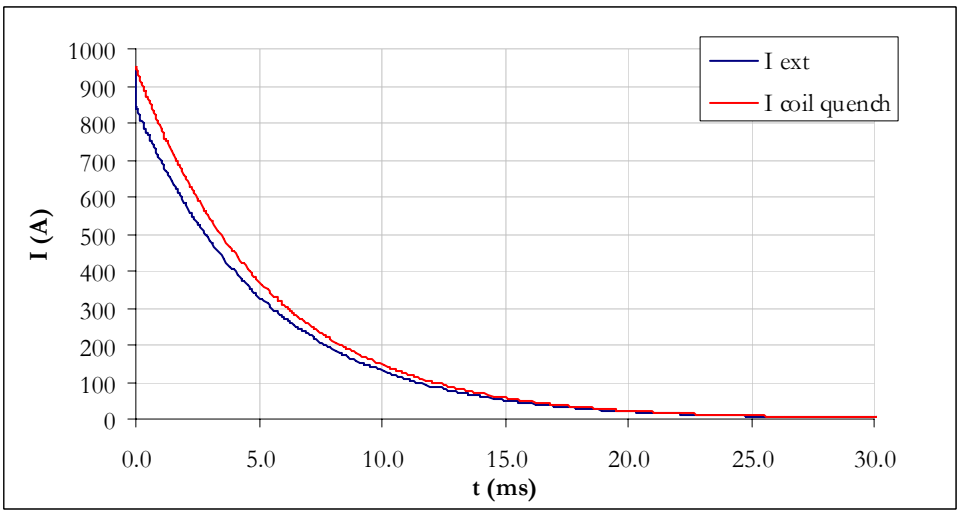

Figure 27. Discharge of the current in the simulated configuration which corresponds to the lowest hot spot temperature.

For the configuration which corresponds to the lowest hot spot temperature the discharge of the current is shown in Figure 27.

2.3.2. The 280 mm period configuration

In case of the long period configuration, because of the vicinity of the coils to the iron, the inductances depend on the current. In this case then the code assumes a constant value of 110 mH for current below 130 A and the function indicated in Figure 28 onwards.

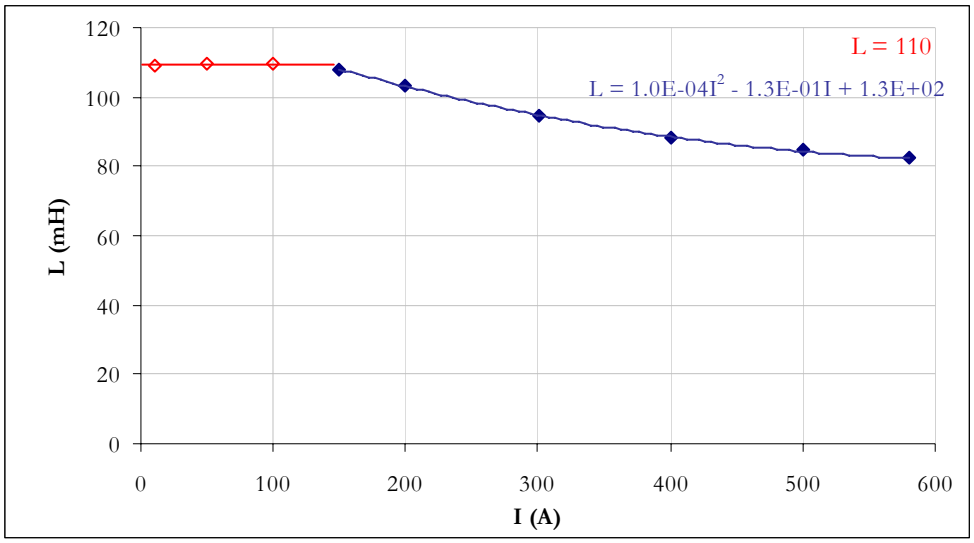

Figure 28. Self inductance of the central coil vs the current.

The mutual inductances at the nominal currents are shown in Table 15.

Mo (mH)	Mc (mH)
9	2

Table 15. Self (L) and mutual inductances of the central coil with the coil symmetric with respect to the mid-plane (Mo) and the close one (Mc).

R_{EXT} (Ω)	R_{PAR} (Ω)	$T_{HOT\ SPOT}$ (K)
0.10	0.10	113
1.00	0.10	105
1.00	1.00	98

Table 16. Hot spot temperature of the simulation of a quench in a coil of the short period configuration of the undulator for several values of the resistance in parallel to each coil (R_{PAR}) and the one in parallel to the whole magnet (R_{EXT}).

For the calculations reported the dependence of the mutual inductance has been neglected. To take into account of this effect it would have been necessary to know the currents in each couple of coils before running the simulation to determine the corresponding stored energy.

Also in this configuration the hot spot temperature in all the simulated circuit of protection considered is less than 120 K (Table 16).

In all these configurations an acceptable hot spot temperature has been obtained.

In particular in Figure 29 the discharge of the current is shown.

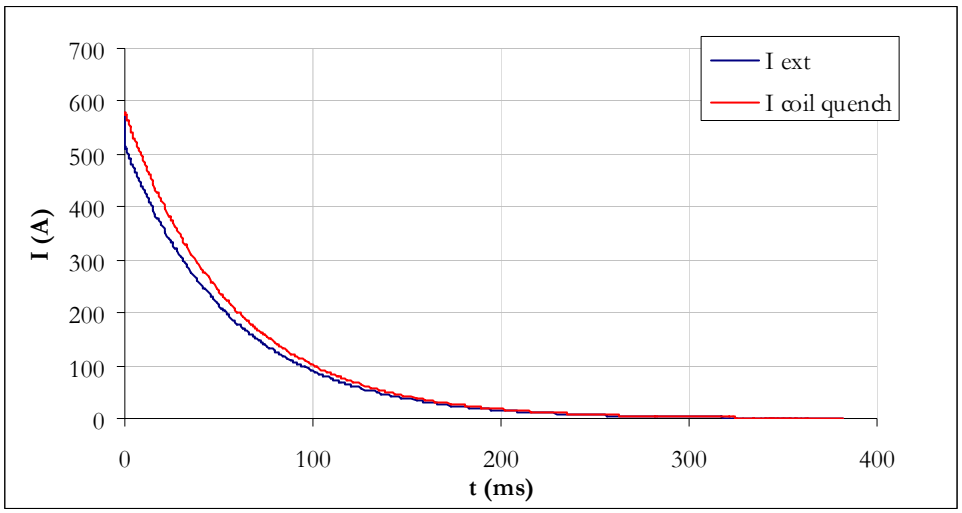

Figure 29. Discharge of the current in the simulated configuration which corresponds to the lowest hot spot temperature.

2.4. Conclusions

The design of the undulator with a 280 mm or 140 mm period to measure the beam profile on the protons and lead ions LHC beams has been presented. After an initial 2D optimization, a 3D model simulation has been made. It allowed verifying that the field uniformity in the transverse dimension doesn't perturb the beam dynamics and that the fringe field seen by the other circulating beam is negligible. The optimization of the circuit of protection has been performed by using the quench simulation code developed during this work of thesis.

CHAPTER 3

Nb_3Sn TECHNOLOGY: BASIC PRINCIPLES

At present Nb_3Sn is the only superconductor which may make possible the manufacture of accelerator magnets in the range of 15 T and above, because at such values of fields it is still able to sustain high critical current densities. The superconducting properties of this composite are determined by its ordered crystallographic structure, which makes the material such brittle that it is impossible to extrude and drawn down the wire when Nb_3Sn is already formed. To overcome this, the wire is manufactured with the more ductile un-reacted components of Nb_3Sn. After the wire has been drawn at useful dimensions, the superconductor is formed by an appropriate heat treatment, which may also strongly influence the final properties of the strand. In this chapter the typical steps of the heat treatment are presented. A too aggressive one may increase the dimensions of the filaments over the limiting value, determined by the flux jumping stability criteria, as described at the end of the chapter.

Since 90's some dipole magnets based on the Nb_3Sn technology have been built to demonstrate the feasibility of magnets able to produce fields higher than 10 T. The first dipole was a 50 mm aperture cosθ type manufactured at the Twente University and tested at CERN, which reached about 11 T at 4.4 K [1], [2]. At present in the context of an international collaboration which involves Lawrence Berkeley National Laboratory and Fermilab with CERN, a world record of about 16 T at 4.3 K has been reached with the HD-1 H block type model [3], [4].

3.1. Nb_3Sn properties

Nb_3Sn belongs to the family of the A15 intermetallic compounds. This term refers to a cubic crystals represented by the general form A_3B, where the element A belongs to the group III B, IV B and V B or some transition metals and B to the IVA, VA and VI A transition metals. These compounds exhibit a high grade of order, responsible for the excellent superconducting properties of the majority of them (46 superconductors of 76 A15 known compounds).

In Figure 1 the critical temperature and field of the A15 compounds are plotted.

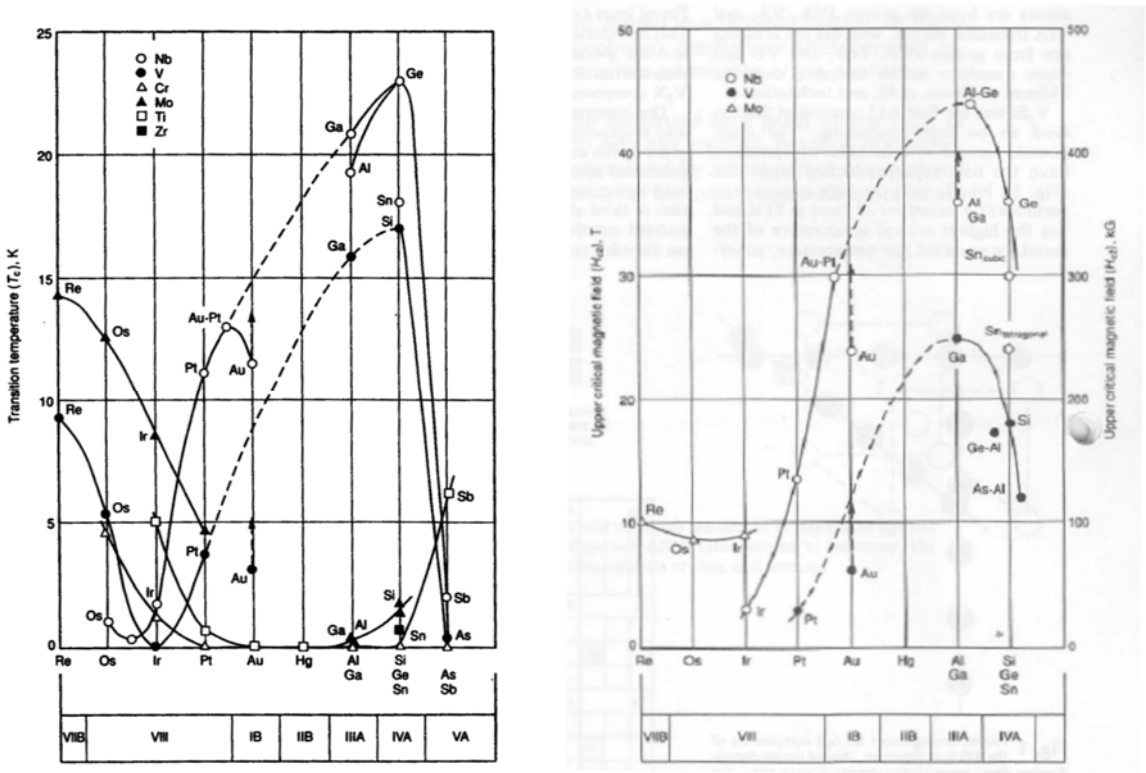

Figure 1. Critical temperature of several A15 compounds [5].

The compounds which contain Nb or V exhibit the best superconducting properties. In particular Nb_3Ge has held the record critical temperature for 20 years, but it is very difficult to obtain high critical current density in layers that are thick enough to be of practical usability. In Figure 2 the critical current density of the most performing superconductors at 4.2 K in function of the magnetic field is shown.

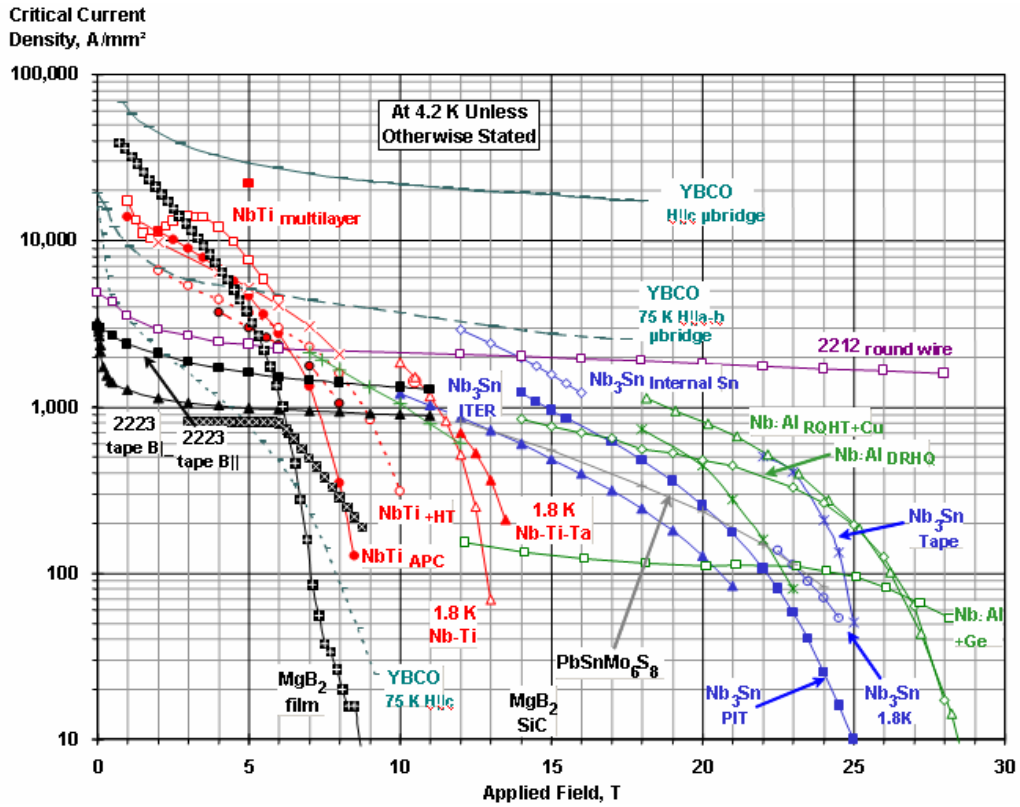

Figure 2. Critical current density of the most performing superconductors at present [6] at 4.2 K.

Nb_3Sn is the one which has a highest critical current density in the range beyond 15 T. The high temperature superconductors (BCO, YBCO, 2212 and 2223) are difficult to produce in the length necessary to manufacture a magnet. From the same graph of Figure 2 it can be also noticed that the critical current density depends on the manufacture process of the wire. The internal tin diffusion process at present is the one which allows obtaining the highest critical current density, but it is critical for flux jumping instability, because of the large dimensions of the filaments[1].

3.2. The manufacturing process

Because of its brittleness Nb_3Sn cannot be reacted before the extrusion and the drawing, and it is then necessary to assembly the billet with the more workable un-reacted components, which will form the Nb_3Sn, and only after the extrusion and the drawing to the desired dimension, the superconductor is formed.

[1] More details can be found in the last section of this chapter.

At present four processes are used to manufacture Nb_3Sn strand:

- Bronze process
- Internal Tin process (IT), which includes Rod Restacked Process (RRP) and Hot Extruded Rod (HER)
- Modified Jelly Roll (MJR) process
- Powder in Tube (PIT) process

In consideration of the fact that the bronze or the other alloys in the strand after the reaction to form Nb_3Sn do not play any role from the electrical point of view and that the area of the superconductor is difficult to estimate, for this superconductor it is common practice to define the critical current density over the non-copper area of the wire. This is referred as non-copper J_C.

The continuous research brought to an improvement of the non-copper critical current density of more than a factor 2 in the last 15 years, as shown in Figure 3.

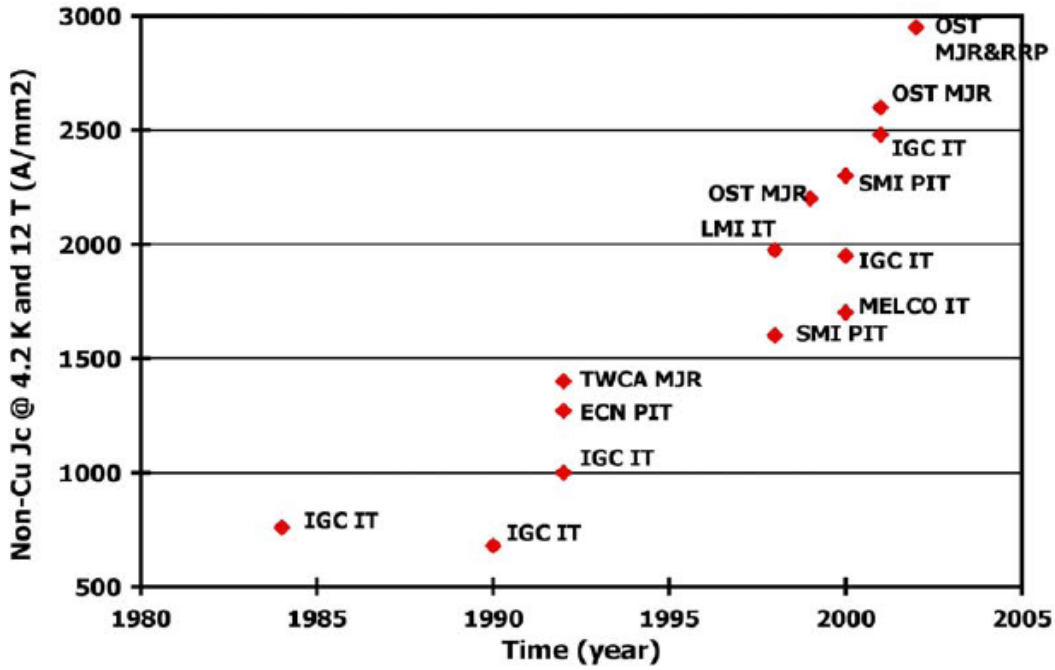

Figure 3. Improvement of the non-copper critical current density for the different processes [7].

The state of the art is the RRP manufactured by the Oxford Instruments Superconducting Technology, which reached a non-copper J_C of 3000 A/mm^2 at 12 T and 4.2 K. This is the strand designed for the LHC undulator described in this thesis.

In the next sections the several wire manufacture processes are described.

3.2.1. Bronze process

The strand manufactured with this process is produced from billets made up of Nb rods inserted into holes drilled in a CuSn alloy matrix. Because of the high resistivity of the bronze at low temperature copper is added to deviate the current in case of quench. The copper is protected by some barriers in niobium, tantalum or vanadium to prevent its pollution during the heat treatment [8], [9]. If Nb is used it also contributes to the volume of Nb_3Sn, but it also causes an increment in the magnetization effect. To avoid this effect tantalum can be used instead of the niobium also if it is less ductile and more expensive. In case of barriers in vanadium it has been found that it may diffuse into Nb_3Sn, thus degrading the critical current density [10], [11].

The cross section of a strand produced with the bronze process in shown in Figure 4.

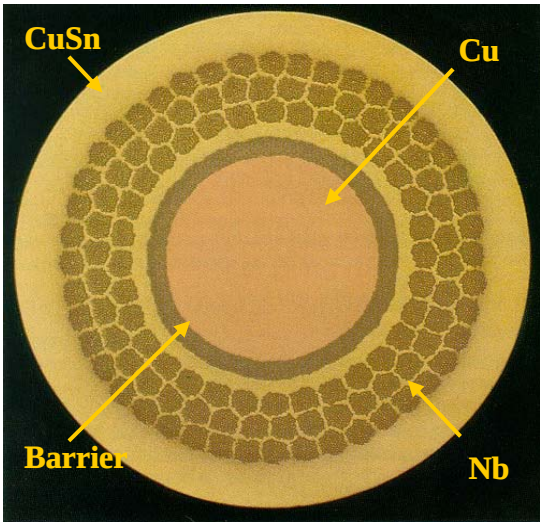

Figure 4. Cross section of a strand produced with the bronze process.

An disadvantage of this process is the limitation on the disponibility of tin in the bronze matrix. The only ductile phase of the alloy copper-tin, which can be easily worked is the α, which, as can be seen in the phase diagram of Cu-Sn of Figure 5, has a limited content of tin (15.7%wt).

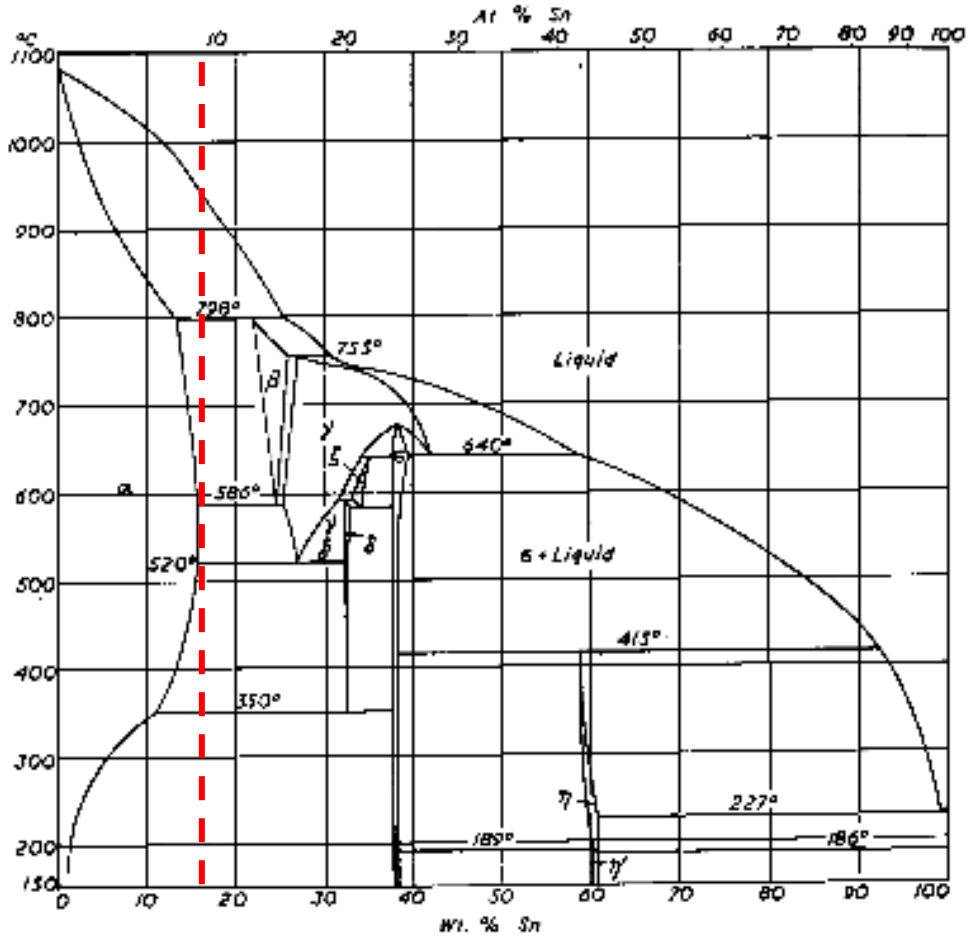

Figure 5. Copper tin phase diagram [12].

To ensure that enough tin is present in the strand to react with the niobium, it is then necessary to design a strand with high bronze over niobium ratio, but in this way also diminishing the critical current density. Another disadvantage of this manufacturing process is the large hardening coefficient of the α phase, which makes necessary numerous intermediate annealing steps during the drawings to recover the mechanical properties.

Several japanes manufacturers produced a strand able to achieve 950 A/mm^2 at 12 T and 4.2 K [13], [14].

3.2.2. Internal tin process (IT)

The internal tin process (IT) allows eliminating intermediate annealing steps and increasing the fraction of tin for the Nb_3Sn formation. The typical cross section of a strand manufactured by this process is shown in Figure 6.

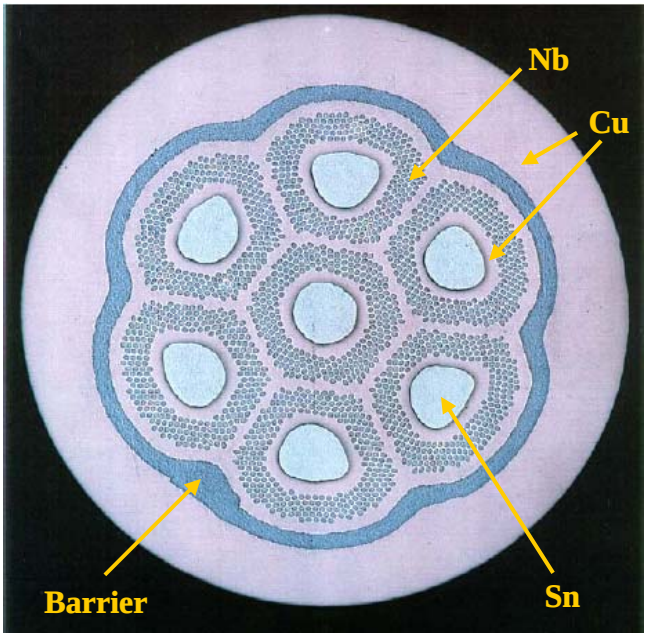

Figure 6. Cross section of an internal tin strand [15].

Internal tin process is divided in two phases. The first one is the formation of the sub elements, placing niobium rods around a tin core in a copper matrix. The sub elements are then assembled, extruded and drawn. It is only during the heat treatment that the tin from the pools diffuses into the copper matrix of each sub element to form bronze, which will be used with niobium to form the Nb_3Sn. As in the case of the bronze process pure copper is added separated by anti-diffusion barriers.

This process eliminate the intermediate annealing steps, because a pure copper matrix with a low work-hardening coefficient is used. Another important advantage is that the quantity of tin in the strand is not limited by its solubility in the α phase of the CuSn alloy, then the bronze over niobium ratio can be made smaller than in the case of the bronze process, resulting in an increasing of the non-copper critical current density.

In this process it is not possible to make the hot extrusion after the insertion of the tin rods have been inserted into the copper matrix, because of the low melting temperature of the tin (231.93ºC). A method to overcome this limitation is to insert the tin as late as possible during the manufacturing process. This method is used by the Oxford Instruments Superconducting Technology (OI-ST) with the Rod Restacked Process (RRP). The billet by the niobium rods are placed in the copper matrix, which fills also the spaces where in a subsequent step the tin will be inserted. Only after this assembly is extruded and drawn down to an intermediate dimension, the tin rods are

inserted in holes drilled into the copper matrix. The billet is then cold drawn down to the final dimensions. This technique presents some critical points. The drilling of the holes requires great care and tight tolerances and can't be done at too small size. Another critical point of the RRP is the cold drawing performed on a composite assembly that may not be tightly compacted; particular attention has therefore to be used to avoid breakages during working.

An alternative solution is to fill the holes made at the beginning of the manufacturing process with common salt to be removed and replaced by the tin only after the extrusion and the drawing. This technique, called Hot Extruded Rod (HER), developed by the OI-ST is still under study [16], [17].

During the IT the densely packed filament arrays, deformed during the extrusion and the drawing, may favorite the interfilament bridging during the heat treatment. It causes the filaments to behave as a unique larger filament resulting in large magnetization effect and in instability for flux jumping especially at low fields, as discussed in details in Section 3.4. . A trivial method to reduce this effect is to increase the filament spacing, but this gives a decrease of the non copper critical current density. Another possibility, developed by Europa Metalli in collaboration with LASA (INFN Lab, Milano) is to increase the number of the sub elements and to insulate them with individual barriers, as shown in Figure 7.

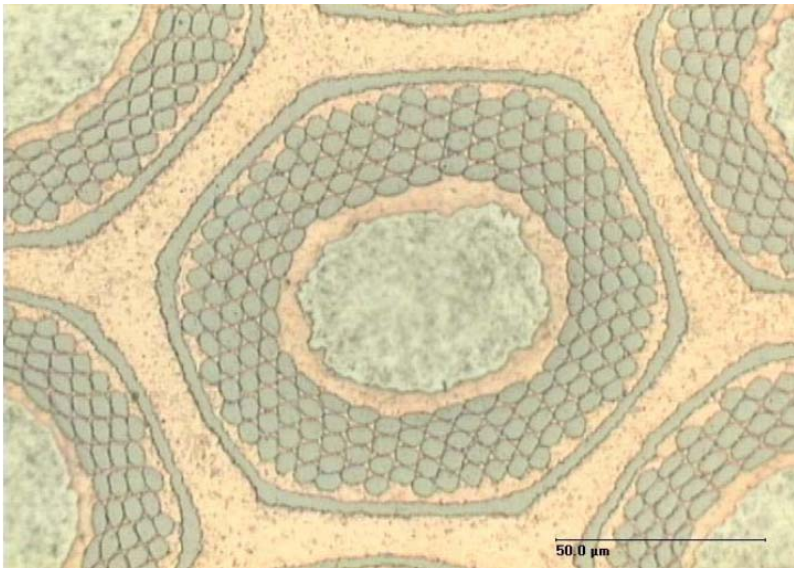

Figure 7. Cross section of the not-reacted strand developed at LASA. The sub element size is smaller and protected by a barrier (courtesy of L. Rossi, CERN AT MAS Group Leader).

In this way the effective filament diameter, which in the worst cases is equal to the sub element dimension, can be made smaller.

The IT process allows to achieving value of non copper critical current density well above the ones obtained with the bronze process. The strand developed by the LASA in collaboration with Europa Metalli reached 1975 A/mm^2 at 4.2 K and 12 T in 1998. This value has been increased by the Intermagnetics General Corporation (IGC) in USA which reported a value of about 2500 A/mm^2 at 4.2 K and 12 T in 2001 [18]. The highest non copper critical current density at present time has been made by the OI-ST with a non copper current density of about 3000 A/mm^2 at 4.2 K and 12 T [19].

3.2.3. Modified Jelly Rod process (MJR)

This process has been developed at the beginning of the 80's at the Wah Chang Albany (TWCA) in Oregon [20], [21] and at present it is under study at the OI-ST [22]. In this manufacturing process the niobium is in the form of a metal sheet, rolled up with a sheet of copper or bronze; cylindrical rods are inserted in the center and after everything is enclosed into a copper tube to be extruded and drawn down [23]. The cross section of the resulting strand is shown in Figure 8.

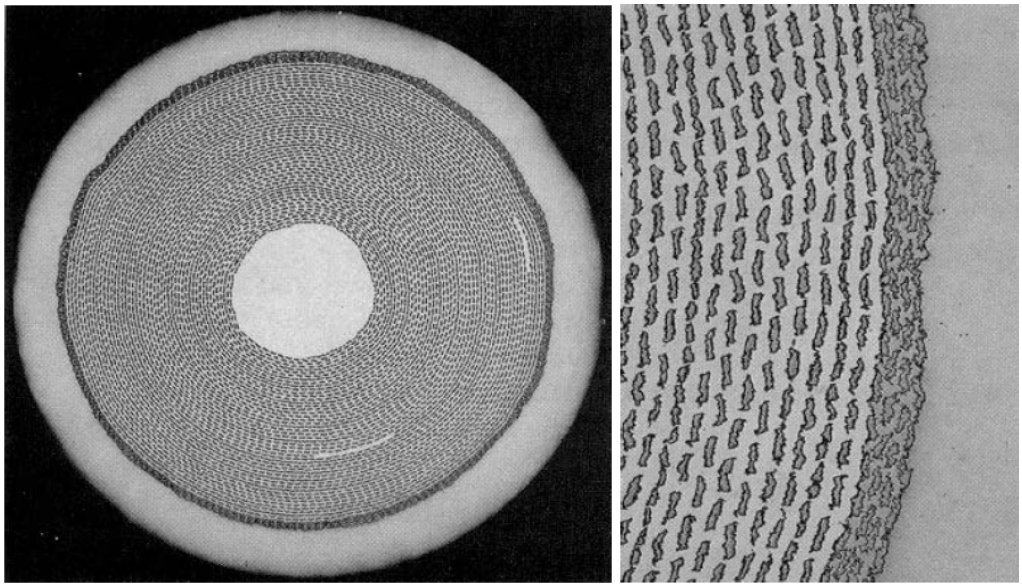

Figure 8. Cross section of a strand produced with the MJR method.

The effective filaments diameter is more difficult to be controlled than in the case of the bronze or the internal tin process.

The best value of non copper critical current density achieved in 2002 is of 2900 A/mm^2 at 4.2 K and 12 T [24].

3.2.4. Powder In Tube process (PIT)

This technique has been developed at the Energy Research Center of Netherland (ECN) and at the University of Twente in the early 70's. A fine grain (less than 3 μm) powder of Nb_2Sn mixed with tin is put in a niobium hollow cylinder inserted into a copper tube. This is drawn down to a rod of small diameter; the rods are then cut and stacked into a copper tube with a solid copper bar at the center and extruded and drawn down as in the other processes. In Figure 9 the cross section of a strand produced with the PIT is shown.

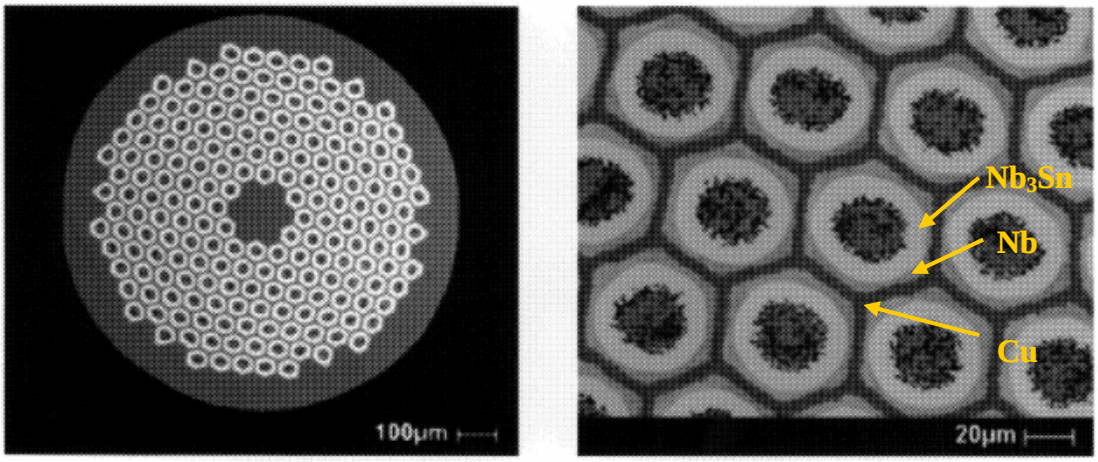

Figure 9. Cross section of a strand manufactured with the powder in tube process [25].

During the first part of the heat treatment Nb_6Sn_5 is formed and after the precipitation to the Nb_3Sn, which grows from the inner side of the niobium tube, occurs. In the second picture of Figure 9 the rich in tin core, the reacted Nb_3Sn the unreacted niobium and the copper starting from the center towards the outside are visible. The unreacted niobium is intentionally left to be used both as a mechanical reinforcement and as a barrier between the copper and the Nb_3Sn.

This process allows controlling the magnetization effects mainly determined by the inner and the outer radius of the ring of the reacted Nb_3Sn in each tube of dimensions smaller than in the other processes. The proximity of the tin sources to the niobium allows appreciably reducing the duration of the heat treatment. This fact, beyond being an economic advantage, permits also to avoid an excessive grain growth, which are to be maintained sufficiently small for an efficient flux pinning and may contribute to produce homogeneous properties over the cross section.

The maximum non copper critical current density measured in 2001 [26] is 3200 A/mm^2 at 4.2 K and 10 T in 2001, which corresponds to 2230 A/mm^2 at 4.2 K and 12 T.

3.3. The heat treatment

The heat treatment to form Nb_3Sn starting from the ductile components of the strand is a crucial step in magnet manufacturing, because it strongly influences the ultimate superconducting and mechanical properties of the wire.

As it can be seen from the phase diagram of Nb-Sn, shown in Figure 10, the only solid stable phase at temperature beyond 930ºC is the Nb_3Sn.

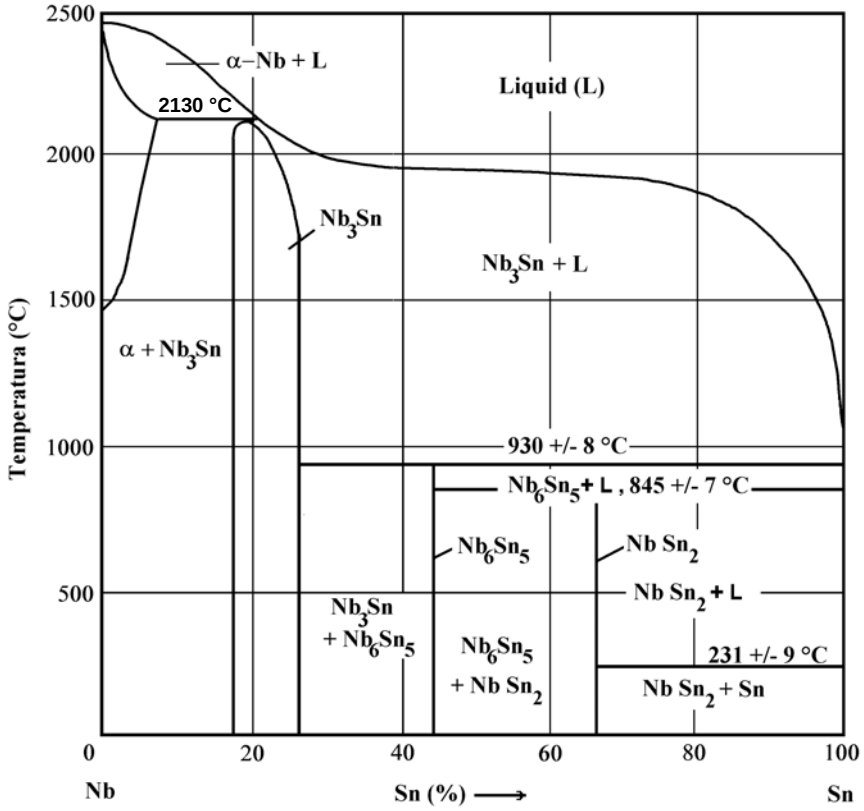

Figure 10. Nb-Sn phase diagram.

For many years then Nb_3Sn has been formed by heating Nb tape in a tin bath at temperatures of 930ºC or higher to avoid the formation of the other phases (Nb_6Sn_5 and $NbSn_2$). At present the A15 compound is formed at a temperature of about 700ºC, exploiting the fact that the copper matrix acts as a catalytic agent for the preferential growth of Nb_3Sn phase at the expense of the other non superconducting Nb-Sn phases.

For Nb_3Sn the dominant source of flux pinning are the grain boundaries, as evident from the plot of Figure 11.

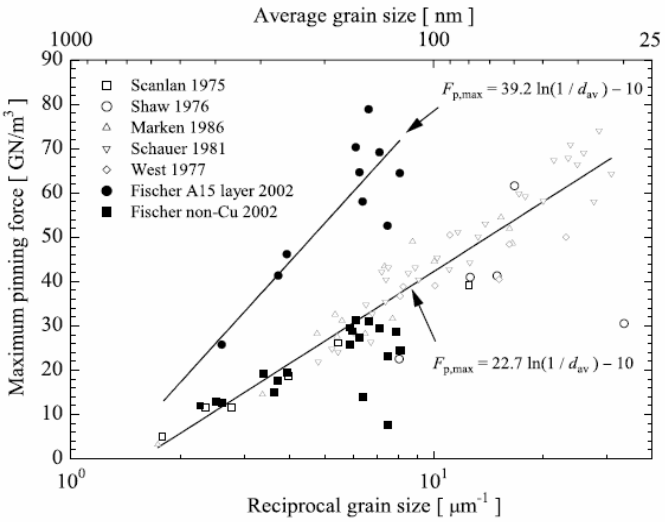

Figure 11. Maximum pinning force in function of the inverse of the grain size [27].

In order to obtain high critical current densities it is then necessary to produce a fine grain structure, which is in conflict with the long time necessary to form a consistent volume of superconductor. The optimum process is obtained by balancing these two issues. In particular it has been estimated that the optimum grain size to achieve the ideal limit of one pinning site per fluxoid at 12 T is 14 nm [34].

The number of the steps, the temperatures and the durations of the heat treatment are different for the several manufacturing processes, but some common guidelines can be identified. For a strand manufactured with the bronze process a single-stage treatment at a temperature between 650ºC and 700ºC is performed, whereas for example in case of IT wire some preliminary steps at temperature lower than the melting one of tin are necessary.

In Figure 12 the typical temperatures of the three steps of the heat treatment for an IT strand are indicated on the Cu-Sn phase diagram.

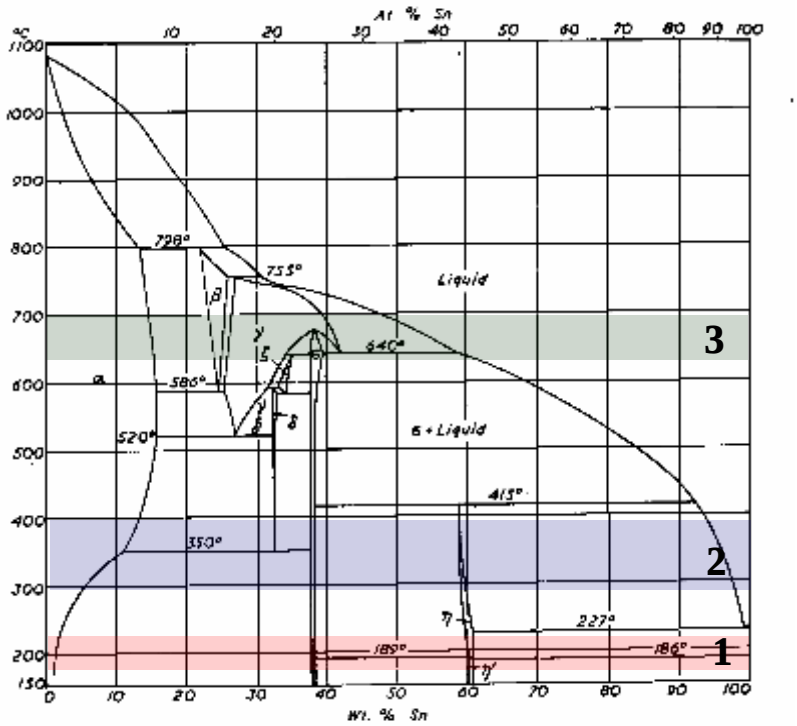

Figure 12. Copper-Tin phase diagram. The temperatures of the three steps of the heat treatment are indicated.

The scope of the low temperature steps 1 and 2 of the heat treatment is the diffusion of the tin into copper to form higher melting point phases. This is performed to avoid the presence of tin liquid phases, which during the high temperature step may cause the strand deformation, due to the loss of structural strength, or that the tin may break the barriers polluting the stabilizer copper or cause the motion of the Nb filaments.

It has been experimentally observed that the transformation of pure tin into higher melting point phases is very inefficient under the tin melting temperature (after 1 week at 210º a large fraction of the tin is still unreacted). An acceptable efficiency is reached for a temperature of 400ºC (at temperatures higher than 440ºC voids and segregations which may result in cracks), but crossing the tin melting point by a direct ramp may be enough to provoke leakages in the strand. A preliminary dwell is then performed at temperature below the tin melting point to form a layer of a solid phase which acts as a container again the tin overpressure for the rest of the heat treatment. A micrograph of the strand after this step is shown in Figure 13.

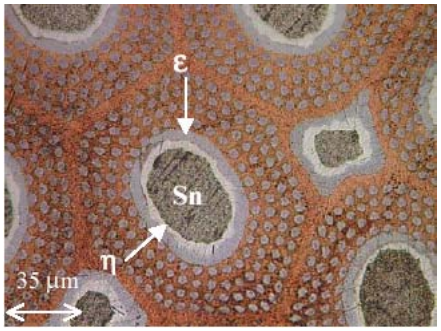

Figure 13. ε phase which acts as a container for the rest of the heat treatment [28].

The final step of the heat treatment, generally performed at temperatures between 650ºC and 700ºC for IT strands, is to diffuse the tin contained in the bronze to form the Nb_3Sn with niobium. The critical temperature at 0 T and zero strain and the upper critical magnetic flux density at 0 K and zero strain are strongly influenced by the stochiometry of the final A15 compound, as shown in Figure 14.

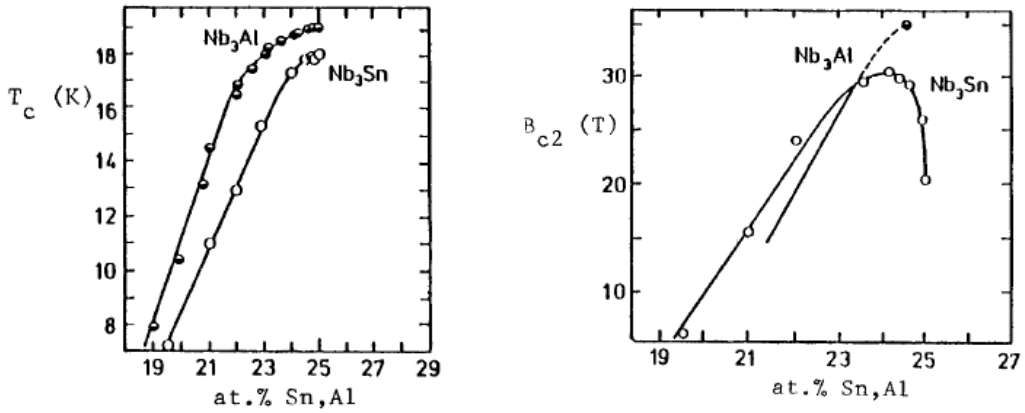

Figure 14. Critical temperature at zero strain and field and upper critical magnetic field at 0 K and zero strain of Nb_3Sn in function of the tin content [29].

Both critical temperature and field are proportional to the tin content until it is smaller than 23at% and they saturate or diminish for higher tin content. This behavior is attributed to transition from a cubic to tetragonal phase for tin content exceeding 24.5at% at temperature below 43 K [30]. To avoid this transformation the cubic structure is stabilized by doping niobium with tantalum [31] or titanium [32], which acts also as catalyst for the formation of the Nb_3Sn [33].

3.3.1. De-sizing

The coils are manufactured following two procedures: *React & Wind* (RW), which consists in reacting the superconductor and then winding the coil and the *Wind &*

React (WR), which reverses these two steps. The RW procedure is applicable only in case the bending radius is large enough to a level that doesn't degrade the performances of the superconductor [34]. This technique is still under experimentation and the majority of the coils is manufactured with the WR procedure. In this case the wire has to be insulated before the heat treatment, and then the insulation must be able to resist to the high temperatures of the heat treatment necessary to form the superconductor and this excludes the use of polyimide tapes.

The insulation is commonly made in two steps. Before the heat treatment the strand is wound by a mineral fiber cloth, which provides conductor spacing to facilitate the penetration of the resin and limits the crack propagation in the resin. After the heat treatment the coil is put into a mold and vacuum impregnated with epoxy resin. It increases the turn to turn breakage voltage, gives a rigid shape to the coil and prevents the occurrence of quench for small mechanical disturbances.

The fiber wrap has to be able to resist to the high temperature step of the heat treatment, it has to be as thin as possible to maximize the overall critical current density, easy to be wrapped and ensure physical continuity along the conductor to limit the risk of turn to turn shorts. The adopted solution is a glass fiber made up of few μm filaments assembled in a yarn. The cheapest and most used fiber is the E Glass, which has a too low recrystalization temperature of about 650ºC to be used for the Nb_3Sn coils. The S and the S2[2] Glass in USA (R Glass in Europe), with a crystallization temperature above 750ºC, are suitable for this application. Sizing the filaments that form the yarn with organic compounds is necessary to protect them from abrasion and to lubrificate and reduce the filament to filament friction and yarn to contact surface. These organic compounds undergo a graphitization-like decomposition that leaves electrical conducting residues at a temperature of about 700ºC. It is then mandatory to remove them before the final step of the heat treatment (de-sizing). If the exact composition of the chemical composition of the sizing and of their solvents is known, the de-sizing can be done by chemical dissolving. Often the exact composition of the sizing is not given by the wire manufacturers and this procedure doesn't ensure the completeness and the uniformity of the de-sizing. The other possibility is to make the de-sizing by carbonization in air, which happens at a

[2] S Glass and S2 Glass differ only for the purity, higher in the S2 Glass.

temperature between 200ºC and 250ºC for E Glass and S Glass, which coincides with the range of the first steps of the heat treatment.

The first two steps of the heat treatment have then the double scope to prepare the composite for the grown of the Nb_3Sn and to perform the de-sizing.

3.4. Flux jump instability

Flux jump instability is the major source of disturbance besides the mechanical one in superconducting magnets. It may cause a wire to quench at temperature, magnetic field and current density well below the critical curve of the superconductor. This phenomenon, being connected to the resistive motion of the fluxoids under the action of an external field, may happen in the mixed state of the type II superconductors and it can be demonstrated that it is more dramatic for high critical current density superconductors. In this section the elements to understand the phenomenon and justify the experimental results presented in the next chapters are described. More details can be found for example in [35], [36], [37].

According to their comportment in an external magnetic field the superconductors are divided into two types.

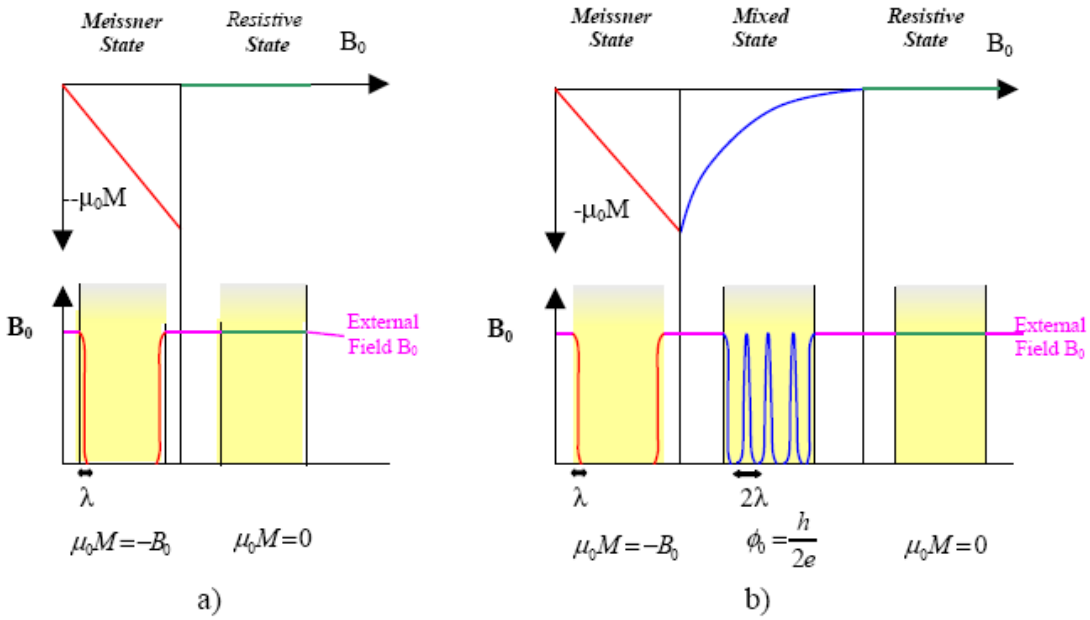

Figure 15. Magnetization of superconductors of type I and II [28].

A superconductor of type I in presence of an external magnetic field which is smaller than the critical one B_{C1} behave as a perfect diamagnetic material, fully expelling the

flux lines, otherwise the interior of the superconductor is not shielded and the field can fully penetrate, as schematically shown in Figure 15. This kind of superconductors is not suitable for magnets because of the low value of B_{C1}, normally of the order of no more than 1 T at 4.2 K. The materials used to manufacture magnets are the superconductors of type II, which have an intermediate state between B_{C1} and another critical field B_{C2}. This state, said mixed phase, is characterized by the presence of flux vortex or fluxoids, composed by a supercurrent ring which circulates around a normal resistive core. For Nb_3Sn the radius of the ring and of the core are 124 nm and 3.6 nm respectively [38]. Because of their normal core, fluxoids motion induces power dissipation, which, if not limited or promptly evacuated, may initiate a quench. In practical superconductors, fluxoid motion is prevented bounding them to "pinning" centers, which can be the lattice imperfections, such impurities sometimes appositely added to the pure superconductor, defects or ground boundaries.

Let's consider a slab of type II superconductor. When a magnetic field is applied to the slab as indicated in Figure 16, surface currents at very high current density to shield the interior of the superconductor appear.

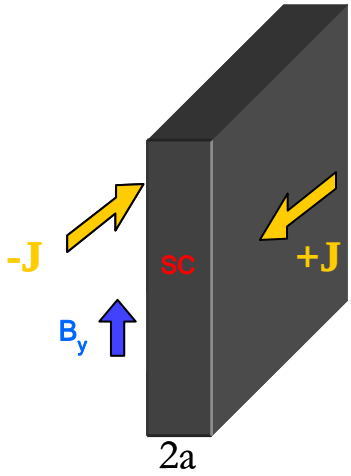

Figure 16. Slab of a superconductor in an external magnetic field.

Because this density exceeds the critical one, the surface current decays resistively and the magnetic field penetrates inside the slab until the current density reaches the critical value. The net result is that all the regions of the slab immersed in a magnetic field parallel to the broad face carry currents at critical current density or no current at all (critical-state model).

This state becomes instable if the slab is subjected to a heat pulse also smaller than the one corresponding to the minimum quench energy. A thermal perturbation, in fact,

causes a rise of the temperature and, consequently, a decrease of the critical current density. The current density must therefore decreases somewhere in the slab, and this lets penetrate the magnetic field deeper into the slab. The resulting resistive flux motion generates heat, which raises still further the temperature. This increment of the temperature decreases the critical current density and so on. A number of stability criteria have been developed, but the most common used are the adiabatic and the dynamic ones, which both involve the fine subdivision of the superconductor.

A criterion for the stability without considering the interaction of the superconductor with the surroundings (adiabatic stability criterion) can be found writing down the heat balance in case a quantity of heat Q_G is given to the superconductor. It can be derived [39] that the effective specific heat for unit of volume γC_e, where γ is the density of the superconductor, is reduced by the energy stored in the screening currents represented by the second term in [39]:

$$\gamma C_e = \frac{Q_G}{\Delta T} = \gamma C - \frac{\mu_0 {J_C}^2 a^2}{3(T_C - T_R)} \tag{1}$$

where T_C is the critical temperature, J_C the critical current density, T_R is a reference temperature and C the specific heat of the superconductor without the currents, assuming a linear fall-off of J_C in function of the temperature. If the right side of the equation (1) is equal to 0 an infinitesimal disturbance causes the temperature grows without limitation (flux jump). This is avoided if the stability parameter β [39] is smaller than 3:

$$\frac{\mu_0 {J_C}^2 a^2}{\gamma C(T_C - T_R)} \equiv \beta < 3 \tag{2}$$

In a more general derivation, without assuming the linear fall-off of the critical current density on the temperature, true for NbTi, it can be derived [40] that the dimension of the slab has to be kept smaller than:

$$a = \sqrt{\frac{3C}{\mu_0 J_C \left| \frac{\partial J_C}{\partial T}(T, B) \right|}} \tag{3}$$

where the derivative of the critical current density is calculated at the operational temperature and field.

The stability can be improved slowing the motion of the fluxoids, by inserting the superconductor filaments in a copper or aluminum matrix, and improving the cooling (dynamic stability).

Including the heat brought away by convection of the refrigerant and the presence of the matrix, it can be found [40] that the filament dimension has to be less than:

$$a < \sqrt{\frac{32\,\lambda_{Wire}\,k_{SC}(T,B)}{\rho_{Matrix}(RRR,T,B)\,J_C\left|\frac{\partial J_C}{\partial T}(T,B)\right|}} \tag{4}$$

where $\rho_{Matrix}(RRR,T,B)$ is the resistivity of the matrix, λ_{Wire} is the copper over superconductor ratio and $k_{SC}(T,B)$ is the thermal conducibility of the superconductor. Both criteria described in this section involve a fine subdivision of the superconductor. For NbTi this dimension must to be less than about 100 μm also if a smaller one, normally about 50 μm, is usually used to ensure a certain margin of safety. For superconductors like NbTi flux jumping is then a solved problem. Because of the dependence of the maximum dimension of the filaments on the inverse of the critical current density and its derivative with respect to the temperature, flux jumping is a more dramatic problem for high critical current superconductors and in particular in the region of the plane B-I at low fields, where these quantities are larger. In case of Nb_3Sn particular attention has to be paid also to the heat treatment to assure that the dimensions of the filaments remain under the limit determined by the stability criteria.

3.5. Conclusions

The very ordered structure of the Nb_3Sn confers to this material its very good superconducting properties, which make this A15 compound suitable for the manufacture of magnets working at field up to 15 T and above, but this order is also responsible of the brittleness of the superconductor. Because of this, it is necessary to manufacture the wire with the more ductile un-reacted precursors of the Nb_3Sn, before performing the heat treatment to form the superconductor. In this chapter the several wire manufacturing processes and the typical steps of the heat treatment, have been presented. The brittleness of the A15 compound makes also the technique of the Wind & React the only one pratically applicable to manufacture the Nb_3Sn magnets. In this case the insulation has to be able to resist to the temperature up to 700ºC. Glass fiber

is normally used. In this chapter the most diffused techniques developed to de-size the binder to avoid the formation of electrical conducting residues at the high temperature step of the heat treatment are presented. The last part of the chapter is dedicated to the flux jumping, which may make quench a superconductor in the high critical current density region. This effect can be reduced by subdividing the superconductor in fine filaments, but a too aggressive heat treatment may increase them, making it a problem for the stability of the superconductor.

CHAPTER 4

SETTING-UP AND EXECUTION OF EXPERIMENTAL TESTS TO CHARACTERIZE A RRP WIRE MADE BY OI-ST

The design described in chapter 2 fixed the maximum field on the conductor at 10 T, which excludes the use of NbTi as a conductor in favor of Nb_3Sn. The state of the art for this material is the RRP, 0.8 mm diameter, 54 sub-elements wire produced by the Oxford Instruments, Superconducting Technology (OI-ST), able to reach 3000 A/mm^2 at 4.2 K and 12 T. This value, which mainly depends on the strand design, is also influenced by the high temperature step of the heat treatment to form the superconductor. An important part of the experimental work was then the setting-up and the calibration of the system used to form the Nb_3Sn. To check it and at the same time to characterize the wire, critical current density (Jc) and Residual Resistivity Ratio (RRR) measurements have been performed and compared to the results given by OI-ST. These tests have thereafter been followed by flux jumping instability measurements, which revealed the presence of a region of instability in certain conditions of magnetic field-current. As the undulator working point falls inside this region of instabilities, two alternatives have been explored: a different heat treatment and an alternative design of the undulator. The new heat treatment has been

used directly during the manufacture of the coils of the test mini-dipole and an alternative design of the undulator with reduced current has been done.

4.1. The strand

Considerable advances have been reached for the value of the critical current density of Nb_3Sn, thanks to the strong interest in this material for the high field accelerator magnets both in Europe and in USA. The state of the art for this composite is the Rod Restacked Process (RRP), 54 sub-elements strand made by the OI-ST, able to reach a non-copper critical current density of almost 3000 A/mm^2 at 12 T and 4.2 K [1]. The micrograph of a sample of this wire after being impregnated and polished by abrasive papers is shown in Figure 1.

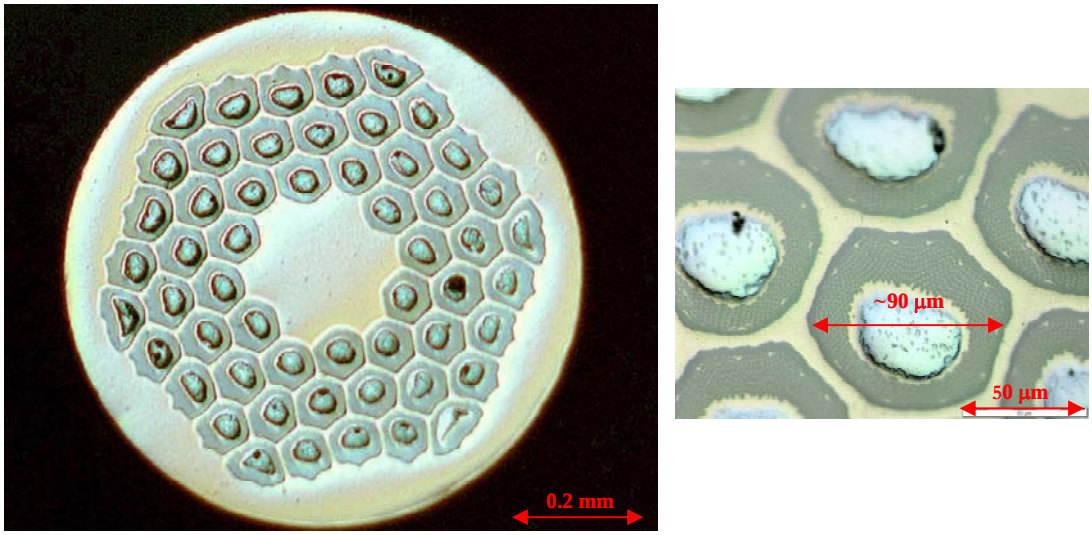

Figure 1. Micrograph of the RRP strand for the LHC undulator before the heat treatment.

This is a circular strand with large sub-elements which measure about 90 µm. The dimensions and the other specifications of the wire are reported in Table 1.

Bare size (mm)	Insulated size (mm)	Twist	Non Cu fraction	Sub elements	Insulation
0.800±0.005	0.930±0.005	12 mm	53 %	54	S2 Glass

Table 1. OI-ST strand specifications.

The strands for the test have been heat treated according to the procedure optimized by OI-ST and shown in Table 2.

	Atmosphere	Ramp		Plateau	Ramp		Plateau
Pre reaction	circulating air	Rate	Target	100 h	Rate	Target	2 h
		25 ºC/h	205ºC		25 ºC/h	325 ºC	
Reaction	vacuum	Ramp		Plateau	Ramp		Plateau
		50 ºC/h	400 ºC	48 h	50 ºC/h	695 ºC	25 h

Table 2. OI-ST optimized heat treatment.

In this sequence the typical steps described in the third chapter of the heat treatment to react the Nb_3Sn the previous chapter can be recognized: the pre-reaction to form the bronze and for the de-sizing, and the first step of the reaction to increase the rate of the bronze formation. Because of the burning of the insulation binder the first part of the heat treatment needs oxygen, and then it must be performed in air, whereas the rest of the reaction is made in inert atmosphere to reduce the risk of oxidation at higher temperatures. It has been experimentally demonstrated that the critical current density and the RRR are almost independent from the composition of the bronze after the pre-reaction, whereas they are more influenced by the last step of the heat treatment [2]. The temperature and the duration of this phase have been suggested by OI-ST after an optimization of it. The results are shown in Table 3.

	25 h	50 h	75 h	100 h	180 h	200 h	220 h
695 ºC	**2931/89**	2930/43	2932/18				
675 ºC			2608/22	2895/18	2969/12		2684/?
665 ºC				2796/31	2700/9		
650 ºC					2901/38	3044/21	

Table 3. Non-copper critical current density at 12 T and 4.2 K (underlined) and RRR for several final steps of the heat treatment to form the Nb_3Sn. The chosen last step for the heat treatment gives the best combination Jc/RRR (bold).

The possibility indicated in bold has been chosen, because it allows having one of the higher non-copper critical current density and a RRR of about 100. A low value of RRR, in fact, could indicate a pollution of the copper stabilizer because of the breakage of the protection barriers. This must be avoided because it would degrade both the resistivity, causing an overheating of the winding in case of quench, and the thermal conducibility of the copper stabilizer, making worse the dynamic flux jumping stability.

In Table 4 the critical current, current density and n value of the strand after the heat treatment of Table 2 as a function of the magnetic field at 4.2 K are shown.

	12 T	13 T	14 T	15 T	16 T
Ic (A)	764	629	509	404	314
Jc (A/mm^2)	2929	2411	1951	1549	1204
n value	49	40	37	30	26

Table 4. Strand critical current (Ic) measured with the 0.1 μV/cm criterion, non-copper critical current density (Jc) and n value at 4.2 K as a function of the magnetic field measured by the OI-ST after the heat treatment indicated in Table 2.

These experimental data are fitted very well by the parameterization of Summers et al. assuming zero strain in the superconductor [3]:

$$J_c(B,T) = \frac{C_0}{\sqrt{B}}\left[1-\frac{B}{B_{c20}\left[1-\left(\frac{T}{T_{c0}}\right)^2\right]\left\{1-0.31\left(\frac{T}{T_{c0}}\right)^2\left[1-1.77\ln\left(\frac{T}{T_{c0}}\right)\right]\right\}}\right]^2\left[1-\left(\frac{T}{T_{c0}}\right)^2\right]^2 \quad (1)$$

where B_{c20} is the upper critical field at 0 K, T_{c0} is the critical temperature at 0 T and C_0 is a factor of normalization. In Figure 2 the comparison between the measurements and the fitting curve is shown.

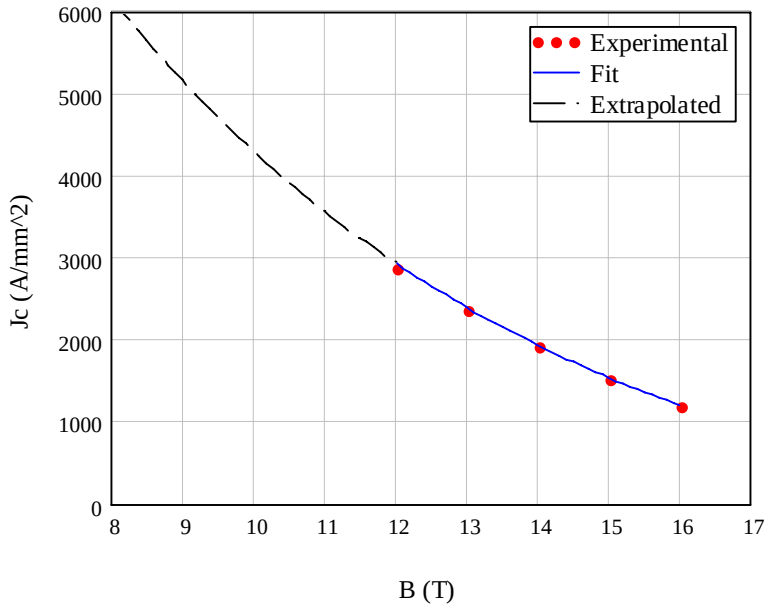

Figure 2. Fit of the non-copper critical current density at 4.2 K from the data given by OI-ST. In the same plot also the extrapolation for smaller fields is indicated.

The values of the parameters resulting from the fit, $B_{c20} = 26.3\,T$ 26.3 T, $T_{c0} = 18.2\,K$ 18.2 K and $C_0 = 42410\ A \cdot T^2 / mm^2$, are very close to the values of 26 T, 18 K and 40000 $AT^{1/2}/mm^2$ respectively [4] found in literature. This fit has been used both to rescale the critical current density from 4.2 K to 1.9 K to check the result of the measurement of the critical current density at CERN, and to extrapolate the values of the critical current at fields lower than 12 T used for the magnetic design.

All heat treatments on the strands described in this chapter have been performed according to the sequence of Table 2. Only the last heat treatment on a coil of the test mini-dipole, described in the next chapter, was done with a modified procedure in order to obtain a higher RRR (about 250 instead of 89) at the expenses of a moderate decrease of the critical current density (3% at 4.2 K and 12 T).

4.2. Calibrations and test of the experimental set-up

The temperature and its stability during the heat treatment to form the Nb_3Sn are important for the final superconducting and mechanical properties of the wire. The first part of the experimental work was then dedicated to the characterization of the furnaces where the superconductor is formed.

All the samples have been treated in the furnace shown in Figure 3, which has a very good stability up to 700ºC (temperature oscillations smaller than 1ºC at about 700ºC).

Figure 3. Furnace used to perform the pre-heat treatment.

The pre-reaction of the coils has been done with a low under pressure (about 100 mbar below the atmospheric one) to remove the large amount of the products of the burnt out of the binder.

To perform the final part of the heat treatment in argon atmosphere this furnace had to be adapted, as shown in Figure 4.

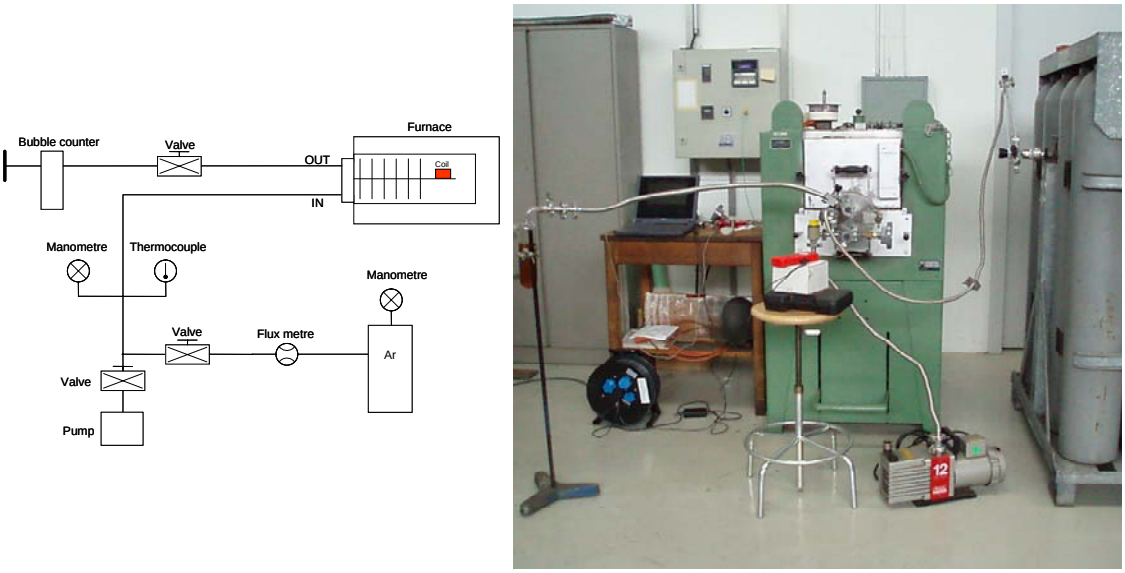

Figure 4. Experimental set-up for the last step of the heat treatment in argon atmosphere.

The sample, as shown in Figure 5, is placed over some pieces of alumina, which act as thermal shielding, and inserted in a metallic cylinder positioned inside the furnace and maintained in argon atmosphere.

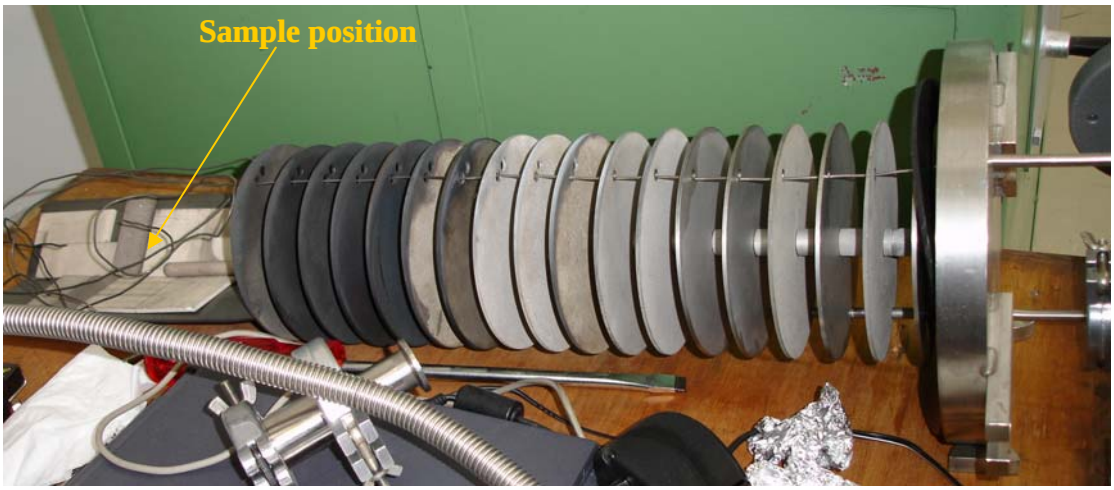

Figure 5. Structure inserted in the furnace to perform the final step of the heat treatment. The sample is put onto some pieces of alumina which act as thermal insulation.

A calibrated argon flux is used to maintain an overpressure of about 100 mbar inside the structure. The gas is poured into the furnace through a can which ends below the sample and evacuated through another can which discharges the gas in a bubble counter to produce argon circulation. At the beginning of the heat treatment the

interior of the furnace is cleaned from air by alternating an under pressure of about 900 mbar with an overpressure of about 200 mbar with respect to the atmospheric value for several times.

As a preliminary test the calibration of the thermocouples was necessary at temperature up to 700ºC. The procedure commonly adopted is to put a material with a precise melting point into the furnace, ramp the temperature and compare the output of the thermocouple with the temperature of fusion of the material. This technique couldn't be used, because the furnace able to reach temperature up to 700ºC hasn't any window to observe the melting of the material. An indirect method has therefore been adopted. A circuit, shown in Figure 6, has been made by some copper blocks and a copper wire, the thermocouple to be tested and a sample of CuAg (melting temperature of 779.2ºC). The achievement of the melting temperature of the CuAg has been detected indirectly by the opening of the circuit.

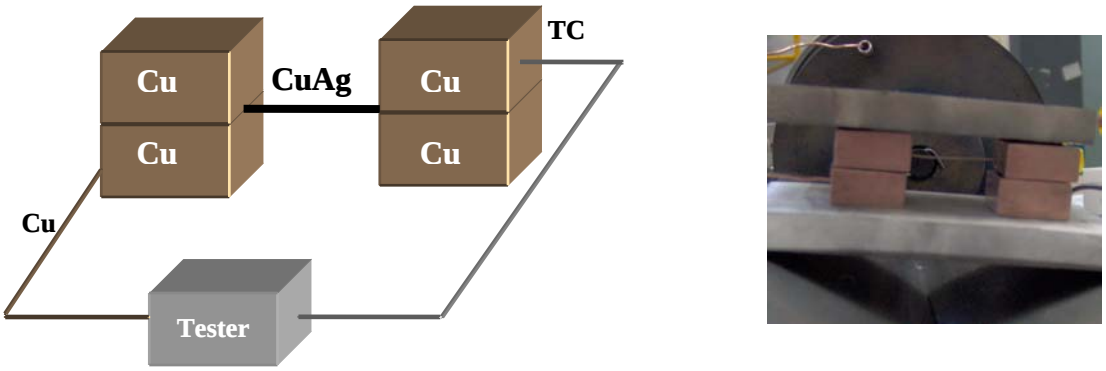

Figure 6. Scheme of the system used for the calibration of the thermocouples. A circuit is formed by a copper wire, a thermocouple (TC) and a CuAg wire. When the CuAg melts the circuit opens.

The temperature into the furnace has been ramped at 200ºC/h until 750ºC, and, after it became stable, it has been increased at 10ºC/h until the circuit opened. The detected temperature was 781.2ºC for the first thermocouple and 781.9ºC for the second one, which corresponds to a difference of 2.6 ‰ and 3.5 ‰ respectively with respect to the melting point of CuAg.

The second test was the determination of the gradient of temperature in the sample region along the radial dimension for the configuration of the reaction, which is the most critical condition because of the small dimension of the diameter of the cylinder where the argon atmosphere is maintained. The temperatures read by the two thermocouples put into the top and the bottom copper blocks at a distance of about

2 cm, which is smaller than the maximum dimension of the coils, has been measured. In Figure 7 the results are plotted.

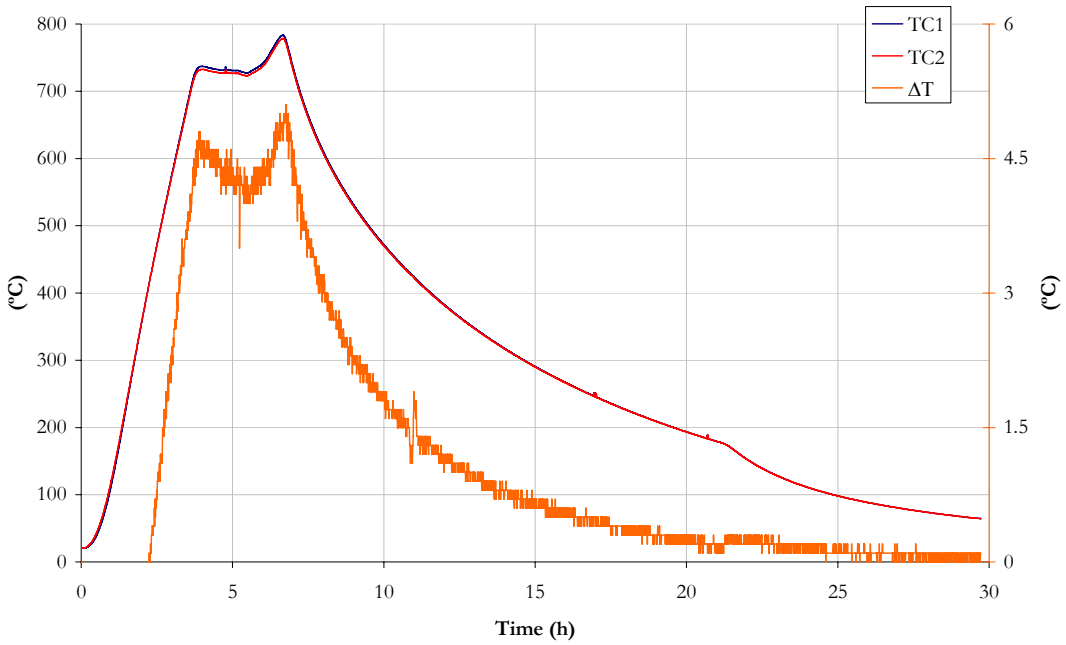

Figure 7. Temperatures read by the two thermocouples and their difference during the test to determine the radial gradient of temperature inside the furnace in the configuration for the reaction. On the left axis the temperatures read by the two thermocouples, on the right axis the gradient are indicated.

As it can be seen in the graph of Figure 7, the maximum gradient of temperature was 5.1ºC in correspondence of the ramp. This value decreases to 4.1ºC in the case of a plateau, which corresponds to less than 1% of the temperature.

4.3. Strand measurements

After the tests on the system described in the previous section, some samples have been heat treated and measured to characterize the conductor and at the same time to check the calibration of the experimental set-up. The RRR has been measured in the CERN test station. The critical current density could be measured in the existing facility CERN, and it was therefore necessary to design and manufacture a new sample holder.

4.3.1. RRR measurements

The resistivity of a material is determined by the scattering of the electrons, in motion under a difference of potential, by the atoms/molecules of the lattice and, in case of

metals, also with the electrons of conduction and with the imperfections/impurities of the material. The first contribution to the resistivity depends on the temperature of the material: the lower the temperature, the smaller the probability of scattering, and then the resistivity is. If the resistivity was determined only by this interaction it would go to 0 for temperatures close to the absolute zero. The scattering with the imperfections/impurities, always present even in the purest materials, gives a contribution to the resistivity which has a limiting value approaching to T = 0 K. The Residual Resistivity Ratio (RRR) is defined as the ratio of the resistivity at 293 K ($\rho_{293\,K}$) and the boiling point of helium at atmospheric pressure ($\rho_{4.2\,K}$):

$$RRR = \frac{\rho_{293\,K}}{\rho_{4.2\,K}} \tag{2}$$

The RRR is commonly used in metallurgy to quantify the presence of defects or impurity in the material.

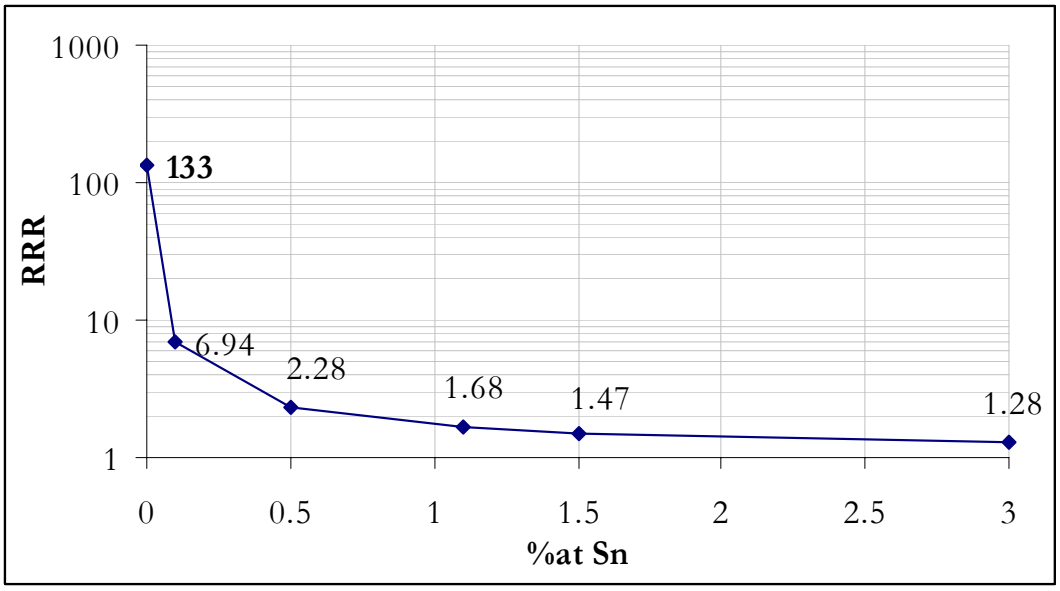

Figure 8. RRR of Cu-Sn alloys in function of the tin atomic percent.

In case of superconducting wires, RRR is normally used in quench computation, because the heat generation in the normal resistive zone depends on it. In particular for Nb_3Sn strands, RRR is used to investigate if the heat treatment caused the breakage of the barriers of protection and, consequently, the pollution of the copper stabilizer. This implies the increase of the resistivity, which may cause an overheating during a quench, and the decrease of the thermal conducibility which aggravates the flux jumping dynamic instability. Since the tin is a strong electron scatterer, the

pollution of the copper can be determined with a great accuracy. In Figure 8 the RRR[1] of Cu-Sn alloys for several atomic tin concentration measured by Fickett [5] is shown. As it is shown in the graph of Figure 8, a 0.1%at of tin is sufficient to reduce RRR from more than 100 to less than 10.

Since Nb_3Sn at 4.2 K and 0 T is superconductive, RRR is defined as the ratio of the resistivity at 293 K and at the critical temperature at zero field (T_C ~18 K).

The sample holder used to perform the measurement is shown in Figure 9.

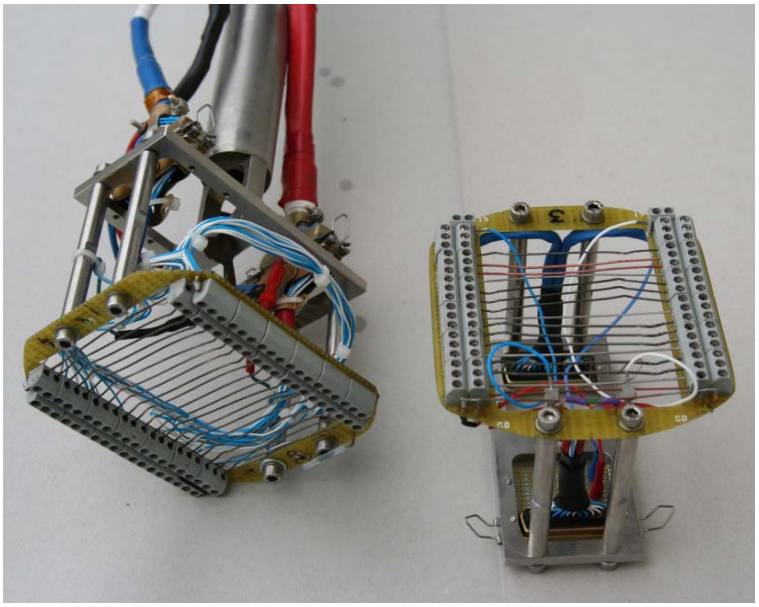

Figure 9. Sample holder for the RRR measurement. The total length of the sample is 11 cm. Courtesy of Zinur Charifoulline (AT/MAS-SC).

The strands to be measured are mounted with others used as references on the sample holder and immersed in a cryostat, where the temperature can be varied by two heaters.

The resistance is obtained by the fit of the voltage drops in function of the circulating current, as the one shown in Figure 10.

[1] For these data RRR has been taken as the ratio of the resistivity at 295 K and the one at 4 K.

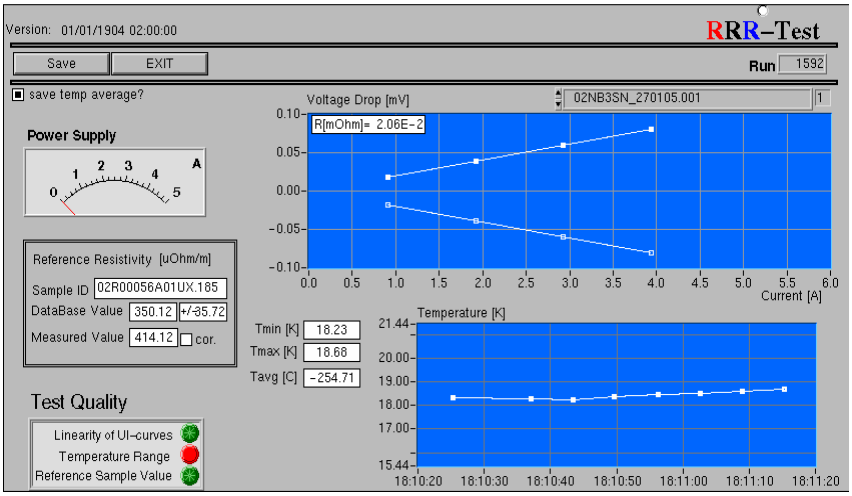

Figure 10. The straight line current-voltage drop used to determine the resistance of the sample. Also the temperature of the sample is monitored during the measurement. Courtesy of Zinur Charifoulline (AT/MAS-SC).

To determine the resistivity at the critical temperature the sample, initially at 4.2 K, is supplied by a constant current and the heaters are switched on to warm up the wire until a voltage drop is detected, indicating the transition of the superconducting to the normal resistive state. In Figure 11 an example of this step of the measurement is shown.

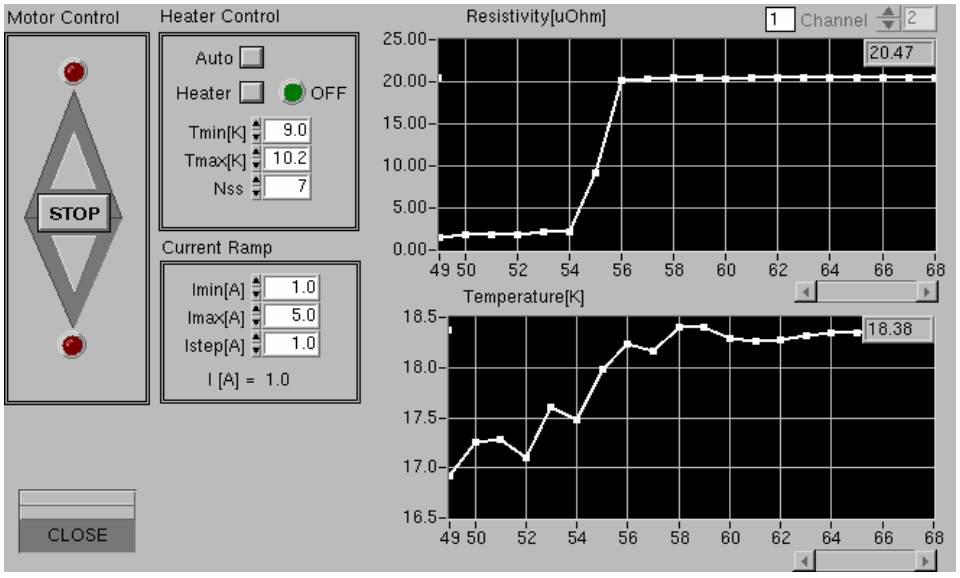

Figure 11. The resistivity and the temperature of the sample are plotted during the first step of the measurement at cold. Courtesy of Zinur Charifoulline (AT/MAS-SC).

The RRR measurement has been repeated for all the heat treatments (appositely done heat treatment, heat treatments for the measurements of the critical current density and for the test coils of the mini dipole). The average of the result of all these tests is RRR = 87±8, in agree with the value of 89 given by OI-ST indicated in Table 3.

Since the RRR of pure copper can be dramatically influenced by the long heat treatment performed to form the Nb_3Sn [6], an Oxygen Free Copper (OFC) wire has been put into the furnace and its RRR has been measured as reference. The results are shown in Figure 12.

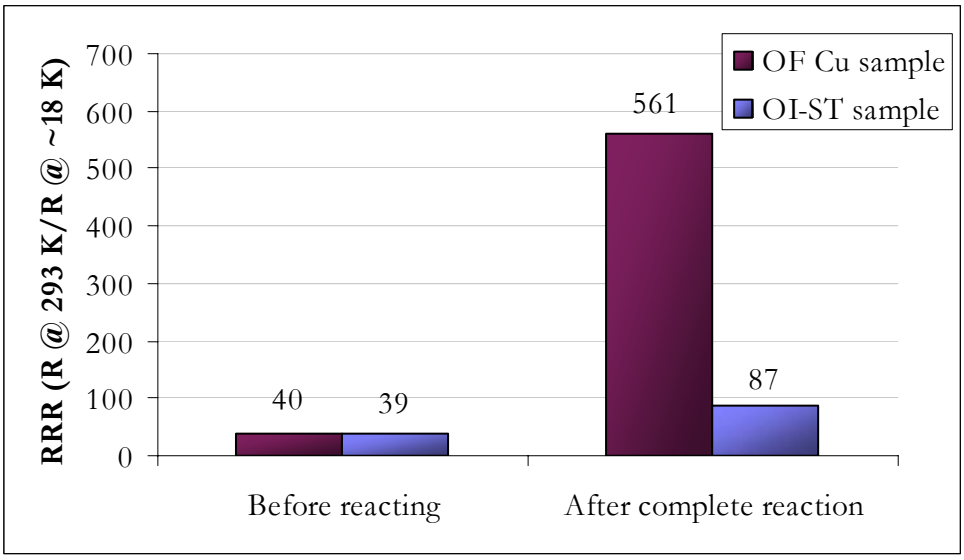

Figure 12. Measured RRR for the different steps of the heat treatment. The RRR of the copper is also indicated for comparison.

Before doing the heat treatment the two samples have the same RRR (39 for the future Nb_3Sn strand and 40 for the pure copper wire), whereas after the heat treatment the average Nb_3Sn RRR = 87 and the pure copper RRR = 561. Because of the presence of the bronze in the Nb_3Sn strand this result must not to be interpreted as the evidence of the pollution of the copper stabilizer. The value of RRR can only be used to compare heat treatments during which a similar quantity of bronze is formed, as the ones of Table 3, for which the same pre-reaction has been performed.

During these tests also the critical temperature has been determined. The average value is 18.1 K in accordance to the value found in literature and the fit presented in Section 4.1. .

4.3.2. Critical current measurements

The measure of the critical current I_C is performed at constant field ramping the current until the transition from the superconducting to the normal conducting state is detected by the appearance of a voltage drop across the sample. Several criteria are used to define I_C, but the most used are the resistivity and the electric field one. In the

first case I_C is defined as the current at which the resistivity is 10^{-14} Ωm. In the second one I_C is the current at which the electric field is 10 μV/m, as sketched in Figure 13.

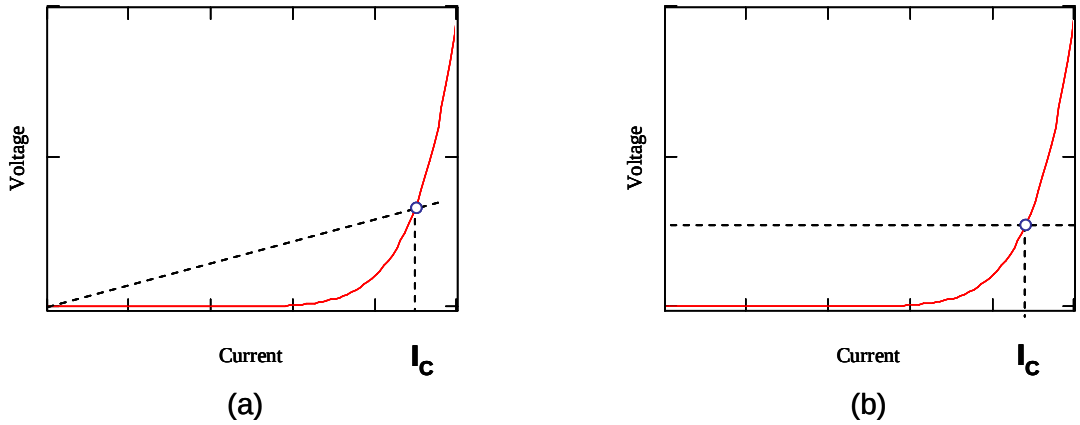

Figure 13. Resistivity and electric field criterion for the measurement of the critical current.
(a) Resistivity criterion: the critical current density is defined as the one at which the resistivity is equal to 10^{-14} Ωm. (b) Electric field criterion: the critical current density is defined as the one at which the electric field is 10 μV/m.

The electric field criterion has been selected in order to compare our measurement with the one of the manufacturer of the wire.

The scheme of the experimental set-up to perform the measurement is sketched in Figure 14.

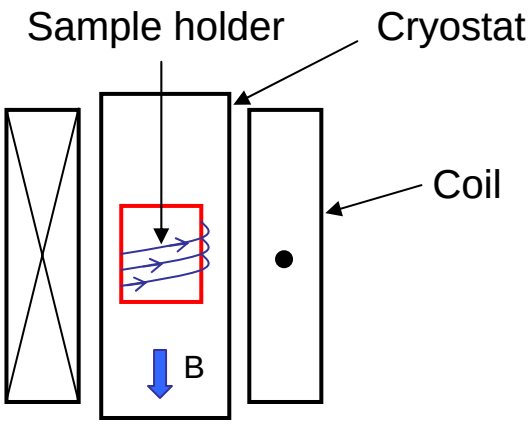

Figure 14. Scheme of the experimental set up for the measurement of the critical current density.

The sample is immersed in a 60 l helium cryostat, which permits to perform the measurement both at 1.9 K and at 4.2 K. An external solenoid produces a maximum magnetic field of 12 T with a good uniformity in the sample region along the mandrel axis (0.4% in a zone of ±5 cm from the center of the system) [7]. This is the station normally used to measure the NbTi strand at CERN. In Figure 15 the sample holder used at this station is shown.

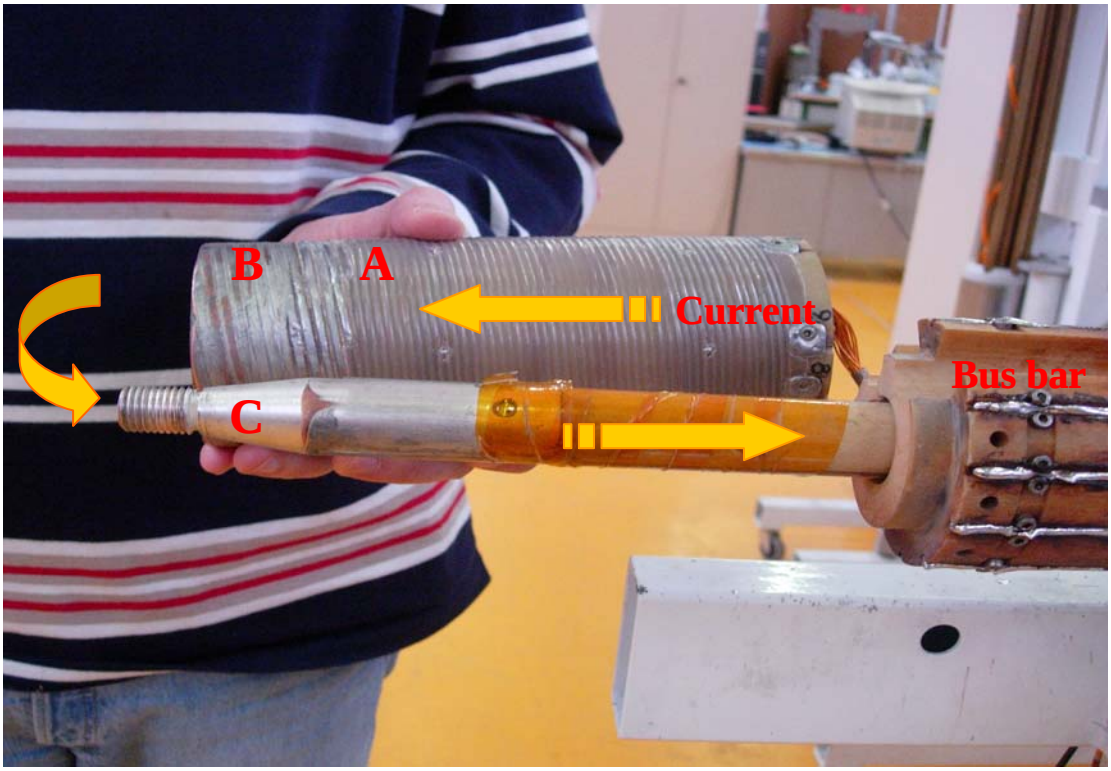

Figure 15. Sample holder for the critical current density measurement of the NbTi strands at CERN.

The current from the NbTi bus bars goes through the strand wound around the G11 block (A), as shown in Figure 16, to a copper cylinder (B) which is in electrical contact with the cone (C) to close the circuit.

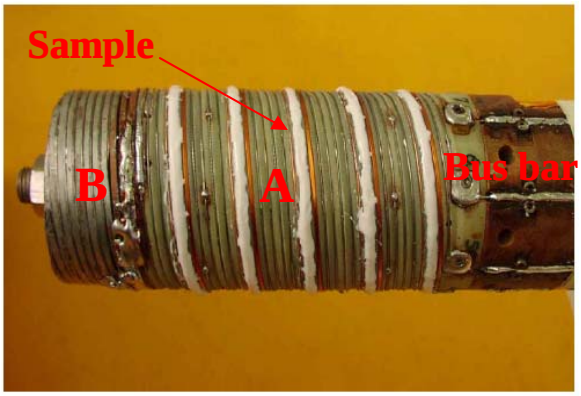

Figure 16. Strand wound on the sample holder for the measurement of the critical current density of the NbTi strands.

This sample holder was not suitable to perform the measurement of the Nb_3Sn strand, because neither the sample could be put on the block (A) after the heat treatment for the brittleness of the superconductor, nor the plastic G11 block can be put into the furnace at a temperatures up to 700ºC.

A new sample holder has then been designed and manufactured to perform the measurement of the Nb_3Sn strand (Figure 17).

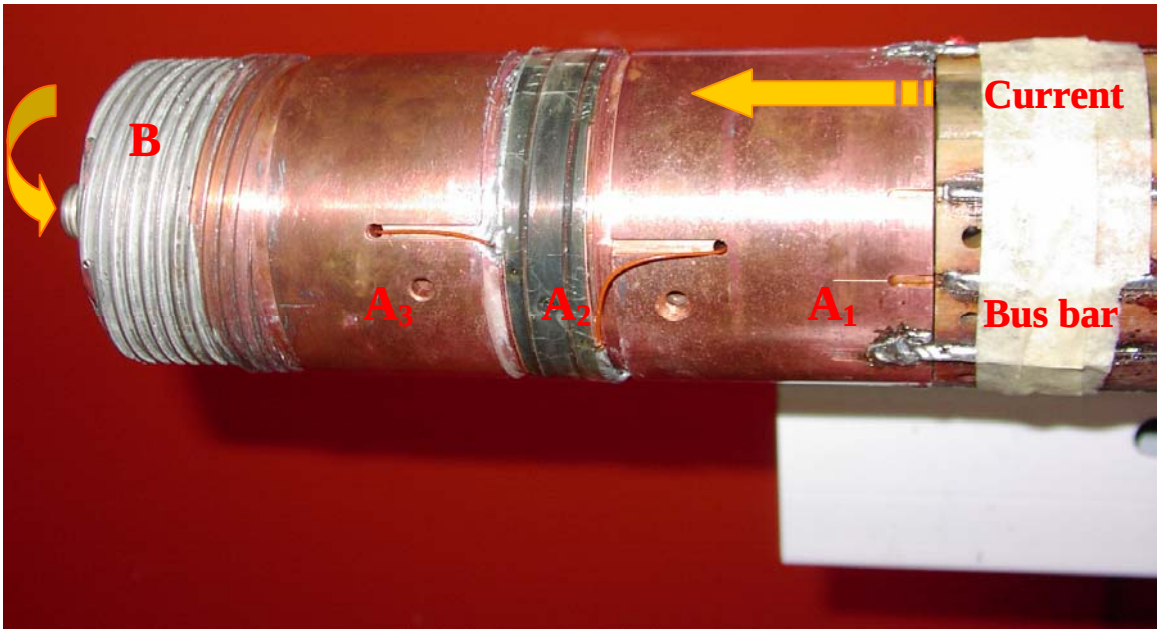

Figure 17. Sample holder used for the measurement of the Nb_3Sn strand. The original block A is replaced by the blocks A_1 (copper), A_2 (316 LN stainless steel) and A_3 (copper). Blocks A_1 and A_3 bring the current from the bus bar to the sample, wound on block A_2, and from the sample to the block B respectively.

The block (A) of Figure 15 has been replaced by two copper blocks, A_1 and A_3 and a 316 LN stainless steel one A_2. The sample to be tested is wound on the block A_2 to which the current is brought by the block A_1. The current is brought away by the A_3, which is electrically in contact with the rest of the structure used to perform the measurement on the NbTi strand.

The sample is wound onto the block A_2, which resists to the high temperatures necessary to form the Nb_3Sn. This sample holder has also the advantage to reduce the necessary quantity of strand of a factor 3 with respect to the one necessary for NbTi sample holder.

After the heat treatment, the sample is impregnated onto block A_2 to prevent any movement that may produce a quench when the sample is supplied.

For the first test the strand has been impregnated by araldite AY 103, a resin with good mechanical and insulation characteristics easy to use, because it requires a relatively low temperature to solidify. The strand on the block A_2 has been maintained at a temperature of about 50ºC for 2 hours rotating under an infrared lamp, thereafter

put in a furnace at 110ºC for 4 hours. After this process the block A_2 is soldered to the A_1 and A_3.

The measurement has been performed at 1.9 K to prevent the quench of the NbTi bus bar, which, in the case of the measurement at 11 T, would have been in a magnetic field of 10.96 T. The fit presented in the Section 4.1. has been used to rescale the expected value from the OI-ST for a measurement at this temperature. The maximum current and magnetic field allow exploring the zone in the plane B-I shown in Figure 18. In this plot the critical current obtained by the fit of the measured values given by OI-ST at 4.2 K and the same curve rescaled for a temperature of 1.9 K are shown.

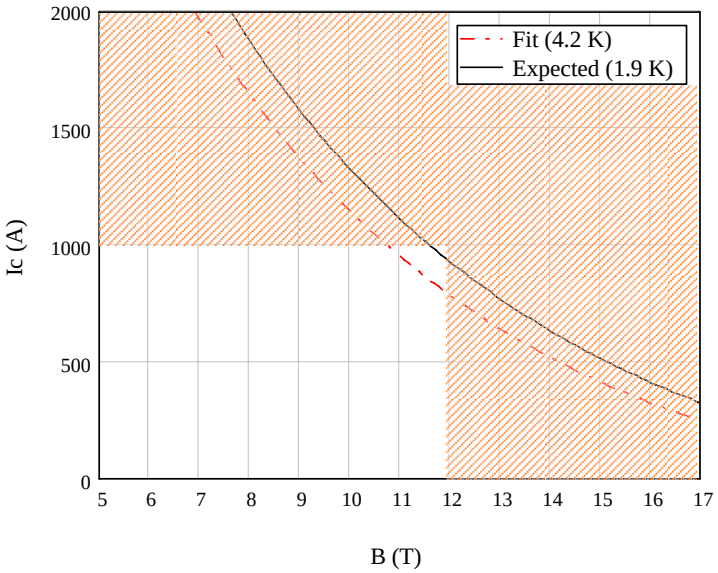

Figure 18. Exploitable region of the plane B-I. The power supply is limited to 1000 A and the maximum magnetic field is 12 T.

In Table 5 the measured quench current and the maximum one, indicated in bold, for the several values of the magnetic field are shown.

Quench	1	2	3	4	5	6	7	8	9	10	**11**	**12**	13	14	**15**	**16**
B (T)	11	11	11	11	11	11	10	10	10	10	**10**	**9**	11	11	**7**	**11**
Ie (A)	1109						1323					**1574**	1109		**2230**	**1109**
Iq (A)	477	582	592	665	678	664	654	635	660	642	**670**	**714**	669	680	**784**	**680**

Table 5. Quench current measured, Iq, and expected, Ie, at several magnetic fields.

A comparison between the measurement and the expected values is shown in Figure 19.

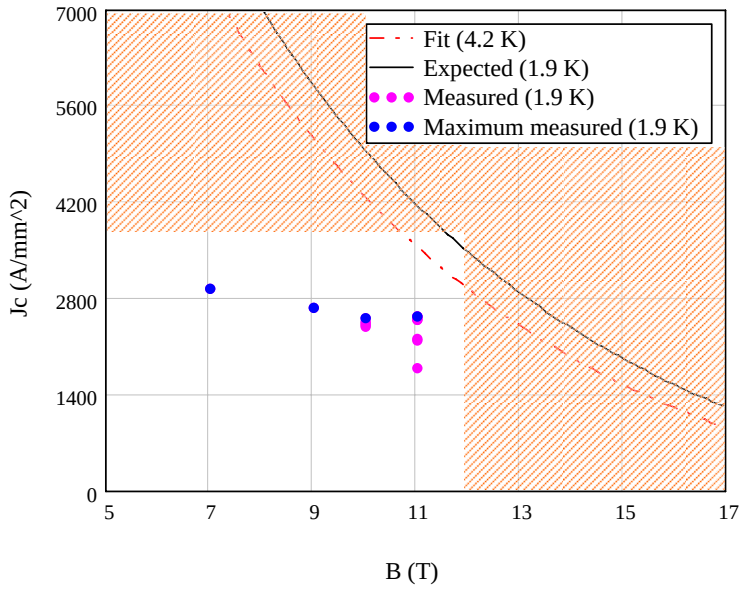

Figure 19. Measured critical current density in the first test. The fit from the OST data points measured at 4.2 K and the values rescaled for the temperature at which our test has been performed are also indicated.

The discrepancy between the expected and the measured I_C is due to the resin. This hypothesis has been confirmed when the sample holder has been removed from the cryostat and some cracks were clearly visible in the resin, as shown in Figure 20.

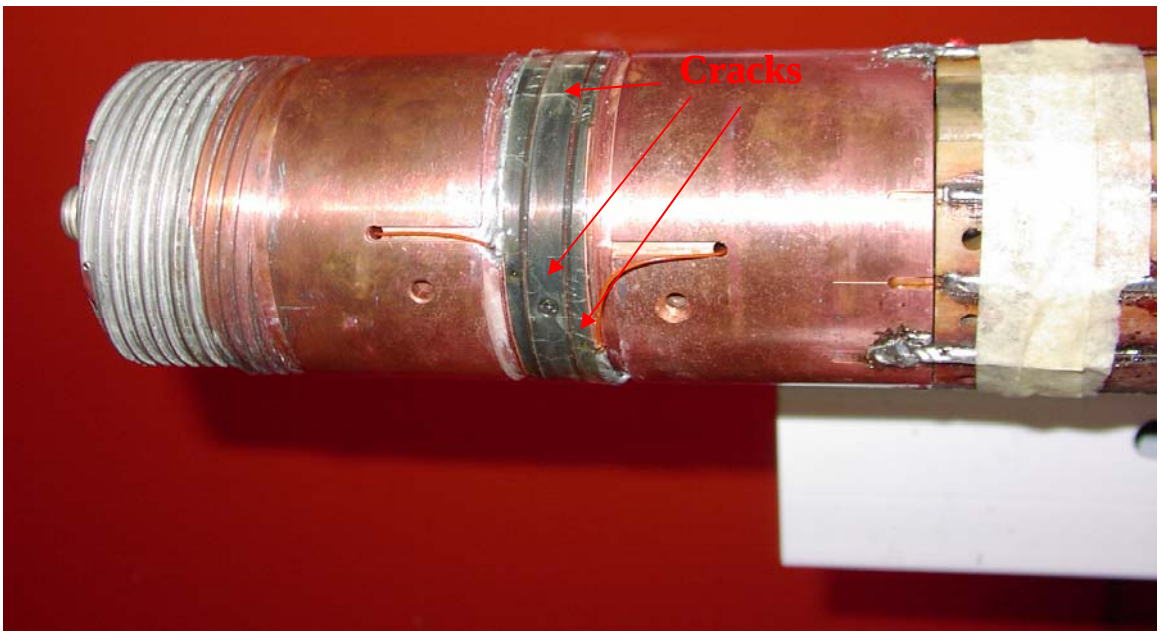

Figure 20. Sample holder after the first test. The cracks in the resin are visible.

A second test has then been done impregnating the sample with Stycast®, which is more resistant to the thermal shocks than the AY103. This resin, due to its relative

high viscosity, is not suited for coils impregnation, but it can be used to impregnate one turn strand, as in our case.

This test was successful, as shown in Figure 21.

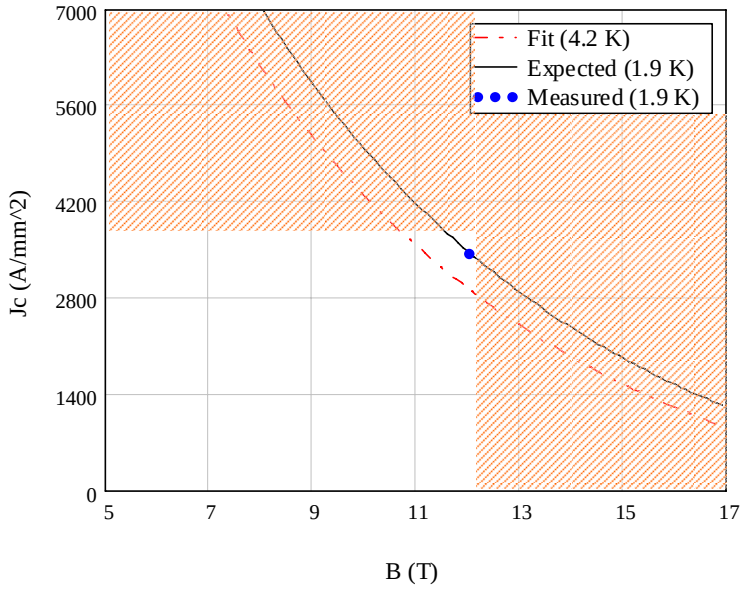

Figure 21. Measured critical current density in the second test. The fit from the OST data points measured at 4.2 K and the values rescaled for the temperature at which our test has been performed are also indicated.

In Figure 22 the sample holder after the measurement is shown.

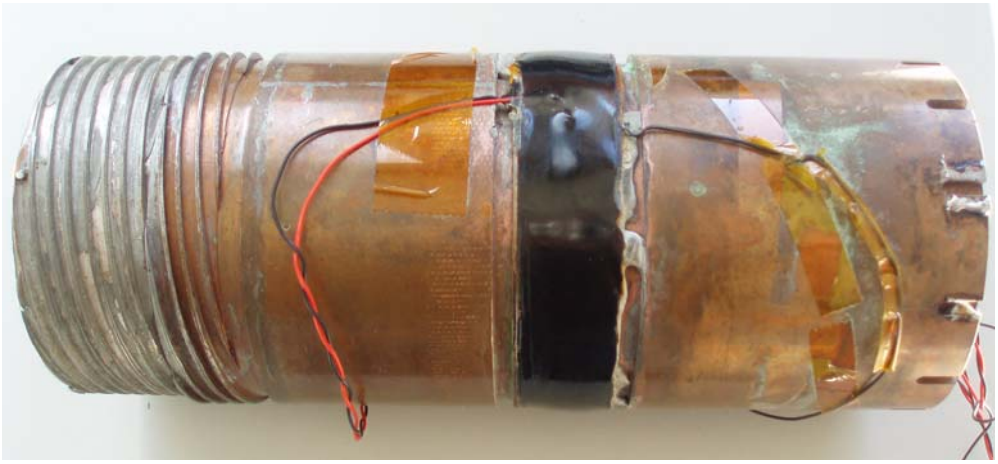

Figure 22. Sample holder after the second test.

In this case no cracks have been observed.

The successful RRR and critical current measurements allowed to verify that the experimental set-up to perform the heat treatment is correct and to confirm the strand performances given by OI-ST.

4.3.3. Flux jumping instability measurements

As described in the previous chapter, flux jumping instability is a problem which may affect high critical current density superconductors. This phenomenon becomes more important for strands with large filaments, as IT wires, which have the largest filament dimensions (the wire for the LHC undulator have filaments with dimensions of ~90 μm). In the last years the strand design maximized the non-copper over copper ratio, increasing the number of the Nb filaments and the content of the tin pools, reducing the inter-filaments distance to improve the critical current density. A too aggressive heat treatment to obtain the highest critical current density by maximizing the quantity of superconductor, may cause the coalescence of the filaments, which behave like larger ones. In this case the strand could suffer both of adiabatic and dynamic instability for flux jumping.

A standard method to detect the region of instability, proposed by Wilson and Walters [8], is to maintain a constant current in the sample and sweep the magnetic field until a transition to the normal resistive state is produced.

Due to a limitation of the batteries used for the critical current density, this kind of measurement couldn't be performed at CERN. Two samples have been tested at LASA (INFN Lab) in the super compact magnet station, which allows achieving a magnetic field of 13.5 T and a current of 2000 A.

The sample holder used to perform the measurements is the standard VAMAS, shown in Figure 23.

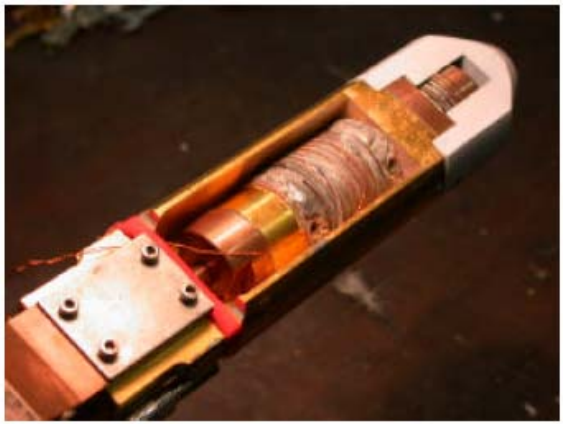

Figure 23. Sample of Nb_3Sn wound on the sample holder VAMAS used at LASA to perform the measurements [9].

Before performing stability measurements, critical current density tests have been done, exploiting the fact that the instrumentation at LASA allows exploring a larger region in the plane B-I than the CERN station can.

The results of the measurement for the two samples are shown in Table 6.

Sample 1			Sample 2		
B (T)	I_C (A)	n	B (T)	I_C (A)	n
13.5	570.4	55	13.5	563.0	48
13.0	629.7	57	13.0	625.9	59
12.0	762.3	62	12.0	757.3	63
11.0	913.1	69	11.0	905.8	67
10.0	1085.4	72	10.5	990.6	83
9.0	1285.1	70			

Table 6. Results of the critical current measurement for the two samples measured at LASA using the voltage criterion and at operating temperature of 4.25 K.

In Figure 24 the corresponding critical current densities are plotted.

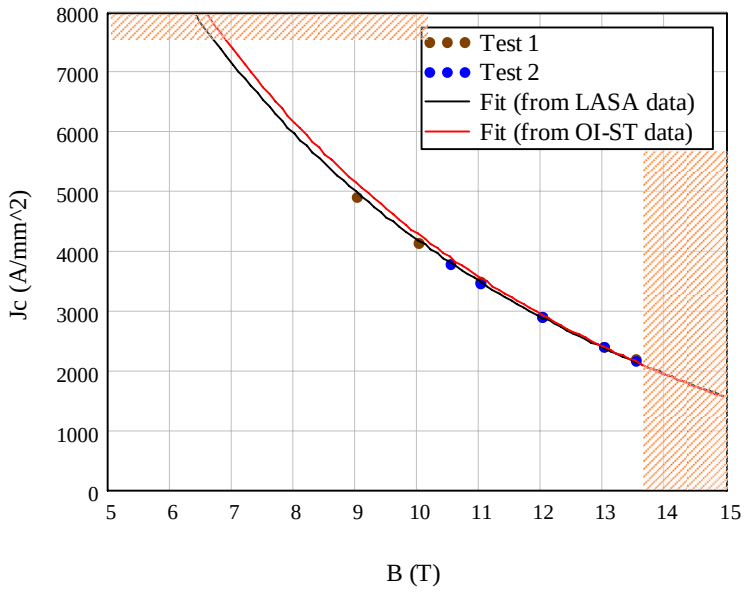

Figure 24. Fit of the critical current density from the measurements performed at LASA. The testable zone of the plane is also indicated.

As shown in Figure 24, the results obtained from the two samples at LASA are in perfect agreement. All these data have been used to perform a unique fit of the critical current density, using eq. (1). This new fit allows to describe the curve field-critical current in the region of smaller fields, closer to the values of the design of the LHC

undulator than the OI-ST data. The values of the parameters are $B_{c20} = 26.9\,T$, $T_{c0} = 17.8\,K$ and $C_0 = 40360\ AT^{1/2}/mm^2$.

As reported in literature, [10], [11], [12], [13], [14], [15], the ramp rate of the magnetic field used for this kind of measurement is between 1 mT/s and 15 mT/s. For the tests described in this chapter it has then decided to ramp the field at 5 mT/s.

In Table 7 the maximum magnetic field reached without a quench (B_{MAX}) and the magnetic field of a quench (B_{QUENCH}) are summarized.

I (A)	B_{MAX} (T)	B_{QUENCH} (T)
200	13.5	
590	13.5	
660		13.0
790	0.0-6.3	12.0
	10.0-11.7	
	11.5-	

Table 7. Stability measurement results. B_{MAX} is the maximum magnetic field achieved without a quench and B_{QUENCH} is the magnetic field where a quench has been detected. All these measurements have been performed ramping the magnetic field at 5 mT/s.

At these currents no instability has been detected, because the strands quenched at values of magnetic field-current corresponding to the critical curve or they did not quench at all in the range of the magnetic field exploitable by the station.

The measurement at 790 A had to be stopped several times before reaching the field of the transition to recharge the batteries, then to perform the measurements at higher currents it has been decided to increase the ramp rate of the field from 5 mT/s to 14 mT/s. In Table 8 the results are indicated.

I (A)	B_{QUENCH} (T)
600	13.5
900	2.3,2.1
1000	0.9,1.7,1.6

Table 8. Stability measurement results. B_{QUENCH} is the magnetic field where a quench occurs. All these measurements have been performed at a magnetic field ramp rate of 14 mT/s.

The strand showed instability for current of 900 A and 1000 A, for which quenches, expected to appear at fields higher than 10 T, have been detected at about 2 T and 1 T

respectively. As a cross check it has been verified that the measurement at 1000 A, with a ramp of 5 mT/s, gave the same result at 14 mT/s.

The results of all these measurements are plotted in the graph of Figure 25.

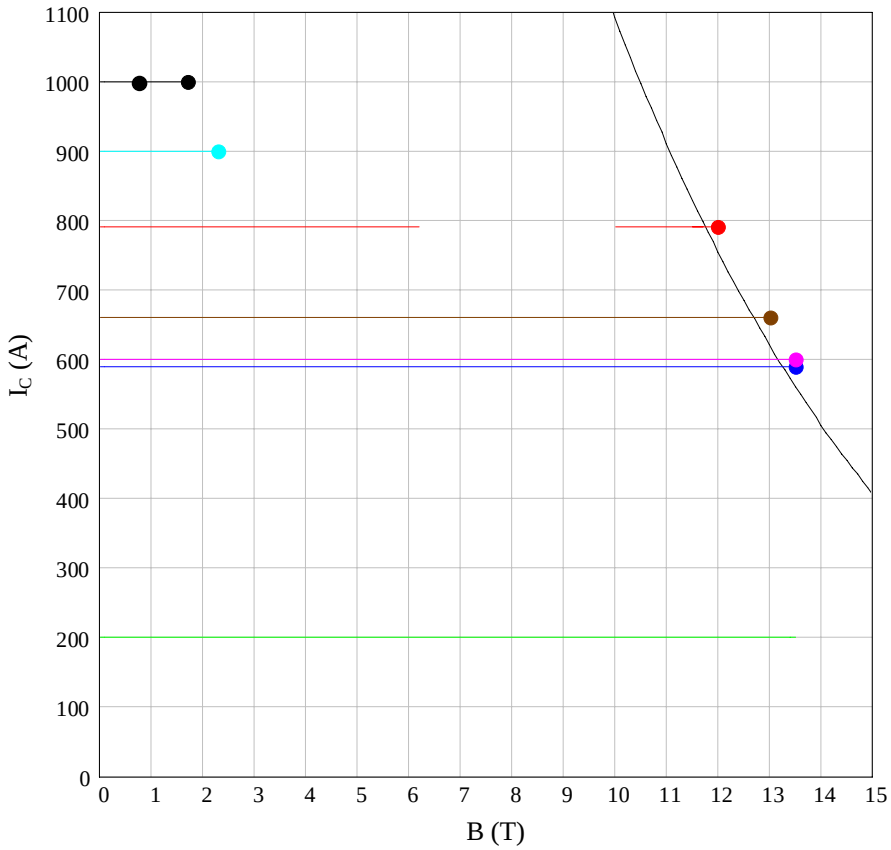

Figure 25. Results of the stability measurements on the two samples. If a quench occurs a point is indicated, whereas the lines which end without a point correspond to a measurement stopped to recharge the battery (case I = 800 A) or for the achievement of the maximum field that the station can produce (case I = 200 A).

The load lines of the undulator coils for the short and the long period configuration are plotted in Figure 26.

For each value of current, during the ramping and at the working point, the conductor points of the coils are immersed in a magnetic field between 0 T and the field on the load line. According to these results, only the coils of the long period configuration can be manufactured using the OI-ST wire, heat treated with the procedure of Table 2. The zone of the plane magnetic field-current for the coils of the short period configuration, in fact, contains a region of flux jumping instability, at current higher than 900 A.

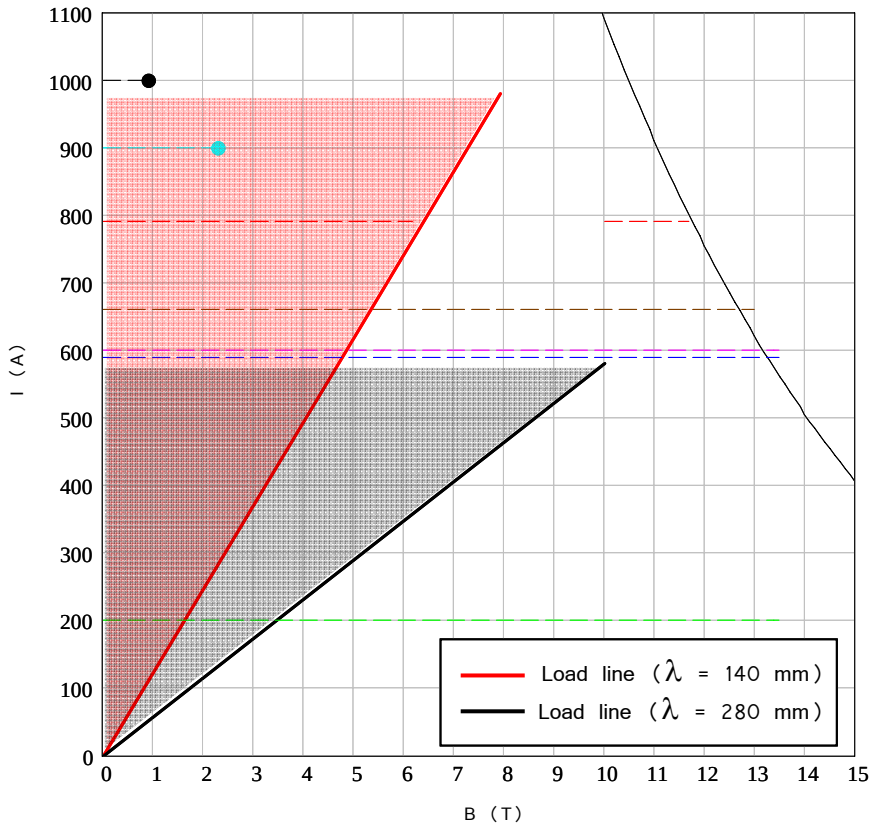

Figure 26. Load lines of the coils for the short and the long period configuration of the undulator. During the ramping of currents the conductor of the coil is subject to a magnetic field from 0 T to the field of the load line.

Two possible solutions can be considered. The first one is to heat treat the wire using a new procedure to improve the flux jumping stability. The second one is to make a new design of the undulator requiring a lower current in coil of the short period configuration. Both possibilities have been explored.

OI-ST proposed a new heat treatment which, according to its measurements, may give a more stable strand for flux jumping (RRR of 250 with respect to the 89). This heat treatment has been used directly to test a coil of the mini-dipole and it is presented in chapter 5.

4.4. Alternative design

To produce the same magnetic field lowering the current in the coils of the short period configuration it is necessary to increase its dimensions to have the same number of ampere-turns. Since the horizontal dimension of the coil is fixed by the

minimum radius of curvature of the strand, the only possibility is to increase the number of turns.

The height of the coils of the short period configuration has been determined to obtain the requested 3 T in the mid-plane imposing a maximum current of 800 A. Because of this modification, the coils of the long period configuration have to be placed far away from the mid-plane, becoming less efficient. An increase of only 20 A with respect to 580 A of the design presented in chapter 2 is enough to produce the requested magnetic field reducing in a negligible way the margin to quench.

The specifications of the modified design of both the configurations of the undulator are summarized in Table 9.

	λ = 140 mm	λ = 280 mm
Gap (mm)	60	
Number of periods	2	
Current (A)	800	600
B_0 1 (T)	3.10	5.05
B_0 2 (T)	2.98	4.75
Margin to quench (%)	23.7	16.8
Number of layers	24	61
Number of turns	13	13
Length of the cable for 8 coils (km)	1.02	3.42
Total length of the cable for both the configurations (km)	4.44	

Table 9. Specifications of the design of both the periods of the undulator modified after the flux jumping instability measurements.

The load lines of the coils of the short and the long period configuration according to this new design are shown in Figure 27.

According to this alternative design the coils of the undulator shouldn't suffer of flux jumping instability and they could be manufactured using the OI-ST wire heat treated according the schedule of Table 2.

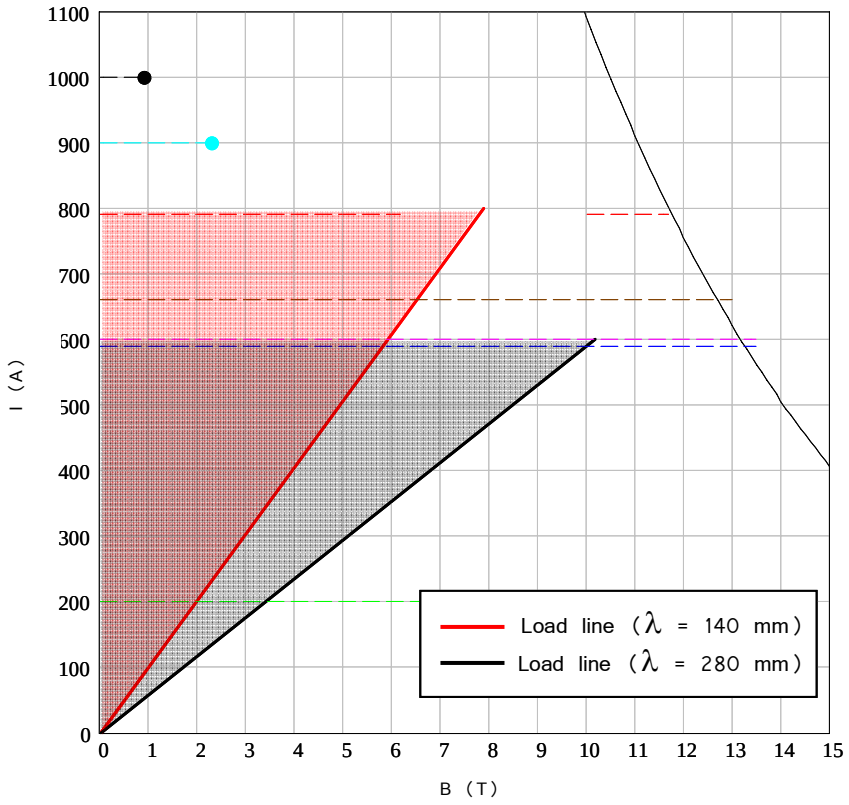

Figure 27. Load lines of the short and long period configurations of the coils of the undulator made after the flux jumping instability measurements.

4.5. Conclusions

In this chapter the setting-up to perform the heat treatment to form the Nb_3Sn has been described. To verify the correct calibration the results of RRR and critical current measurements have been compared with the strand specifications given by the manufacturer of the wire. After these tests were successful a flux jumping instability test has been done to verify if a region of instability is present in the plane magnetic-field current for this strand. This measurement evidenced a region of instability which excludes the feasibility of the coils of the short period of the undulator according to the design presented in chapter 2. An alternative design of the undulator has been then carried out in case the heat treatment will not improved to eliminate the region of instability.

CHAPTER 5

DESIGN, MANUFACTURE AND TESTS OF Nb_3Sn MINI-DIPOLE SPLIT COILS: RESULTS AND ANALYSIS

To verify the feasibility of coils using the OI-ST wire, a test mini-dipole has been designed and manufactured in several units. The magnet is made by two Nb_3Sn solenoids inserted into two NbTi ones. This design has been optimized to reproduce the operational conditions of the coils of the undulator (similar magnetic field on the conductor, current and radius of curvature) and to test the connections, using a reasonably small amount of wire. Two tests have been performed. In the first one numerous quenches have been observed. The possible explanation has been identified into the heat treatment to form the superconductor (too aggressive one and/or disuniformity of the temperature during it). To verify these hypotheses a second test has been performed. A coil has been heat treated in another furnace, according to the same scheduling used for the coil of the first test. In parallel another winding has been heat treated in the same furnace of the first test, but using a thermal shielding to improve the uniformity of the temperature in the region of the coil and performing a different heat treatment, which, according to the OI-ST measurements, should give a more stable strand. During this test no mechanical or flux jumping instabilities have been detected, but the quenching current was limited by the heating of a point, very possibly located at the connection.

These tests allowed verifying the feasibility of the coils of the undulator, but the limitation on the current didn’t allow demonstrating definitively their feasibility according to the design presented in chapter 2 and chapter 4.

In case future tests will show any instability in the region of the plane magnetic field-current not explored during these measurements, an alternative design has been studied.

5.1. Magnetic design

The mini-dipole has been conceived to reproduce the operative conditions of the coils of the undulator in order to verify the feasibility of these magnets using the OI-ST wire. To minimize the amount of wire necessary to manufacture the coils, it has been decided to make solenoids, also in consideration of the fact that it is not necessary to produce the good field region for this kind of tests. To further reduce the amount of wire the gap has been chosen as small as possible compatibly with the 2 mm necessary to put a Hall probe to measure the magnetic field. In Figure 1 the 2D model made by Poisson in cylindrical symmetry around the vertical axis is shown.

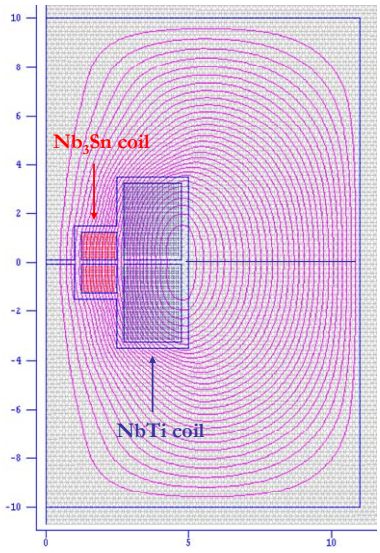

Figure 1. 2D simulation of the mini-dipole split coil with Poisson code. The dipole has a cylindrical symmetry with respect to the vertical axis. Dimensions are in cm.

The two Nb_3Sn solenoids are surrounded by two NbTi coils, used to enlarge the explored region of the plane magnetic field-current producing a background field on the Nb_3Sn.

The specifications of the Nb_3Sn strand have been reported in chapter 3. The specifications of the NbTi wire, already used to manufacture the first LHC undulator, are indicated in Table 1.

Bare strand size (mm x mm)	1.53 x 0.67
Insulated strand size (mm x mm)	1.65 x 0.97
Cu/SC ratio	1.63

Table 1. Specifications of the NbTi strand used to manufacture the external coils of the mini-dipole.

Numerous configurations can be optimized to have, for example, the maximum current in the Nb_3Sn coil or to generate the maximum field on the OI-ST wire. The configuration presented in Table 2 is the one which allows producing the maximum magnetic field in the mid-plane of the mini-dipole compatibly with a reasonable margin to quench in all the coils.

	Nb_3Sn coil	**NbTi coil**
R_{INT} (cm)	1.25	2.75
R_{EXT} (cm)	2.50	4.75
Coil height (cm)	1.24	3.15
Margin to quench (%)	14.8	57.75
Strand length (m)	21.2	98.9
Current (A)	600	300
Gap (mm)	2	
Maximum field in the mid-plane (T)	11.8	
Maximum field on the conductor (T)	10.3	
Operating temperature	4.2	

Table 2. Specifications of the mini dipole.

The manufacturing process and the system of measurement are described in the next section together with the setting-up used to perform the tests.

5.2. Manufacture of the coils

The Nb_3Sn coils have been wound using the automatic machine shown in Figure 2 [1], onto a 316LN stainless steel mandrel covered by a S2 fiber glass glove used as ground insulation.

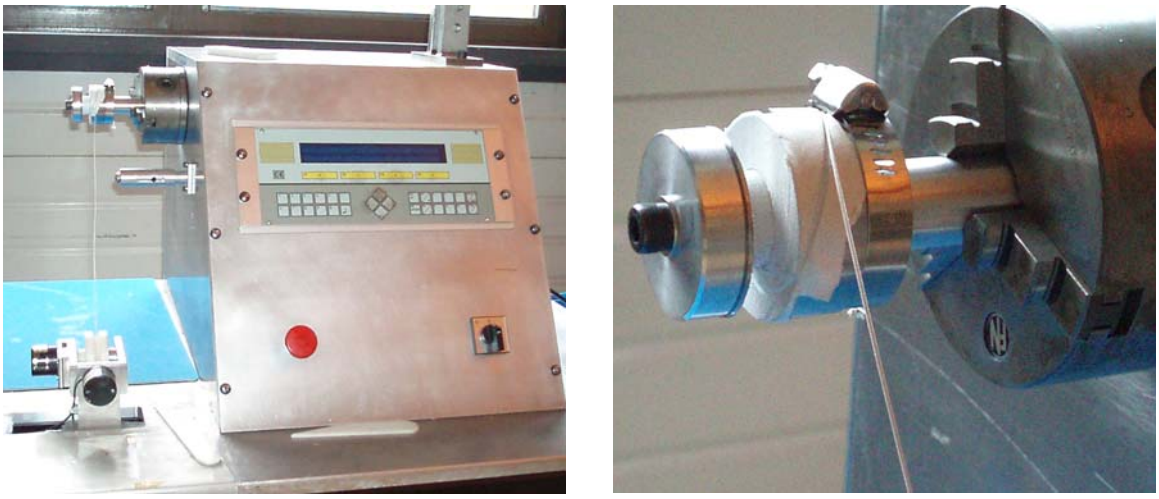

Figure 2. Winding of the coil. The winding machine and the close view of the coil are shown.

After the winding, the coil has been impregnated with the resin CTD-101. This has been chosen (instead of the Stycast®), for its good resistance to the thermal shocks and its low viscosity, which makes it particularly adapted for impregnations, because able to well penetrate in the space between the windings [2]. The CTD-101 and the hardener have been dried at 80ºC for 2 hours before being mixed with a catalyst. The coil is impregnated in vacuum maintained at the same temperature. The polymerization is performed at 110ºC for 5 hours followed by a post-curing at 125ºC for 16 hours.

To bring the current to the Nb_3Sn coil a NbTi strand has been soldered to the OI-ST wire in the point corresponding to the lowest field on the Nb_3Sn coil structure during the test. The two wires are overlapped for about 3 cm, which corresponds to two complete twist pitches of the Nb_3Sn wire. The coil after this step appears as shown in Figure 3.

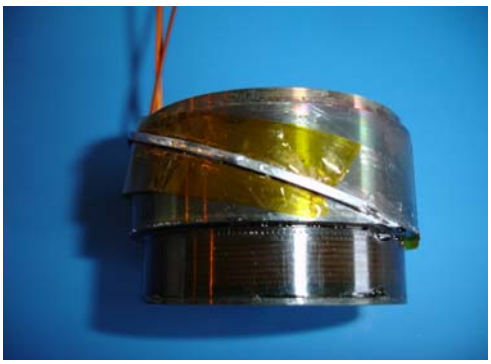

Figure 3. NbTi strand soldered to the Nb_3Sn strand to bring the current to the coil.

The NbTi coil has been manufactured with the same procedure of the coils of the NbTi undulator [1]. It has been wet wound by the AY 103. After a first curing at 100ºC the coil has been fitted in a mold and coated under pressure with Stycast®. This final configuration of the NbTi coil is shown in Figure 4.

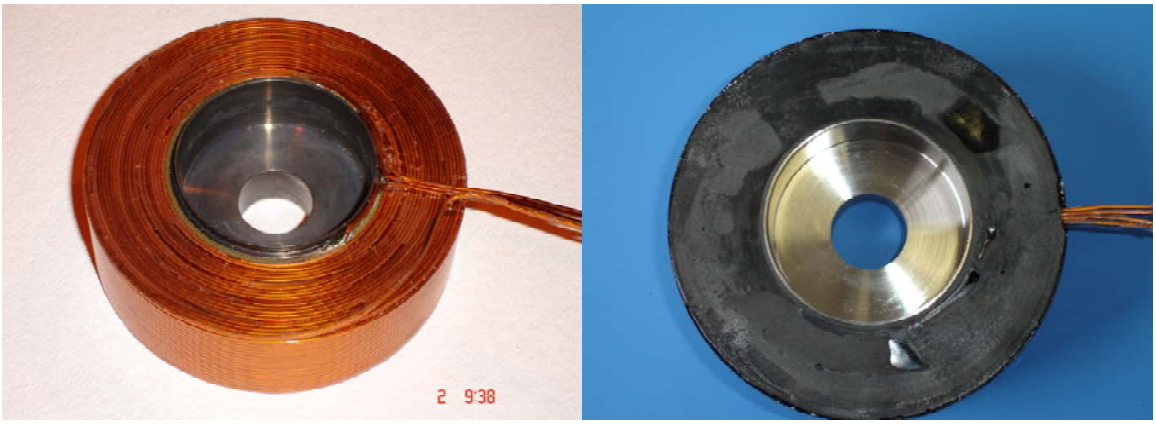

Figure 4. NbTi coil after the winding/impregnation.

The Nb_3Sn coil has been inserted inside the NbTi coil, and the two coils inside the iron yoke. This has been used both to close the flux lines and to mechanically retain the NbTi coil. At this phase of the assembly the magnet appears as shown in Figure 5.

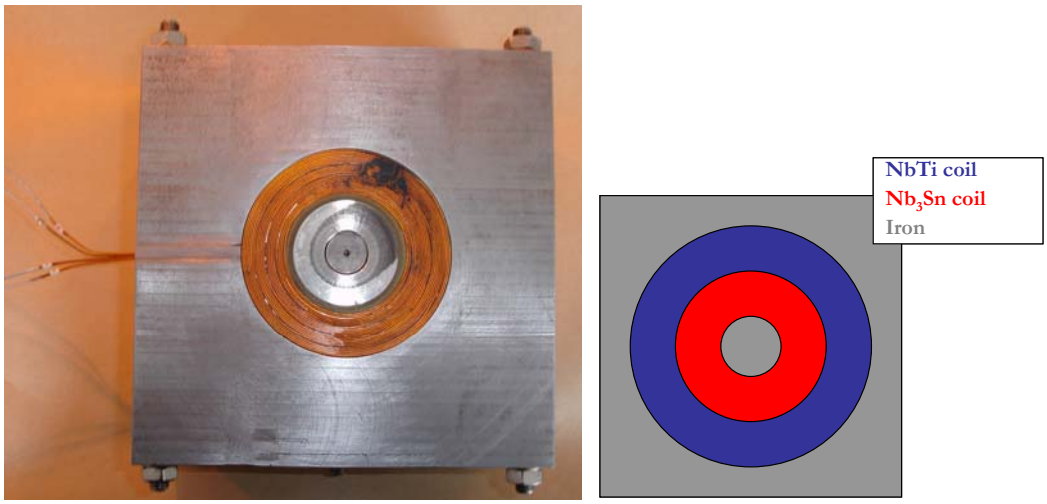

Figure 5. Half configuration of the mini-dipole spit coil. The two coils are inserted one into the other one and inside the iron yoke.

To facilitate the cooling of the magnet two glass fiber sheets in a configuration of fish-bone have been inserted between the coils and the yoke, as shown in Figure 6.

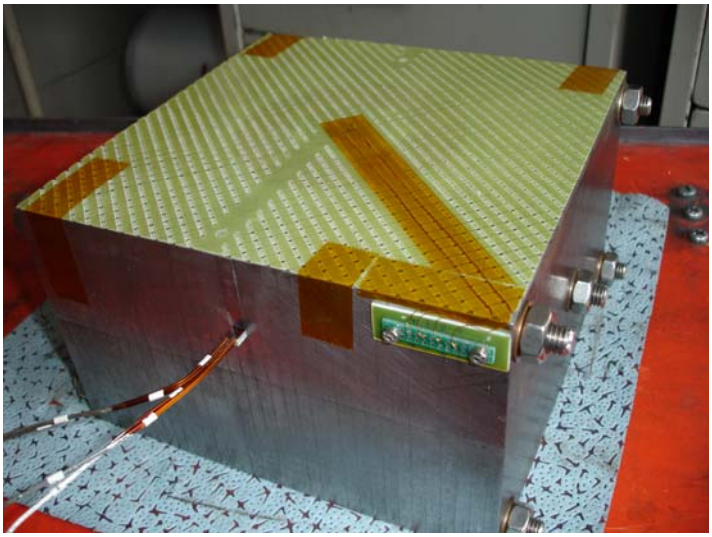

Figure 6. Glass fiber sheets to improve the cooling. The NbTi strands to bring the current to the coils and the terminals of the Hall probe are visible.

This assembly procedure should have been repeated for the second half of the mini-dipole to make the complete configuration shown in Figure 1. However the two tests have been performed immediately after the completion of the heat treatment of the Nb_3Sn coils, using only two coils.

The first test has been performed using the first Nb_3Sn and first NbTi coil. In this case the yoke of the second half of the mini-dipole has been put over the structure of Figure 6, as shown in Figure 7.

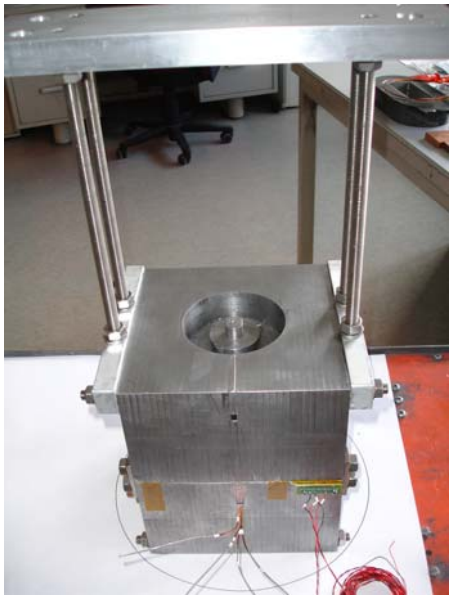

Figure 7. Final structure for the first test. The coils are inserted in the bottom block and the yoke made for the second half of the mini-dipole is used as a top block.

The second test has been performed using the two coils in Nb_3Sn. In this case a ring of brass has been used to fill the space foreseen for the NbTi coils, as shown in Figure 8.

Figure 8. The structure of the magnet for the second test. The space of the NbTi coils has been filled by a brass ring.

The picture of the complete structure as inserted into the cryostat is shown in Figure 9.

Figure 9. Complete assembly of the magnet as inserted in the cryostat.

In the next sections the measurement system and the obtained results in the two configurations are described.

5.3. Quench detection and acquisition system

In a typical test of superconducting magnets the coil is supplied by an increasing current until the difference of potential measured along the conductor exceeds a threshold value, indicating the starting of a quench.

The total tension of the coil, V_T, is given by:

$$V_T = V_L + V_M + V_R = L\dot{I} + M\dot{I}_C + R_Q I \qquad (1)$$

where V_L, V_M and V_R are the self, the mutual and the resistive tension respectively, L and M the self and the mutual inductance, R_Q the resistance which is developed in case of quench, I_C is the current of the coupled coil and the points indicate for the time derivative. If the current is supplied at a constant ramp rate the inductive tensions are constant, except for the dependence of L and M on the saturation of the yoke, and, if no quenches develop, the resistive part of the tension is zero. When a quench starts the resistive tension starts to grow up and, if it exceeds the threshold value, the power supply is switched off and the circuit is closed into a resistance to dissipate part of the stored energy.

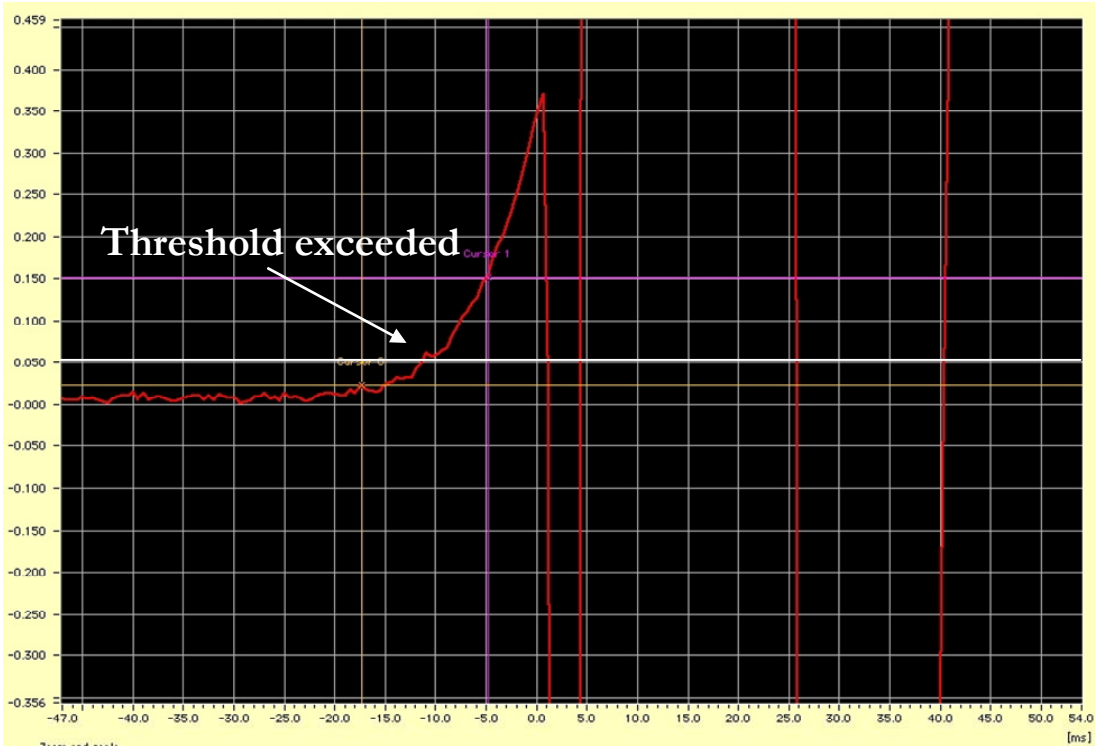

Figure 10. Detection of a quench. If the threshold is overcome for more than 10 ms the power supply is switched off and the quench is recorded.

The acquisition system considers as threshold tension the measured V_T subtracting the inductive tension:

$$V_A = V_T - V_{Inductive} \quad (2)$$

A quench recorded by Labview acquisition system is shown in Figure 10.

The acquisition system records the tension measured between the voltage taps of the coil during the ramping of the current with a sampling time of 0.5 ms and overwrites these data with a period of 1 s until the quench is detected, to avoid managing huge files. To avoid identifying a spike as a quench the signal has to remain over the threshold for more than 10 ms. If this happens the power supply is switched off and the circuit is closed into a resistance and the data with a pretrigger of 250 ms and a post-trigger of 750 ms are saved.

5.4. First test

The first test has been done in a configuration with one NbTi and one Nb_3Sn coil, like shown in Figure 11.

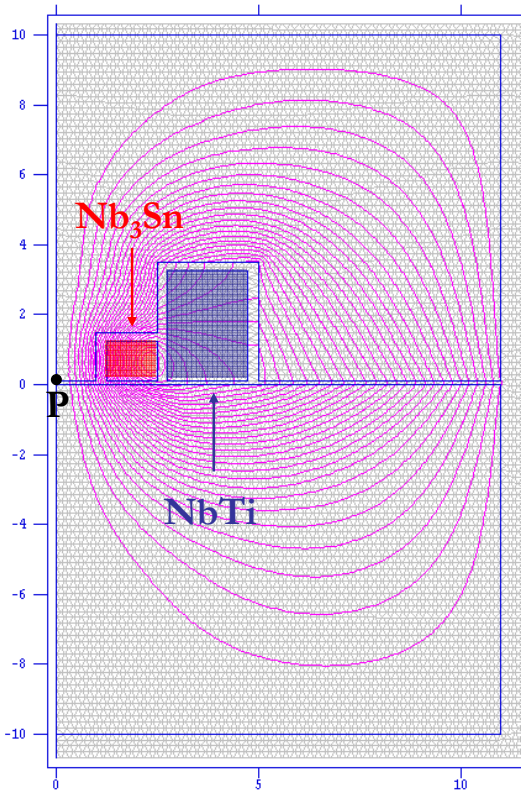

Figure 11. Configuration of the first test. Dimensions are in cm. The magnet is cylindrically symmetric with respect to the vertical axis.

Before the test has been performed some simulation to determine the measurements which are possible in this configuration has been done with the Poisson code.

In particular the magnetic field at the point P(radius = 0 mm and vertical coordinate = 1 mm) indicated in Figure 11, and the currents and the margin to quench at 4.2 K of the two coils are indicated in Table 3.

Nb_3Sn					**NbTi**				
(A)	(T)	(T)	(T)	%	(A)	(T)	(A)	%	(T)
I	Bmax	Bmin	Bc	margin B	I	Bmax	Ic	margin I	B in P
650	10.0	4.1	13	23.1	500	5.2	1200	58.3	9.2
750	10.8	4.0	12	11.8	500	5.2	1200	58.3	9.8
800	11.1	3.8	12	7.5	500	5.3	1177	57.5	10.0
850	11.5	3.8	12	1.3	500	5.3	1174	57.4	10.3
700	11.7	5.7	13	7.0	700	7.0	850	17.6	10.7
800	12.0	5.6	12	2.0	700	7.0	850	17.6	11.0

Table 3. Most significant configurations of the mini-dipole split coil in the first test. Bmax and Bmin are the maximum and the minimum field in the two coils, Ic and Bc are the critical current and field at the operating temperature. The margins in field and in current are also indicated.

The half mini-dipole from the simulations should be able to produce a magnetic field of 11 T with a margin to quench of the order of only few percents in the Nb_3Sn coil. In case of a safety margin of the order of 10% in both the coils the maximum magnetic field is of about 10 T.

The simulated load line of the Nb_3Sn coil in case the NbTi one is switched off is shown in **Error! Reference source not found.**.

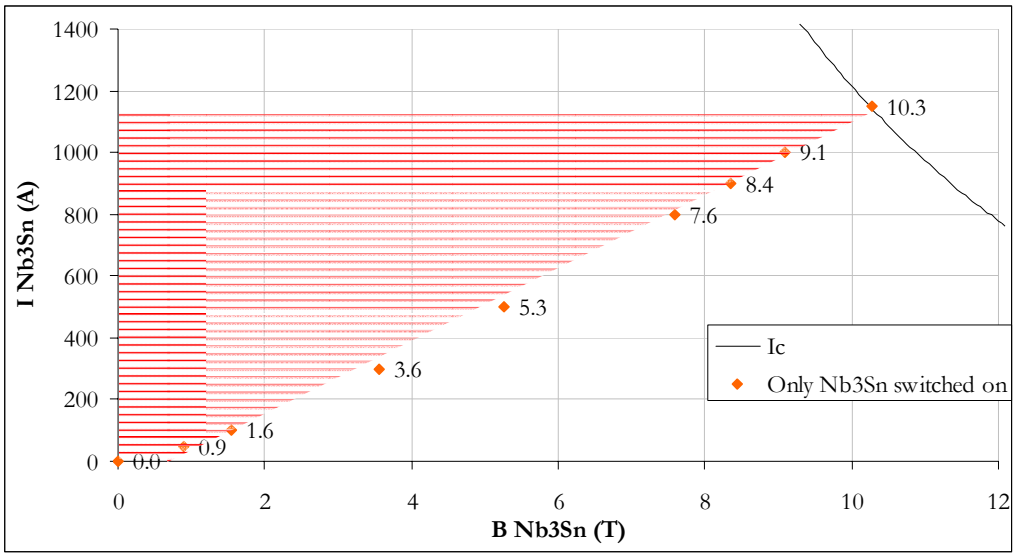

Figure 12. Simulated current versus maximum magnetic field in the Nb_3Sn coil in case the NbTi coil is switched off.

Since the simulated magnetic field at each current in the Nb_3Sn coil is between 0 T and the B on the load line, during the training of this coil it is possible also to explore the region in the (B,I) plane for the flux jump instability shown in the same **Error! Reference source not found.**. This region can be enlarged by switching on also the NbTi coil. In this case the Nb_3Sn coil is supplied at constant current and the NbTi is energized at an increasing current up to a quench is observed in any of the two windings, as shown in Figure 13.

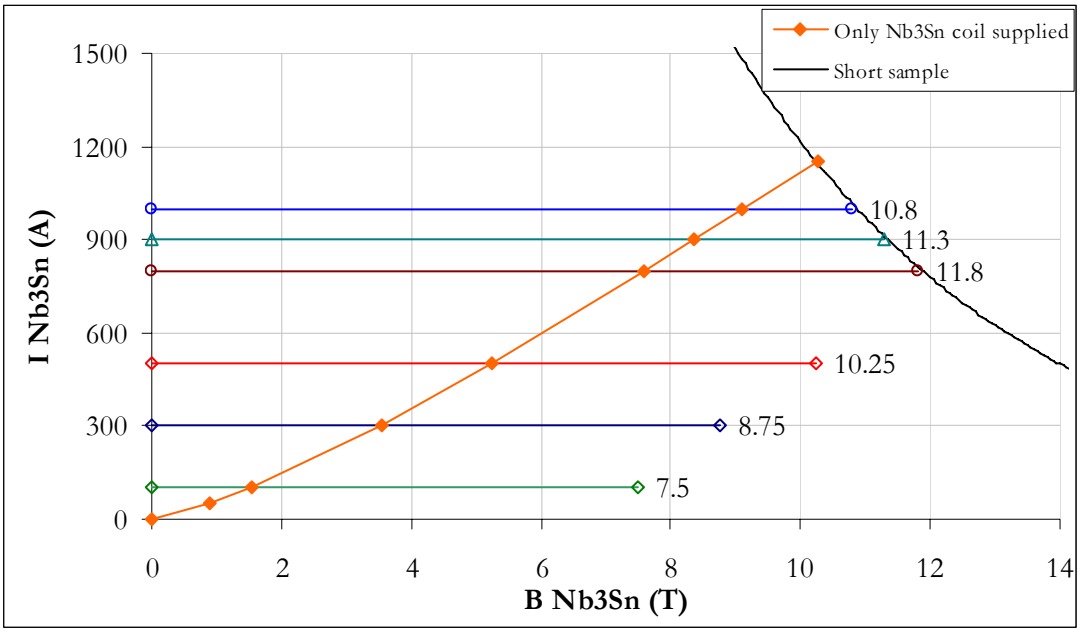

Figure 13. Zones of the magnetic field-current plane in the Nb_3Sn coil supplying also the NbTi coil. The horizontal lines are interrupted, because the critical current of the NbTi or of the Nb_3Sn coil at 4.2 K is reached.

For example at 300 A the maximum value of the magnetic field of 3.6 T, obtained by energizing only the Nb_3Sn coil, can be increased to 8.75, by switching on also the NbTi coil.

Another test which can be performed is the critical current density at 12 T supplying 360 A in the NbTi and 800 A in the Nb_3Sn coil, as shown in Figure 14.

All the experimental measurements have been performed at the operating temperature of 4.2 K if not differently specified.

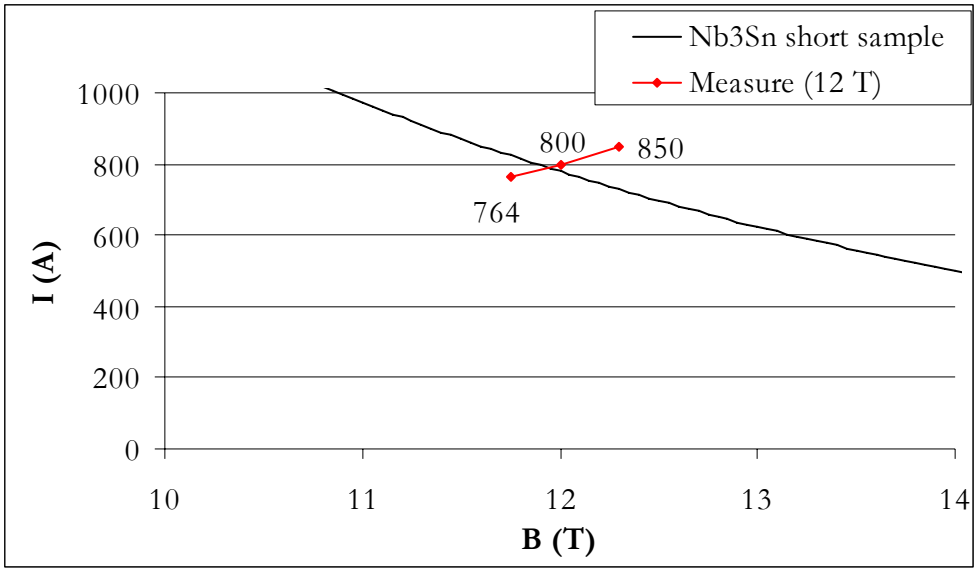

Figure 14. Measurement of the critical current density at 12 T supplying also the NbTi coil at 360 A. The value of the current in the Nb_3Sn coil is also indicated.

The first part of the test was the training of the Nb_3Sn coil with the NbTi coil switched off. From the graph in **Error! Reference source not found.**, the ramp rate of the current has been determined in 1 A/s, which corresponds to a field variation in the typical range for the flux jump instability measurements of 10 mT/s. The results are plotted in Figure 15.

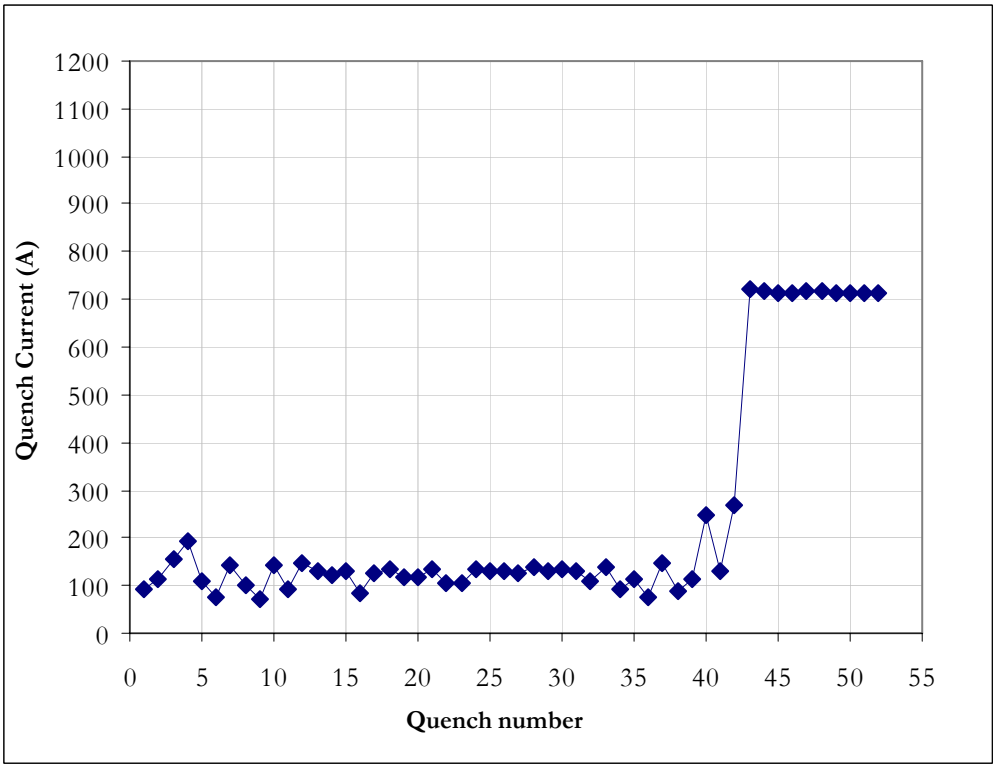

Figure 15. Training curve of the Nb_3Sn coil. The short sample is 1150 A.

During the beginning of the test a lot of over threshold signals, which the detection system identified as quenches, have been detected at currents between about 100 A and 200 A. These signals were due to the tension induced by the variation of the self inductance of the coil, which, in this range of current, varies of more than the 30% of its value from 50 A to 200 A. The quench detection system has then been disconnected during this part of the ramping of the current. After this intervention, the coil reached at the first quench a current of 720 A, which corresponds to the 65% of the short sample limit.

This measurement allowed to explore the region in the plane B-I up to a current of 720 A which on the load line corresponds to a field of 6.9 T (Figure 16).

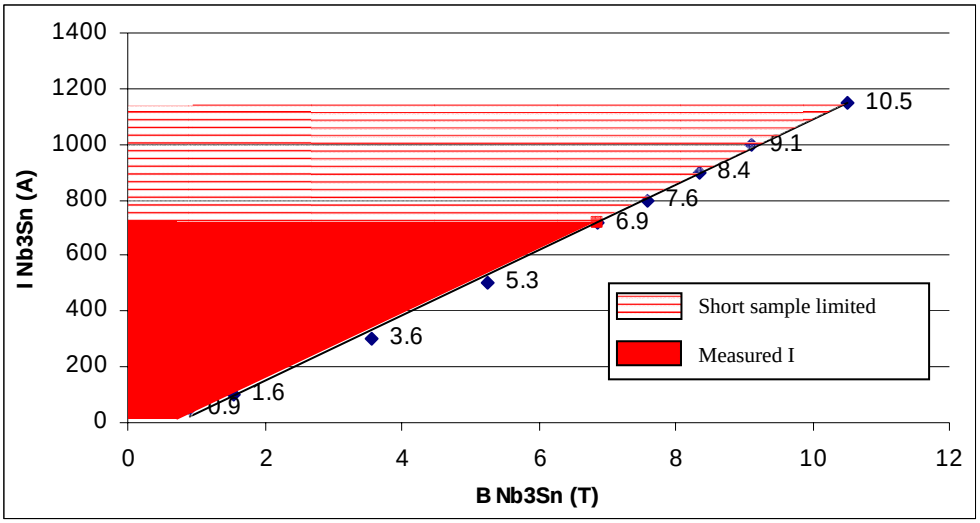

Figure 16. Testable and measured regions in the plane B-I supplying only the Nb_3Sn coil.

Pending further investigation of the reduced performances of the Nb_3Sn coil, it has been decided to test the NbTi coil. In this case the ramp rate of the current has been set to 10 A/s, because only limitation of the maximum tension was taken into account. The measured curve of the training is shown in Figure 17.

After few quenches the coil reached a maximum current of 608 A, which corresponds to the 87% of the short sample limit.

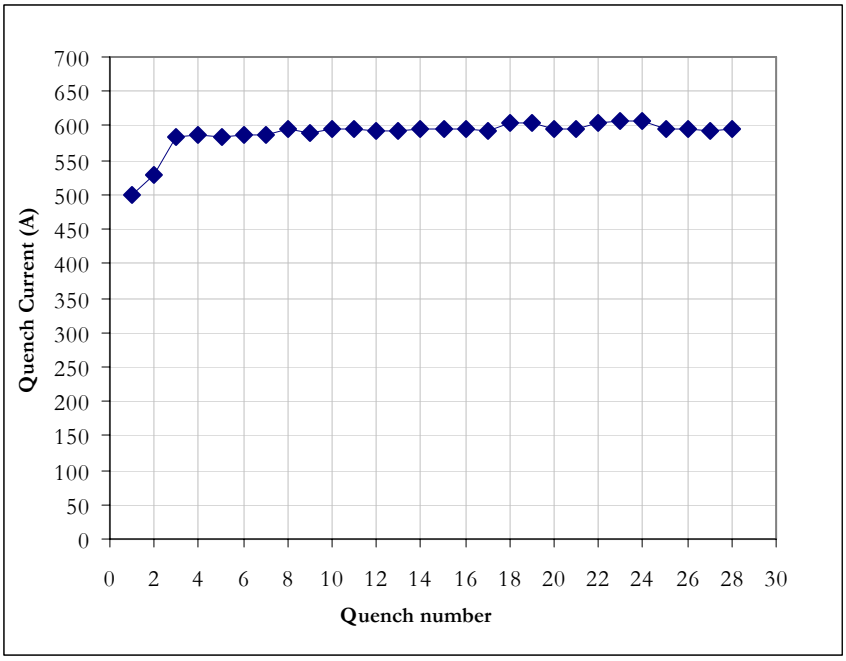

Figure 17. Training curve of the NbTi coil. The short sample is 700 A.

After both coils have been trained the measurements of flux jumping instability supplying also the NbTi coil have been performed. In Figure 18 the results of these measurements in the plane B-I are shown.

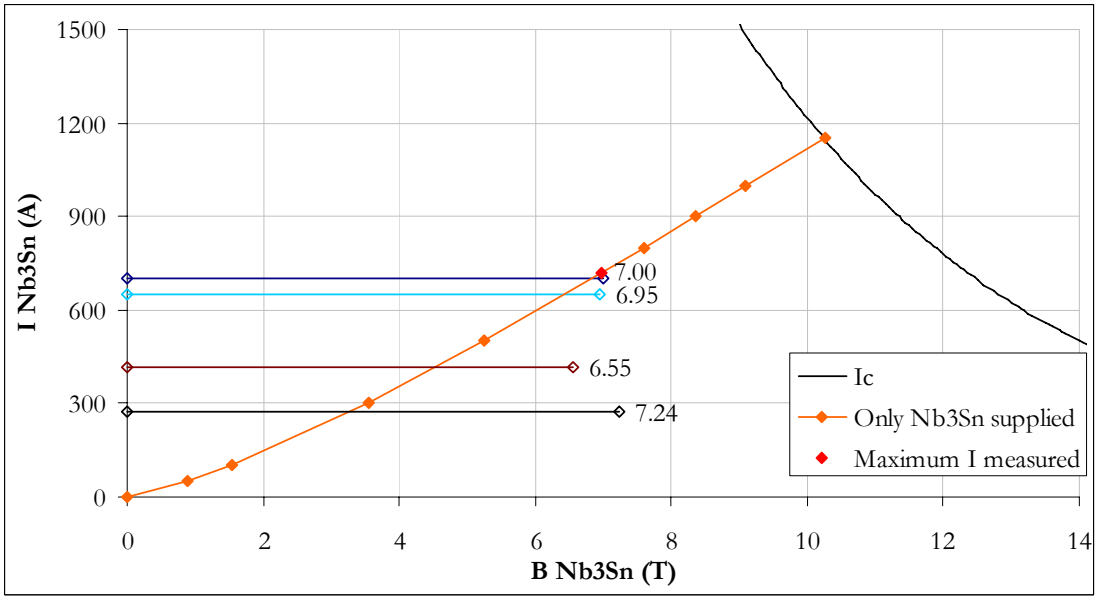

Figure 18. Results of the measurement of flux jumping instability of the Nb_3Sn coil supplying also the NbTi coil.

The Nb_3Sn coil supplied at a given current quenched at values of peak magnetic field on the conductor lower than the expected ones (compare Figure 18 and Figure 13).

This can be attributed to the presence of flux jumping instability at all this low current, in disagreement with the strand tests.

In case the source of the quenches were a mechanical disturbance the quenches would be at constant product current per magnetic field. The distribution of the quenches (Figure 18) allowed to exclude this source and made suppose that the problem has to be attributed to the heat treatment. To have a feeling of the correctness of the heat treatment the measurement of the RRR of the whole coil has been performed. The resistance of the coil at room temperature is 1.1 Ω. The resistance at the critical temperature has been determined during the warm up supplying the coil with a constant current of 5 A. In Figure 19 the resistances of the NbTi and the Nb_3Sn coil are plotted.

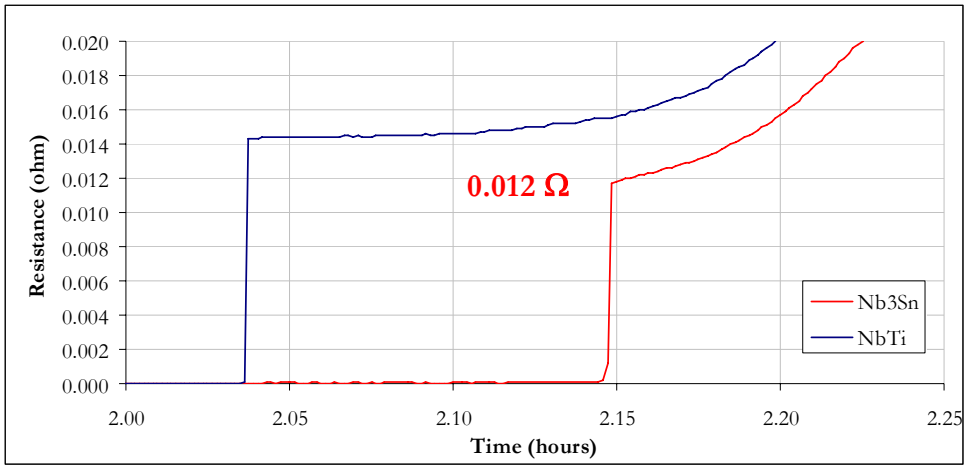

Figure 19. Resistance of the NbTi and the Nb_3Sn coil during the warming up close to the critical temperatures of the two superconductors. The coils have been supplied with a constant current of 5 A.

The Nb_3Sn has RRR = 92, in accordance with the value given by the OI-ST. This allows concluding that a possible mistake in the heat treatment afflicts only a small part of the conductor, since does not sensibly modify the RRR of the whole winding.

5.5. Second test

The second test has been performed to understand and possibly solve the problems identified by the measurements of the first test. If a mistake has been committed in manufacturing the coil of the first test, it has to be searched into the heat treatment to form the superconductor or in the assembly procedure. In particular the possible hypotheses are:

- The heat treatment performed on the coil is more aggressive than the one made on the strand;
- There is a difference between the heat treatment performed on the strand and on the coil, caused by a disuniformity of the temperature inside the winding.

A detailed analysis and tests to verify if the cause of the results of the first test is something related to the heat treatment have been done.

The heat treatment performed on the coil can be different from the corresponding treatment on the strand, because coil and strand are placed in different zone of the furnace. To verify this hypothesis another coil has been heat treated in a furnace at LASA with the same heat treatment procedure of the first coil.

To check if the gradient of the temperature between different points of the coil during the heat treatment can explain the results of the first test, a copper thermal shielding, shown in Figure 20, has been manufactured to improve the uniformity of the temperature.

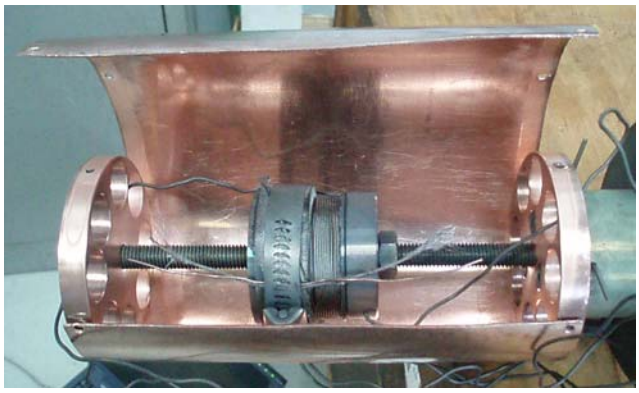

Figure 20. Thermal shielding used at CERN to perform the heat treatment of the coil for the second test.

The coil has been inserted into it and put into the structure of the furnace used during the first heat treatments. This thermal shield reduced of a factor 2 the gradient of temperature in the region of the coil during the reaction, as shown in the graph of Figure 21.

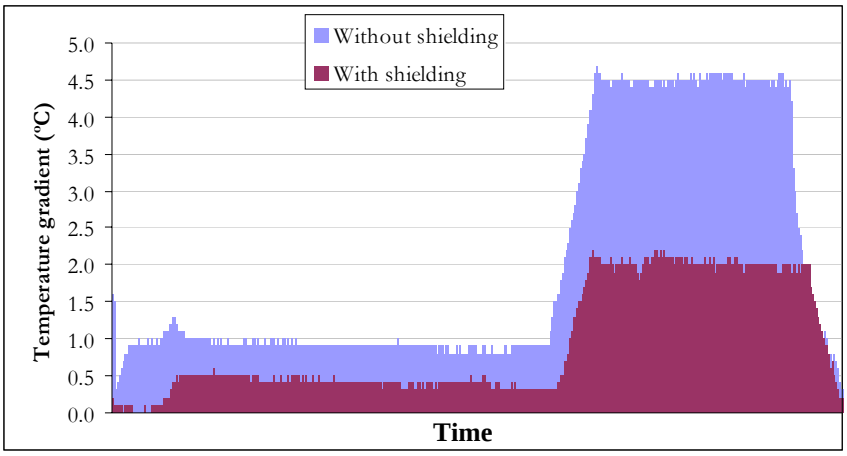

Figure 21. Temperature gradient in the coil region during the heat treatment with the thermal shielding compared to the case without it.

This coil has been heat treated using the sequence shown in Table 4, which should give a more stable strand with higher RRR (about 250 with respect to 89 from the OI-ST measurement) decreasing of less than 3% the critical current density.

	Atmosphere	Ramp		Plateau	Ramp		Plateau
Pre reaction	Circulating air	Rate	Target		Rate	Target	
		25 ºC/h	205ºC	100 h	25 ºC/h	325 ºC	2 h
Reaction	Vacuum/inert	Ramp		Plateau	Ramp		Plateau
		50 ºC/h	400 ºC	48 h	50 ºC/h	665 ºC	50 h

Table 4. Heat treatment of the coil at CERN for the second test. The previous heat treatment has as a last step a plateau at 695ºC for 25 h.

The modifications with respect to the first heat treatment are the doubled duration and the temperature of the last step.

The second test has been performed in the mini-dipole using only the couple of the Nb_3Sn coils, and replacing the NbTi ones with brass blocks, as shown in Figure 22.

In this case the coils can produce a magnetic field of more than 10 T at the pole center (point P in Figure 22) with a margin to quench larger than 10%, as shown in Table 5.

CERN			**Milano**		
I (A)	Margin to quench (%)	B_{Peak} (T)	I (A)	Margin to quench (%)	B_{Peak} (T)
850	14.0	10.4	730	17.2	10.4

Table 5. Most meaningful configuration of the mini dipole split coil in the assembly for the second test.

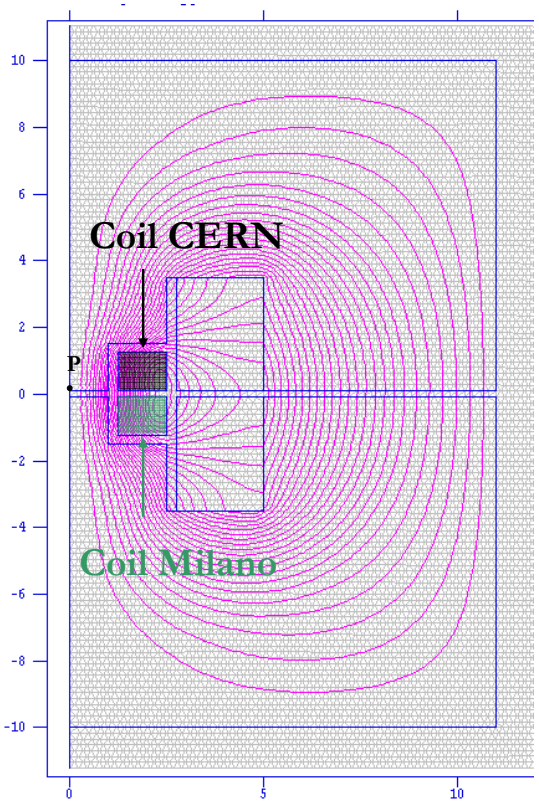

Figure 22. Configuration of the mini-dipole split coil for the second test. Dimensions are in cm. The magnet is cylindrically symmetric with respect to the vertical axis.

To enlarge the explored region of the B-I plane each Nb_3Sn coil can be used to produce the background field for the other one, as done during the previous test by the NbTi coil. The testable zone of the plane B-I in this case is shown in Figure 23.

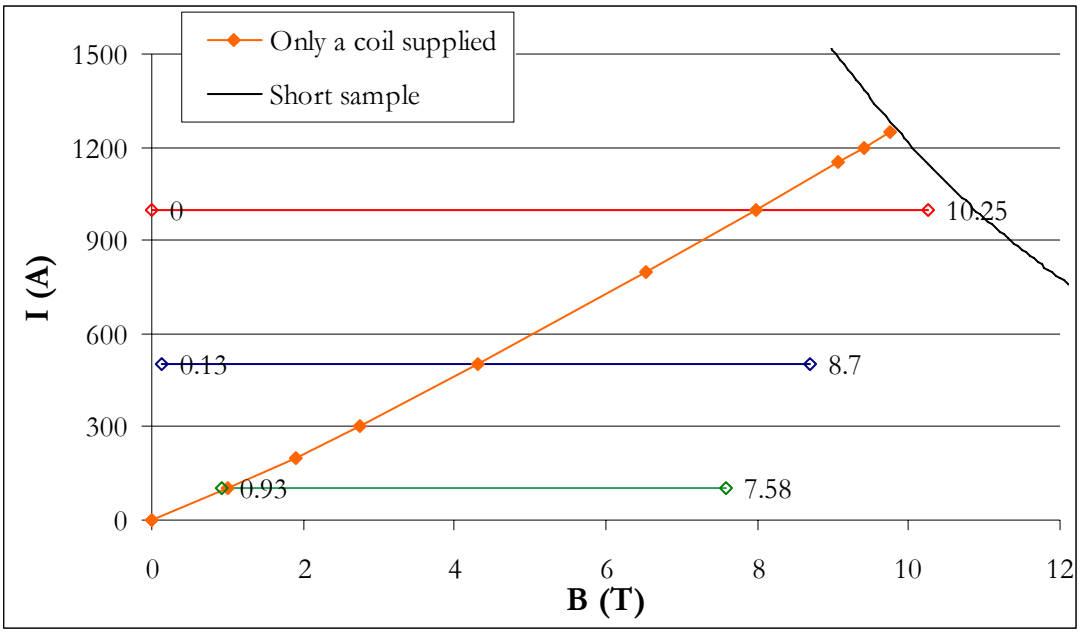

Figure 23. Several zones of the plane magnetic field-current in a coil supplying the other one. The horizontal lines are stopped in correspondence of the critical curve at 4.2 K in one of the two coils.

In Figure 24 the training curves of the coil heat treated at Milano and of the one at CERN for the second test are shown.

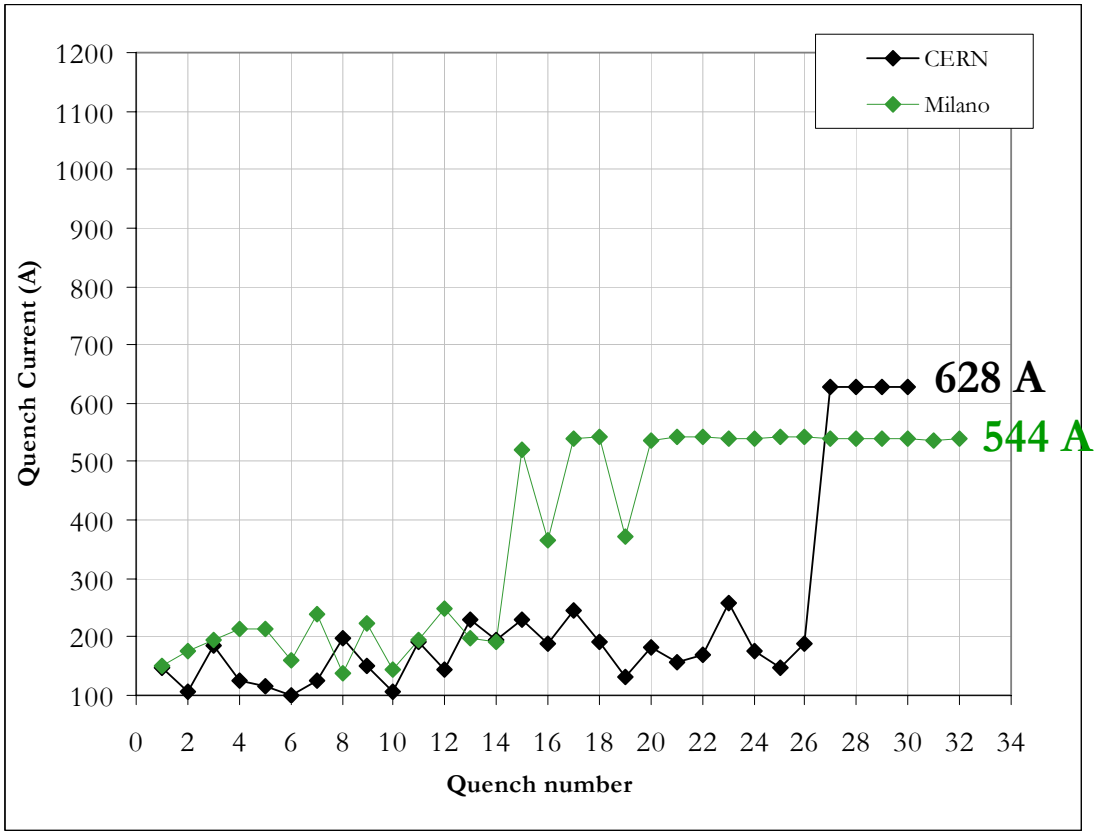

Figure 24. Training curves at 4.2 K of the two coils of the second test.

The value of the quenching current was 544 A for the coil heat treated at Milano and 628 A for the one heat treated at CERN. Possible explanations of this limitation are:

- The filaments of the Nb_3Sn have been broken and the measured value of the current corresponds to the critical curve of the superconductor;
- Mechanical instability;
- Flux jumping instability;
- Heating of one or more points of the coil.

In the first two cases (broken filaments or mechanical instability), the maximum current should decrease by increasing the magnetic field. In the last case (hot point) the maximum current should be independent from the magnetic field where the conductor is immersed except the negligible variation of the resistance for the magneto resistance phenomenon. In the case that the quench is induced by flux jumping instability no conclusion can be obtained from a measurement in a different magnetic field. In fact, if the region of instability is present at low fields, a sufficiently

high background field could raise the maximum current, but if the instability is at higher field, the increase of the field does not change the value of the maximum current.

In Table 6 the measured current and the maximum magnetic field onto the two coils in the case the two coils are supplied in series to increase the magnetic field compared with the measurement with only one coil supplied is shown.

	I (A)	B_{MAX} (T)
Only one coil supplied	544	4.65
In series	540	5.6

Table 6. Current and maximum magnetic field on the conductor for only one coil supplied and for two coils connected in series.

This measurement allowed to exclude the hypothesis of broken filaments or a mechanical instability, because the maximum current resulted independent from the magnetic field where the superconductor is immersed.

To discriminate between the flux jumping instability or the heating of a point, the measurement of the maximum current has been repeated at 1.9 K. It has been predicted and experimentally demonstrated [3], in fact, that for Nb_3Sn the flux jumping is more critical at 1.9 K than at 4.2 K.

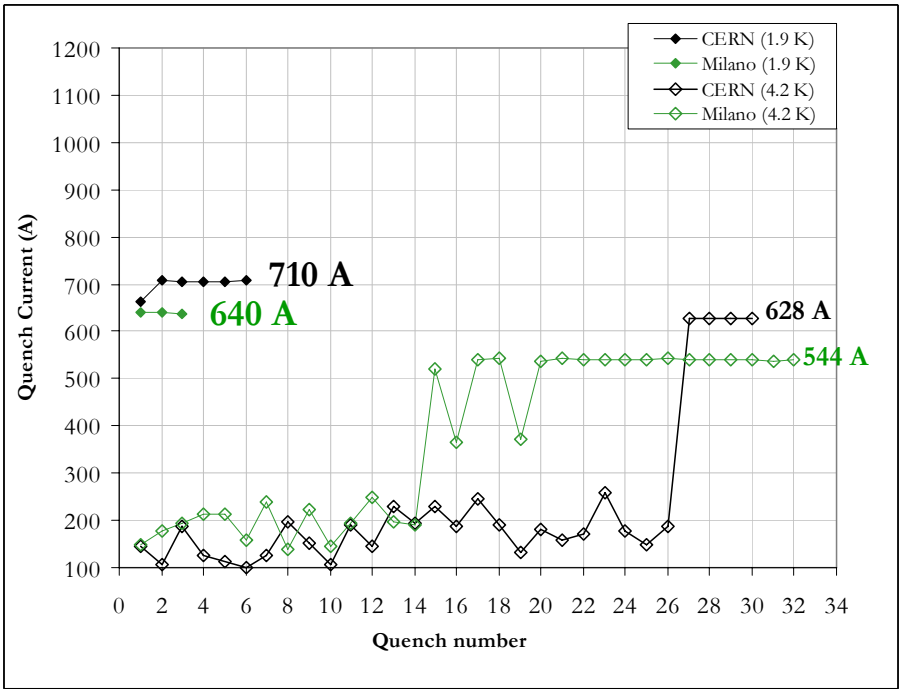

Figure 25. Training of the two coils of the second test at 1.9 K. For comparison also the measurements at 4.2 K are reported.

The training curve at 1.9 K for both coils is shown in Figure 25.

For both coils the value of the current increased, proving together with the test at different fields at 4.2 K, that the limitation of the current is due to the heating of a point of the coil, possibly located at the connection between the NbTi and the Nb_3Sn (see Figure 3).

As in the first test, the measurement has been performed to explore the zone of the plane B-I up to the allowable current and at fields between 0 T and the load line, as shown in Figure 26.

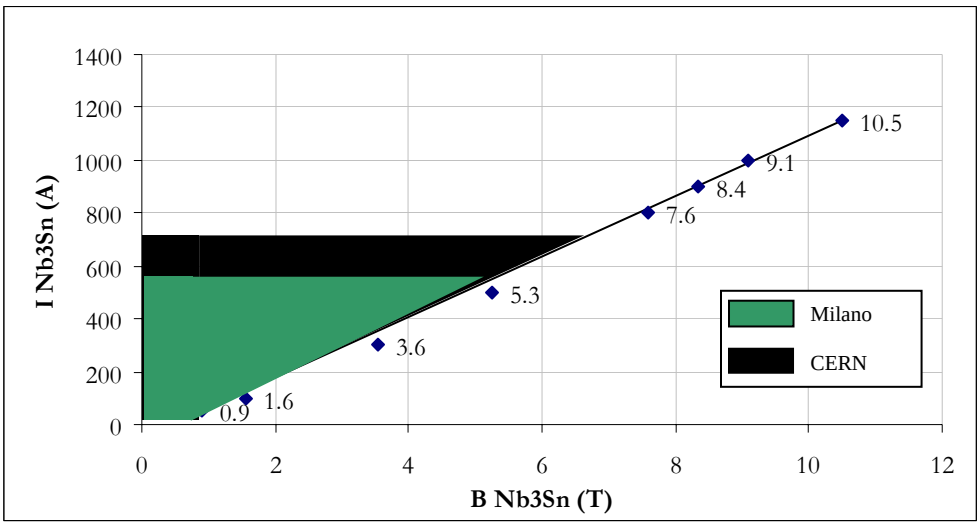

Figure 26. Measured zone in the B-I plane during the training of the two coils.

The subsequent step of the test was to enlarge the explored zone of the plane supplying the coil under test by a constant current and ramping the current in the other coil until a quench is observed.

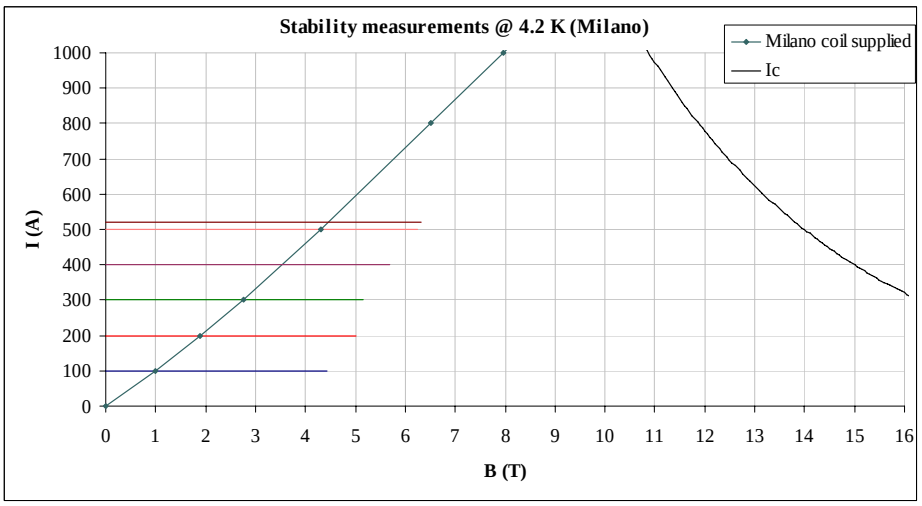

Figure 27. Measurement of flux jumping instability at 4.2 K for the coil heat treated in Milano.

The results for the coil heat treated in Milano are plotted in Figure 27.

For all the values of current no quenches have been detected in the coil heat treated in Milano, and the measurements have been stopped at the maximum current in the coil heat treated at CERN. These tests allowed to conclude that no flux jumping or mechanical instabilities are present in the coil heat treated at Milano.

The results of the analogous measurement on the coil heat treated at CERN are presented in Figure 28.

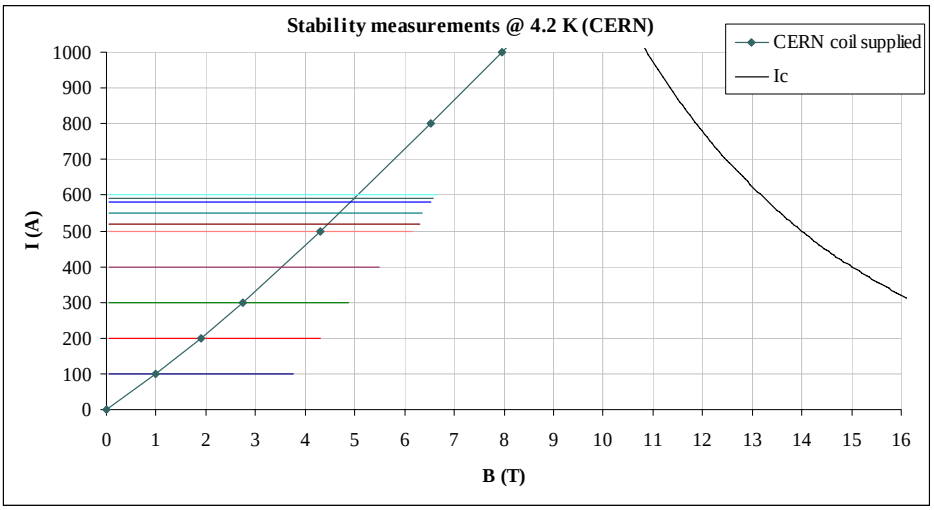

Figure 28. Measurement of flux jumping instability at 4.2 K for the coil heat treated at CERN.

No quenches in the coil in test have been detected, and the measurements have been stopped at the maximum current of the coil heat treated at Milano. Also for this coil flux jumping or mechanical instabilities have been excluded.

This measurement has been repeated at 1.9 K, considering the fact that the flux jumping instability gets worse at lower temperature. If no instability is detected at this temperature there will be not stability also at the operational temperature of the undulator. At this temperature the background field can be increased allowing to explore a larger region of the plane B-I.

The results of the measurement on the coil heat treated at Milano are presented in Figure 29.

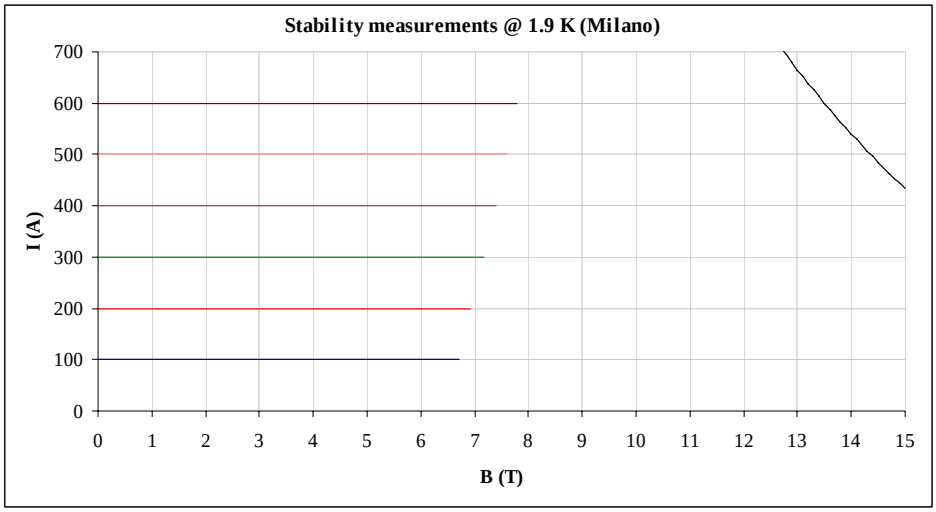

Figure 29. Measurement of flux jumping stability at 1.9 K for the coil heat treated at Milano.

At 1.9 K it was possible to reach 7.78 T at 600 A on the conductor with respect to 6.24 T with a current of 500 A in the case of the measurement at 4.2 K. No instabilities have been detected, and all the measurements have been stopped because the maximum current at 1.9 K for the coil heat treated at CERN has been reached.
The results of the similar measurements for the coil CERN is presented in Figure 30.

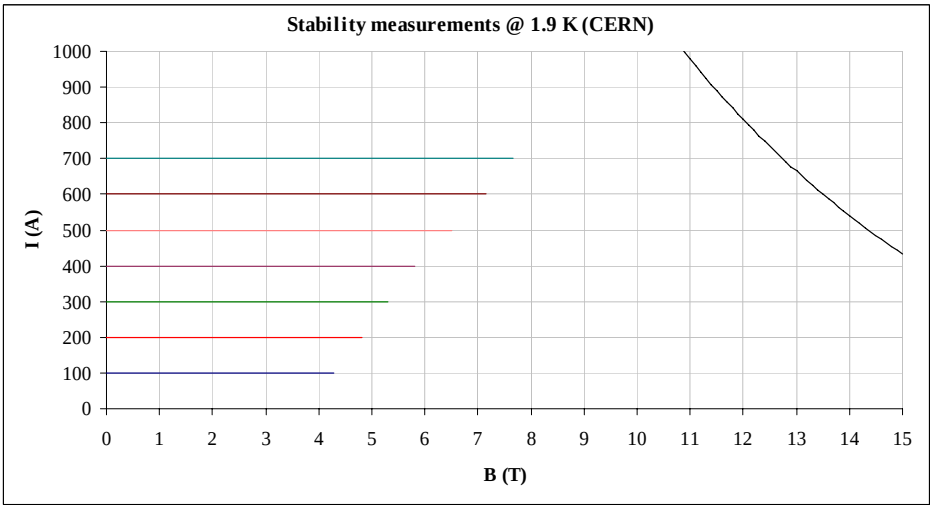

Figure 30. Measurement of flux jumping stability at 1.9 K for the coil heat treated at CERN.

In this case it was possible to reach 7.66 T at 700 A on the conductor with respect to 6.30 T with a current of 520 A in the case of the measurement at 4.2 K. Also in this case the measurement didn't evidence any instability.

5.6. Alternative design

No flux jumping or mechanical instabilities have been detected during the test of the coils. These measurements however didn't allow to explore the whole region of the plane B-I of the first proposed design of the undulator. In Figure 31 the comparison between the load lines of the undulator coils of this design and the results of the measurements at 1.9 K, which are the worst cases for the flux jumping instability, is shown.

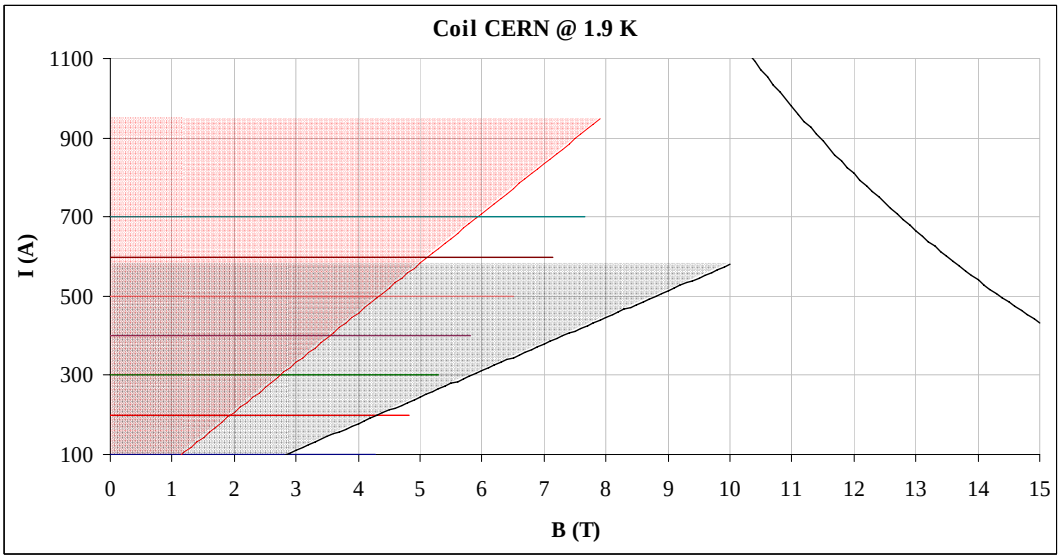

Figure 31. Load lines of the short and long period configurations of the coils of the undulator. The colored area indicates the magnetic fields of the coils during the ramping of the current.

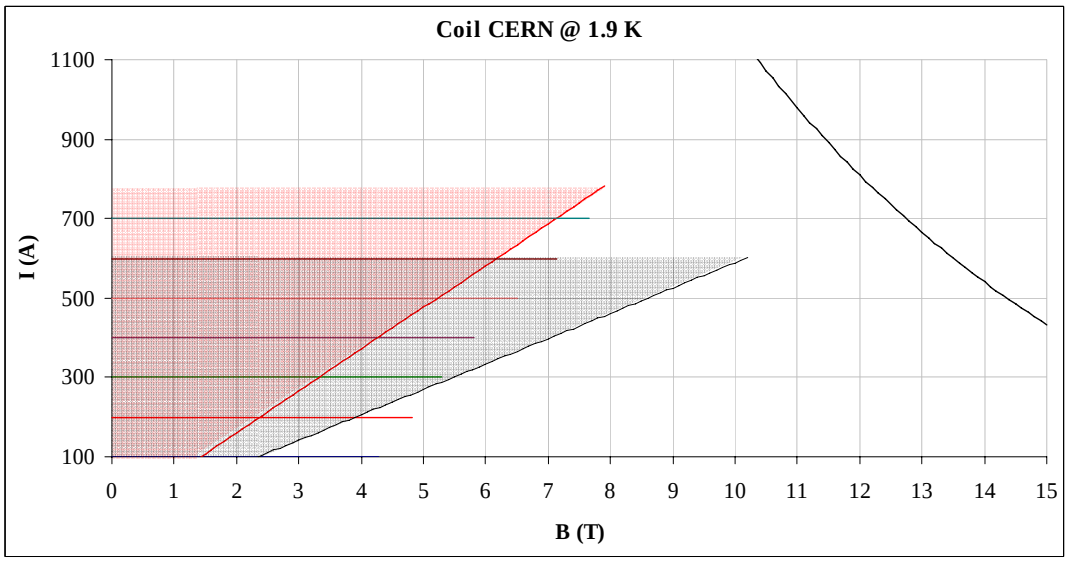

Figure 32. Load lines of the short and long period configurations of the coils of the undulator made after the strand stability measurements. The colored area indicates the magnetic fields of the coils during the ramping of the current.

A similar graph for the design made after the flux jumping instability measurements on the strand is presented in Figure 32.

These measurements didn't allow to demonstrate the feasibility also of the coils of this second design.

Another design of the coils of the undulator has therefore been studied, imposing the maximum current of the coils of both configurations to 700 A, since up to these current values no flux jumping instability has been detected. In Table 7 the most important parameters of the design for the coils of the two configurations are shown.

	λ = 140 mm	λ = 280 mm
Gap (mm)	60	
Number of periods	2	
Current (A)	700	550
B_0 1 (T)	3.20	5.16
B_0 2 (T)	3.05	4.82
Margin to quench (%)	26.3	14.4
Number of layers	24	61
Number of turns	16	16
Length of the cable for 8 coils (km)	1.25	3.90
Total length of the cable for both the configurations (km)	5.15	

Table 7. Specifications of the alternative design of the undulator.

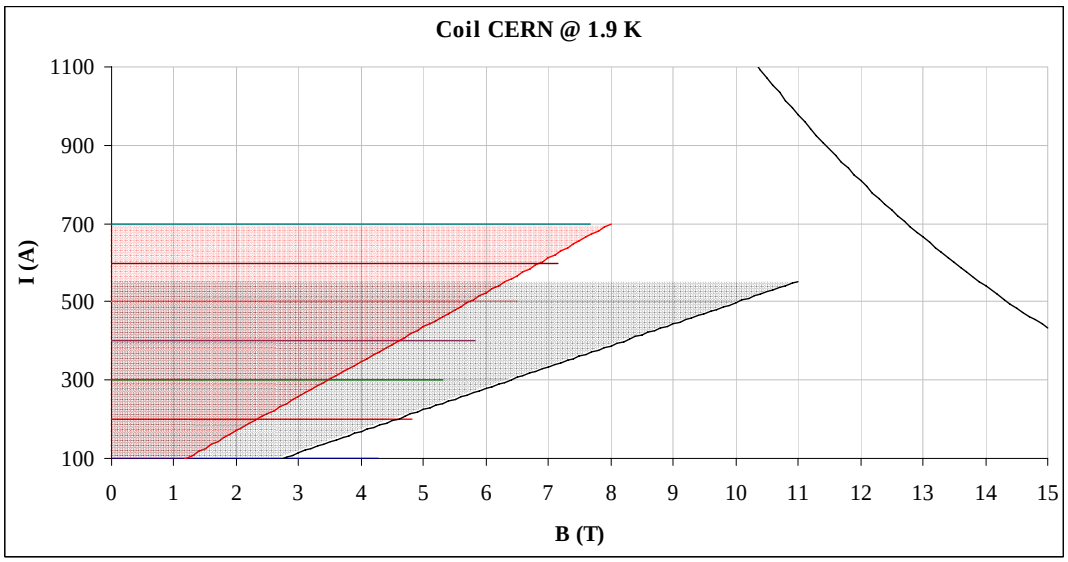

Figure 33. Load lines of the short and long period configurations of the coils of the undulator made after the tests of the coils. The colored area indicates the magnetic fields of the coils during the ramping of the current.

The load lines of the coils of the short and the long period configuration according to this new design are shown in Figure 33.

In case future measurements will put in evidence a region of instability at current above 700 A. This design should be safe although with a safety margin depending on the precise value of the current at which the flux jump instability starts.

5.7. Conclusions

The design, the manufacture and the test of coils made using the OI-ST strand to be used for the LHC undulator have been presented. Following the unsatisfactory results of the first test, modifications have been applied to make a second and a third coil. In particular a new heat treatment has been used and the uniformity of the temperature on the coil has been improved of about a factor 2 in the highest temperature step. In parallel another coil has been heat treated in another furnace. The second test performed on these coils didn't put in evidence any flux jumping or mechanical instability in the testable region of the plane B-I up to 700 A, limited by a point disturbance probably located in the connection between the NbTi and the Nb_3Sn. In case that future measurements will put into evidence flux jumping instability at currents higher than the tested one, an alternative design of the undulator has been studied and presented.

APPENDIX A

FINITE DIFFERENCE QUENCH SIMULATION CODE

Quench is the transition of a superconductor into the normal resistive state. This phenomenon, being the superconductors are able to sustain high current densities, may produce a large overheating of the magnet, which in the worst cases can also degenerate in the melting of the winding. To protect a superconducting magnet in case of quench, the coils are coupled with a circuit of protection, a system of resistances and/or diodes which have the scope to extract and to dissipate part of the stored energy. In the scientific community several quench propagation codes are available to preview the evolution and the effect of a quench in superconducting coils. Each of them has specific features and limitations. For example some tools discretize the coil into “global volumes”, which don’t reflect the real topology of the winding and they perform calculation based on the value of the quench propagation speed determined from a more or less approximated formula. The simulation tool I developed during this work of thesis and described in this appendix is a finite difference code. It meshes the coil reflecting as more as possible the real thermal and electrical characteristics of the winding and it determines the evolution of the quench

starting from the heat balance equation and the value of the quench propagation velocity, instead of imposing it. The code is also capable to determine the evolution of the tensions, the currents and the voltages developed in each element of the circuit of protection and the 3D temperature map of the quenching coil in function of time, known the properties of the wire, the geometry of the coil and the temperature of the helium bath.

A.1. Introduction

Superconductivity is a phenomenon whereby some materials, under opportune circumstances have zero electrical resistance. These materials remain in this state if their temperature, magnetic field and current density identify a point below its critical surface in the (T, B, J) 3D space. This is true for a short sample test, but it has been experimentally observed that the performances of a wire are degraded when it is used to wind a coil, which usually quenches below the critical surface. When a superconducting magnet is tested it shows a progressive improvement of its performances after a series of quenches. This phenomenon is known as "*training*". A quench can be induced by several kinds of disturbances. They can be classified in continuous or transient, which can be divided in point-like or distributed ones. The continuous disturbances, which might be caused for example by a bad joint between two conductors (point-like), or by a fault of the cryogenics system (distributed), don't produce training, although they may be responsible of degradation. They can be eliminated by an accurate design and manufacture process. The responsible of the training are instead the transient disturbances, as flux jumping and mechanical instabilities. Because of the small value of the specific heat of the materials at the cryogenics temperatures, a quench can be initiated also by a small release of energy, which, for the same reason, can produce very high hot spot temperature. For a typical NbTi winding at 6 T at 4.2 K the deposition of a density of energy of about 750 J/m^3, which at room temperature would produce an increment of temperature of only $2.5x10^{-4}$ K, is enough to start a quench [1]. It is possible to calculate that this density of energy can be produced by a movement of the conductor of the order of micrometers [1]. These numbers give the idea of the importance of carefully protecting the coil in case of quench. The tool I developed has been used to simulate the behavior of the coils designed and manufactured during this work of thesis.

A.2. Structure of the code

Most of the codes used for quench studies use a pseudo-analytical model based the scheme proposed by Wilson [1]. In these tools at the beginning the normal resistive zone starts to grow at the quench velocities both in the longitudinal and in the transverse dimensions, in such a way that at the end of the first temporal step the volume of the normal zone is an ellipsoid. At each other iteration another layer is added to the normal resistive zone of the previous step and the increase of the temperature in each one of these layers and the resistance of quench are updated. This resistance is used to solve the equation of the circuit to determine the current circulating in each element. The flow-chart of this kind of codes is presented in Figure 1.

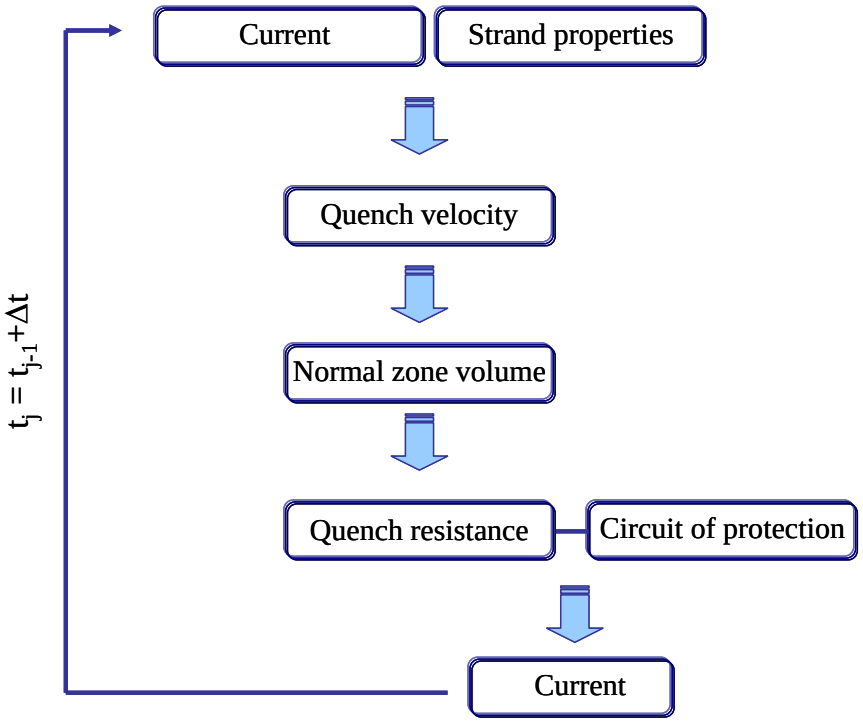

Figure 1. Flow-chart of the codes which start from the determination of the quench propagation velocity to simulate the quench evolution.

The most important limitations of this kind of tools are that they consider the superconducting coil as a global volume and that the evolution of the quench is based on the values of the propagation velocities calculated by a more or less approximated formula.

In the last years a new approach based on a finite difference method has been developed. In this approach the coil is meshed in such a way that each unit represents the real turns and layers of the winding and the heat balance equations are written and solved to determine the temperature map of the magnet. This kind of approach eliminates the limitations of the previous code. The flow-chart of this kind of code is shown in Figure 2.

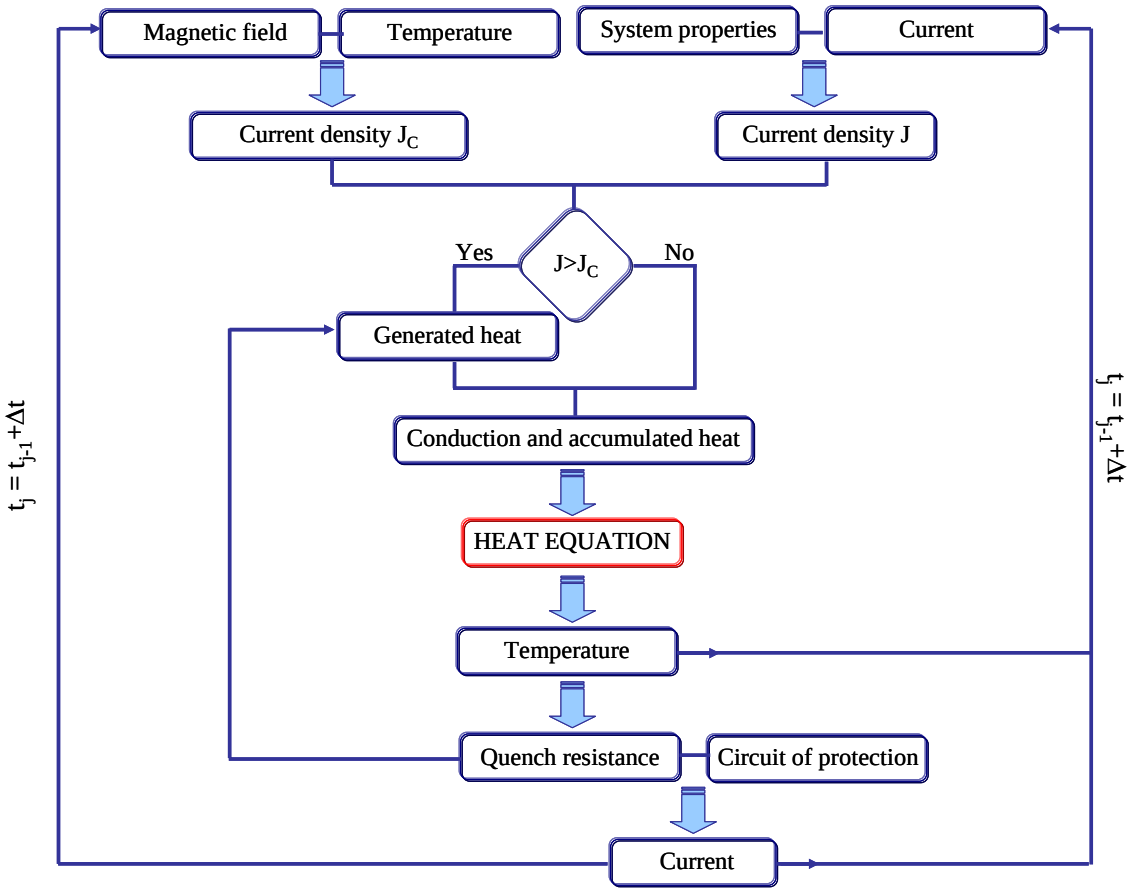

Figure 2. Flow-chart of the codes which start from the determination of the quench propagation velocity to simulate the quench evolution.

Initially the code produces a mesh of the coil and the quench is initiated by imposing that one or more of these units are resistive and therefore generating heat. At each temporal step and for each unit, known the properties of the materials and the current, the current density J in the superconductor is determined and compared to the critical one J_C, in function of the temperature and of the magnetic field. If J exceeds the critical value, the unit is considered in quench, then it contributes to the total quench resistance of the coil and it produces a term of heat generation in the heat balance equation. This equation is solved to determine the temperature, which are also used to update the materials properties for the successive iteration. Known the characteristics

of the circuit of protection, the resistance of the quenching coil and the inductances of all the coils, the currents are calculated. They are useful to determine the developed tensions and energies and to update the current density of the successive iteration. These steps are repeated until the current or the time reach a user defined value.

The inputs of the code are:

- Strand specifications: dimensions, proportions of superconductor, copper and insulation, copper RRR;
- Coil characteristics: dimensions, layer and turns;
- System features: starting current, bath temperature, resistances of the circuit of protection and inductances, starting point of the quench, dependence of the magnetic field on the conductor in function of the spatial coordinates;
- Code parameters: minimum current and maximum time at which stop the simulation, first temporal step, tolerance on the solution, maximum allowed temperature variation in a temporal step.

The code gives in output:

- The 3D temperature map and in particular the hot spot temperature;
- The current, the voltages, the resistance of quench and the tensions developed in each coil and in all the elements of the circuit of protection in function of the time;
- The velocity of propagation of the quench in all the 3 dimensions.

In the next sections a more detailed description of the most important aspects of the code is given.

A.3. Mesh of the coil

In Figure 3 a schematic coil section in the x-y plane is shown. In the same figure the mesh of the coil in the same plane is also indicated.

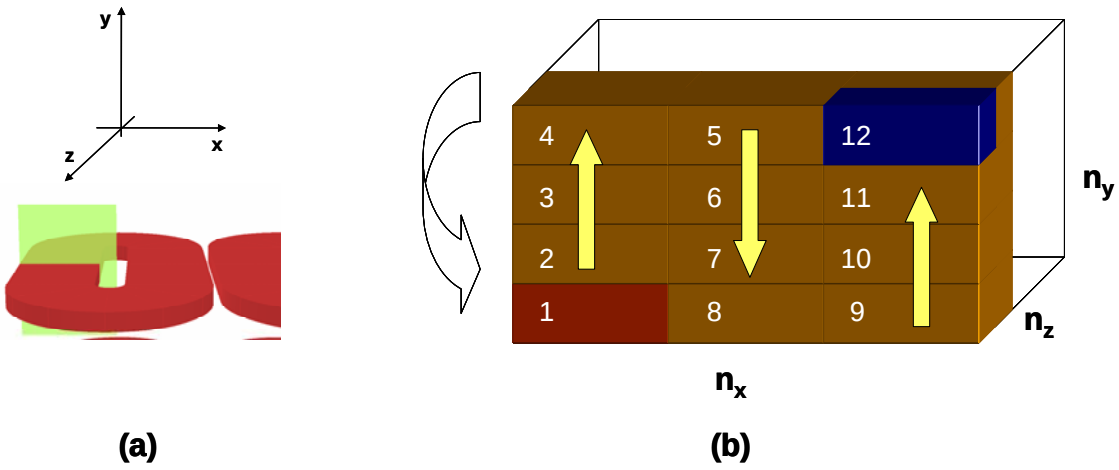

Figure 3. Mesh of the coil in quench. (a) Section of the coil. (b) Section in the x-y plane of the coil in quench. The coil has n_x turns, n_y layers and n_z units in the longitudinal dimension respectively. In the same figure the path of the current is also shown.

The coil is subdivided into n_x, n_y and n_z units along the x, y and z dimension respectively, determined in such a way that the dimensions of the cells in the direction x and y correspond to the real number of turns and layers. The connections between the units are performed following the path of the current, which enters in the coil through the cell indicated by 1 in Figure 3 and, after n_z units along the z axis, passes to the next layer starting from the cell indicated by 2 and so on. After the top layer the current goes in the next turn passing through the unit indicated as 5 in the same Figure 3 and after n_z blocks along the z axis it goes to the cell indicated by 6 and so on. This mesh allows reflecting more precisely the real thermal and electrical contact between the elements of the coil. In this way it is possible to correctly describe the evolution of the quench in case it does one or more turns along the z axis.

A.4. 3D heat balance equation

The heat equation is of the form:

$$C_S(x,y,z,t)m\frac{\partial T(x,y,z,t)}{\partial t} = R_Q(x,y,z,t)I(t)^2 - \sum_{i=x,y,z} k_i(x,y,z,t)A_i\frac{\partial T(x,y,z,t)}{\partial x_i} \quad (1)$$

The term on the left represents the stored heat, given by the product of the specific heat, the mass and the time derivative of the temperature. The first term on the right side is the internal heat generated, present only in the case the current density overcomes the critical ones. The last term describes the heat conduction between the turns and the layers of the windings. It is given by the product of the thermal

conductivity multiplied by the surface of contact and the space derivative in each one of the three dimensions. Because the code has been developed to study the behavior of fully impregnated coils, the helium cooling has been neglected. The (1) is a space and time partial derivative equation, which can be solved analytically only in very restricted hypothesis [2, 3]. A finite difference method, which discretizes the time and the space, has been used to determine its solution. The time discretization is obtained solving the equation for each temporal step, whereas the spatial one has been satisfied by meshing the coil in quench. It has been considered that each unit is influenced only by the neighboring ones, as schematically shown in Figure 4.

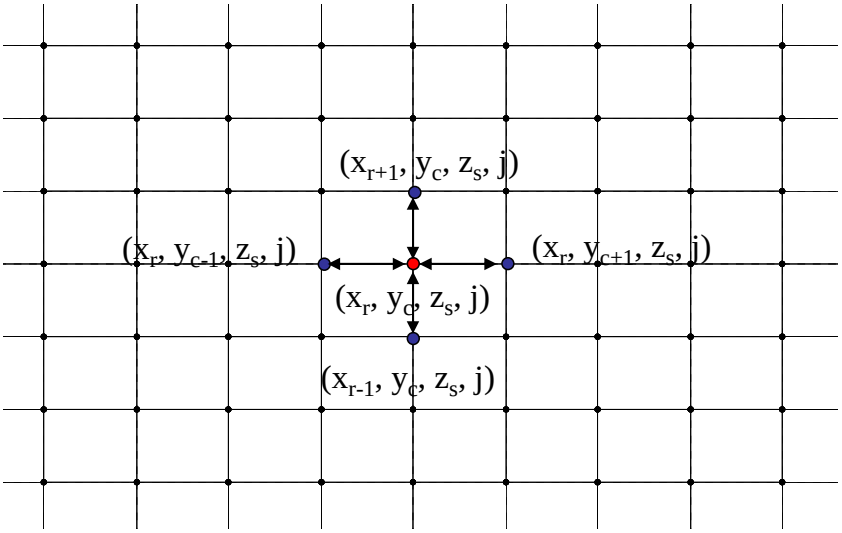

Figure 4. The finite difference method discretizes the space in a grid of points. The point in the center interacts with the neighboring ones. The interaction in the longitudinal direction z with the units (x_r, y_c, z_{s-1}) and (x_r, y_c, z_{s+1}), is not indicated for simplicity. The j index refers to the time.

In these hypotheses the time derivative becomes:

$$\frac{\partial T(x_r, y_c, z_s, t_j)}{\partial t} = \frac{T(x_r, y_c, z_s, t_j) - T(x_r, y_c, z_s, t_{j-1})}{t_j - t_{j-1}} \qquad (2)$$

and the space derivative, for example along z for an internal unit:

$$\frac{\partial T(x_r, y_c, z_s, t)}{\partial z} = \frac{T(x_r, y_c, z_s, t_j) - T(x_r, y_c, z_{s-1}, t_j)}{z_s - z_{s-1}} \qquad (3)$$

Because of the coupling of the equations introduced by the term which contains the thermal conductivity, at each temporal step the code has to solve a system of nx x ny x nz equations. A way to uncouple these equations is to assume that the temperature of the closest points can be considered constants in the calculation of $T(x_r, y_c, z_s, t_j)$ of the considered unit, i. e. for example in z:

$$T(x_r, y_c, z_{s-1}, t_j) \approx T(x_r, y_c, z_{s-1}, t_{j-1}) \tag{4}$$

but this approach would give only a very approximated solution of the problem, and then it has been discharged. The system of equations has been made linear assuming the less strong hypothesis that only the material properties are constant during the time of one iteration. Under this condition the system can be written in the matricial form as:

$$AT = B + R_Q I^2 \tag{5}$$

where the 3D matrices A, B and R_Q are in biunivocal correspondence with the units of the coil in quench. In particular the matrix A contains all the terms which are multiplied by the temperature at the temporal step of the current iteration, the matrix B the term which are multiplied by the ones of the previous time, and R_Q the quench resistance of each unit. In a section of the x-y plane these matrices can be written as:

$$A \equiv \begin{bmatrix} \dots & \dots & \dots & \dots & \dots \\ \dots & \dots & -\dfrac{k(x_{r+1}, y_c, z_s, t_{j-1})A_x}{x_r - x_{r+1}} & \dots & \dots \\ \dots & -\dfrac{k(x_r, y_{c-1}, z_s, t_{j-1})A_y}{y_c - y_{c-1}} & C_S(x_r, y_c, z_s, t_{j-1})\dfrac{m}{t_j - t_{j-1}} + \sum_{i=x,y,z} \dfrac{k_i(x_r, y_c, z_s, t_{j-1})A_i}{i_r - i_{r-1}} + \dots & -\dfrac{k_i(x_r, y_c, z_s, t_{j-1})A_y}{y_c - y_{c+1}} & \dots \\ \dots & \dots & -\dfrac{k(x_{r-1}, y_c, z_s, t_{j-1})A_x}{x_r - x_{r-1}} & \dots & \dots \\ \dots & \dots & \dots & \dots & \dots \end{bmatrix} \tag{6}$$

$$B \equiv \begin{bmatrix} \dots & \dots & \dots & \dots & \dots \\ \dots & \dots & T(x_{r+1}, y_c, z_s, t_{j-1}) & \dots & \dots \\ \dots & T(x_r, y_{c-1}, z_s, t_{j-1}) & T(x_r, y_c, z_s, t_{j-1}) & T(x_r, y_{c+1}, z_s, t_{j-1}) & \dots \\ \dots & \dots & T(x_{r-1}, y_c, z_s, t_{j-1}) & \dots & \dots \\ \dots & \dots & \dots & \dots & \dots \end{bmatrix} \tag{7}$$

$$R_Q \equiv \begin{bmatrix} \dots & \dots & \dots & \dots & \dots \\ \dots & \dots & R_Q(x_{r+1}, y_c, z_s, t_{j-1}) & \dots & \dots \\ \dots & R_Q(x_r, y_{c-1}, z_s, t_{j-1}) & R_Q(x_r, y_c, z_s, t_{j-1}) & R_Q(x_r, y_{c+1}, z_s, t_{j-1}) & \dots \\ \dots & \dots & R_Q(x_{r-1}, y_c, z_s, t_{j-1}) & \dots & \dots \\ \dots & \dots & \dots & \dots & \dots \end{bmatrix} \tag{8}$$

The (5) is then solved multiplying its right term by the inverse of the matrix A.

The hypothesis that the materials properties remain constant during each iteration to make linear the system of equations could be satisfied making an infinitesimal temporal step, but this request is not compatible with a reasonable running time.

Another technique has then been used. The typical temperature evolution in time for a unit is shown in Figure 5.

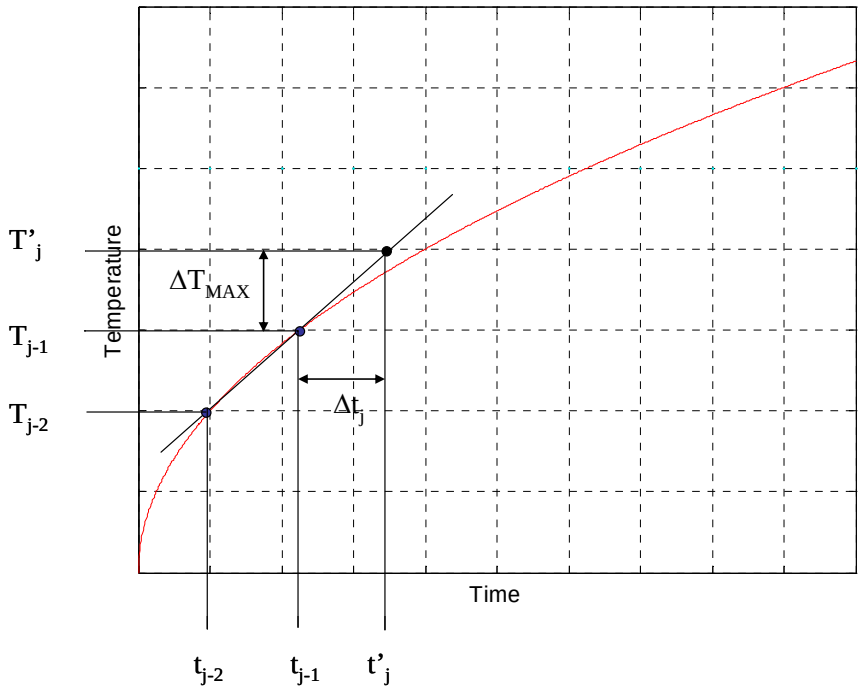

Figure 5. Typical time evolution of the temperature in a unit. The time step of the j[th] iteration is determined from the rate of temperature of the previous iteration. T'_j is the expected temperature assuming that the rate of T is the one determined from the previous iterations.

This curve is used to calculate the temporal step Δt_j, which is dynamically adapted to the quench evolution. To determine the temporal step of the j[th] iteration Δt_j, the code computes the angular coefficient of the line which describes the variation of the temperature between the two previous temporal steps j-2 and j-1, m_j, as:

$$m_j = \frac{T_{j-1} - T_{j-2}}{t_{j-1} - t_{j-2}} \qquad (9)$$

where the meaning of the terms is evident from Figure 5. The temporal step at the j[th] iteration is then determined assuming that the temperature in function of the time maintains the same slope and imposing to it a maximum variation ΔT_{MAX}:

$$\Delta t_j = \frac{T'_j}{m_j} = \frac{T_{j-1} + \Delta T_{MAX}}{m_j} \qquad (10)$$

The iteration is repeated with a smaller Δt_j until the variation of the temperature is smaller than a user defined value. This procedure is applied to the curve of the average temperature of the units which have changed temperature until the current

iteration[1]. This choice is a compromise between choosing the unit where the quench is initiated and the coldest one, where the increase of the temperature is maximum. The curve of the first unit in quench can't be used, because after the first temporal steps the increase of the temperature of the other colder units would be higher and it would be out of control adopting this strategy. The ideal choice would be to use the temperature curve of the unit which has, at any iteration, the maximum variation of temperature. However this approach would be inefficient, because the temporal step would be determined by the coldest units also if far away from the starting point of the quench and then less influent to determine the hot spot temperature.

A.5. Material properties

The material properties involved in the heat balance equation are averaged and weighted over the cross section of the unit in the x-y plane.

In the case of the product of the specific heat and the density the equivalent quantity is calculated simply making a weighted cross section average as:

$$\gamma C_S = \sum_{i=materials} \frac{A_i}{A_{TOT}} \gamma_i C_{S\,i} \qquad (11)$$

where A_{TOT} is the total surface of the unit in the x-y plane, A_i is the section, γ_i the density and C_{Si} the specific heat of the ith material of the unit. The specific heat of the copper can be written as the sum of the contribution of the lattice, which scales as T^3, dominant for low temperatures, and the ones of the free electrons which goes as T [4]:

$$C_{S\,Cu} = 7.44 \cdot 10^{-4} \cdot T^3 + 1.1 \cdot 10^{-2} \cdot T \qquad (12)$$

The specific heat of Nb_3Sn in the superconducting state is given by [4]:

$$C_{S\,Nb_3Sn} = 4.2 \cdot 10^{-3} \cdot T^3 + 0.183 \cdot T \qquad (13)$$

The specific heat in the normal state has been determined by a fit on the measured values [4], and the used parameterization is:

$$C_{S\,Nb_3Sn} = \begin{cases} 1.37 \cdot 10^{-3} \cdot T^3 + 0.28 \cdot T, & T < 32\,K \\ 2.7 \cdot 10^{-5} \cdot T^3 - 1.8 \cdot 10^{-2} \cdot T^2 + 4.08 \cdot T - 58.8, & T \geq 32\,K \end{cases} \qquad (14)$$

[1] This curve is monotone and then it can be used at this scope because the treatment neglects the convection with the helium bath.

For a G10 insulation the specific heat has the expression [5]:

$$\log(C_{sG10}) = a + b\cdot\log T + c\cdot(\log T)^2 + d\cdot(\log T)^3 + e\cdot(\log T)^4 + f\cdot(\log T)^5 + \ldots$$
$$g\cdot(\log T)^6 + h\cdot(\log T)^7 + i\cdot(\log T)^8$$

The coefficients are shown in Table 1.

Concerning the equivalent thermal conductivity in the longitudinal or in the transverse dimensions the models indicated in Figure 6 have been used.

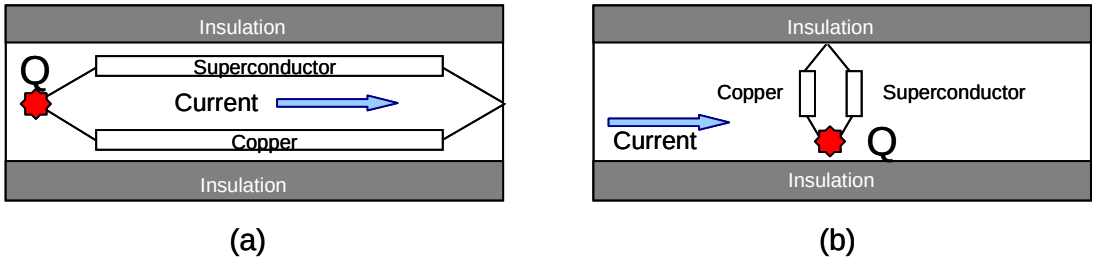

Figure 6. Longitudinal (a) and transverse (b) equivalent thermal conductivity in a unit. Q indicates a point where the quench is supposed to start.

The contribution to the conductivity of the insulation in the longitudinal dimension is negligible with respect the ones of the copper and the superconductor, then it has been excluded from the calculation. The equivalent conductivity has been determined considering the copper and the superconductor in parallel. Being $A_{TOT\,COND}$ the section of the unit excluding the insulation, and k_i the thermal conductivity of the copper and of the superconductor, the equivalent conductivity in the longitudinal dimension is then calculated as:

$$k_l = \sum_{i=Cu,SC} \frac{A_i}{A_{TOT\,COND}} k_i \qquad (15)$$

Along the transverse dimensions also the contribution of the insulation has to be taken into consideration. The equivalent thermal conductivity in the transverse dimension is calculated considering the copper and the superconductor in parallel, the insulation in series to them and weighting over the cross section of each material, i.e.:

$$\frac{1}{k_t} = \frac{A_{Cu}/A_{TOT} + A_{SC}/A_{TOT}}{k_{t\,COND}} + \frac{A_{Ins}}{A_{TOT}}\frac{1}{k_{Ins}} \qquad (16)$$

where k_{tCOND} is given by:

$$k_{t\,COND} = \sum_{i=Cu,SC} \frac{A_i}{A_{TOT\,COND}} k_i \qquad (17)$$

The thermal conductivity of the copper and of Nb_3Sn in the longitudinal and in transverse dimension are the same. In particular k_{Cu} can be found from the expression [5]:

$$\log_{10}(k_{Cu}) = \frac{a + c \cdot T^{0.5} + e \cdot T + g \cdot T^{1.5} + i \cdot T^2}{1 + b \cdot T^{0.5} + d \cdot T + f \cdot T^{1.5} + h \cdot T^2} \tag{18}$$

where the coefficients are indicated in Table 1 and for the Nb_3Sn in the normal state it is calculated as [4]:

$$k_{Nb_3Sn} = \min\left(1 \cdot 10^{-3} \cdot T^2, 3.2 \cdot 10^{-4} \cdot T^2 - 5.8 \cdot 10^{-4}\right) \tag{19}$$

whereas in the superconducting state as [6]:

$$k_{Nb_3Sn} = \begin{cases} 5.45 \cdot 10^{-3} \cdot T^3 - 5.34 \cdot 10^{-2} \cdot T^2 + 0.187 \cdot T - 0.21, & T < 6.5K \\ 14 \cdot \exp(-1.6 \cdot 18.3/T), & T \geq 6.5K \end{cases} \tag{20}$$

The longitudinal and the transverse thermal conductivity of the insulation can be written as [5]:

$$\log(k_{G10}) = a + b \cdot \log T + c \cdot (\log T)^2 + d \cdot (\log T)^3 + e \cdot (\log T)^4 + f \cdot (\log T)^5 + \ldots$$
$$g \cdot (\log T)^6 + h \cdot (\log T)^7 + i \cdot (\log T)^8$$

where the coefficients are indicated in Table 1.

	k_{Cu} W/(mK)	C_{sG10}	k_{LG10}	k_{TG10}
a	2.2154	-2.4083	-2.64827	-4.1236
b	-4.7461×10^{-1}	7.6606	8.80228	13.788
c	-8.8068×10^{-1}	-8.2982	-24.8998	-26.068
d	1.3871x10	7.3301	41.1625	26.272
e	2.9505×10^{-1}	-4.2386	-39.8754	-14.663
f	-2.0430×10^{-2}	1.4294	23.1778	4.4954
g	-4.8310×10^{-2}	-0.24396	-7.95635	-0.6905
h	1.2810×10^{-3}	-0.015236	1.48806	0.0397
i	3.207×10^{-3}	0	-0.11701	0

Table 1. Coefficient of the material properties.

In the case the unit is in quench also the equivalent resistance is calculated considering in parallel the copper and the superconductor:

$$\frac{1}{R} = \frac{A_{Cu} / A_{COND}}{R_{Cu}} + \frac{A_{SC} / A_{COND}}{R_{SC}} \tag{21}$$

The resistivity of the superconductor becomes negligible with respect to the one of the copper after some iteration the quench is started in the unit. The resistivity of the copper is expressed as [4]:

$$\rho = \max\left(\frac{1.67\cdot 10^{-8}}{RRR} + 0.5\cdot 10^{-10}\cdot B, 5.9\cdot 10^{-11}\cdot T - 10^{-9}\right) \tag{22}$$

where RRR is the residual resistivity ratio.

To determine the properties of the material the magnetic field of each unit is calculated assuming that it depends linearly from the coordinate x. The parameters of this line are determined as:

$$\begin{cases} m = \dfrac{B_{MAX} - B_{MIN}}{R_{EXT} - R_{INT}} \\ q = B_{MAX} \end{cases} \tag{23}$$

being R_{INT} and R_{EXT} the internal and the external radius of the coil, B_{MIN} and B_{MAX} the minimum and the maximum field at the half height the coil respectively. The coefficients of (21) are rescaled with respect to the ones at the start of the quench, $m\left(I_{Input}\right)$ and $q\left(I_{Input}\right)$, according to:

$$\begin{cases} m(I) = \dfrac{m\left(I_{Input}\right)}{I_{Input}} I(t_j) \\ q(I) = \dfrac{q\left(I_{Input}\right)}{I_{Input}} I(t_j) \end{cases} \tag{24}$$

where $I(t_j)$ is the current at the time t_j. For each temporal step it is determined by solving the system of equations which describes the protection system, as described in the next section.

A.6. Solution of the circuit

The scheme of the simulated protection system is shown in Figure 7.

When a quench is detected the switch A closes the circuit onto the resistance R_{EXT}. Because of the inductances of the coils, the current doesn't drop to zero instantaneously, but it continues to circulate until the stored energy is dissipated according to a RL discharge with an equivalent resistance variable because of the time dependence of R_Q.

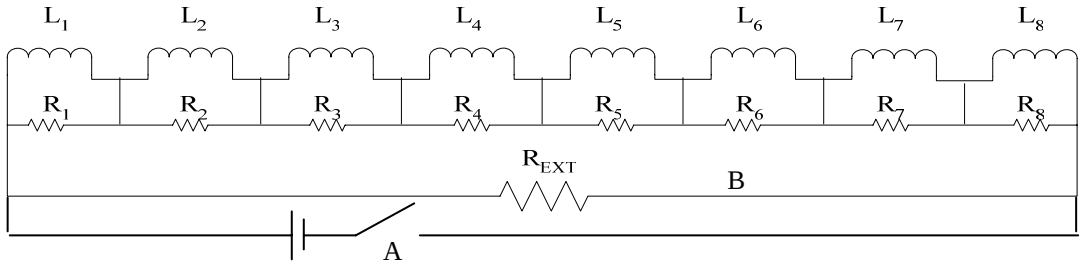

Figure 7. Scheme of the system of protection of the undulator. After the quench is detected the switch A opens isolating the power supply and B closes the circuit on the resistance R_{EXT}. The mutual inductances M_{ij} are not indicated for simplicity.

The other shunt resistances R_i in parallel to each coil are used both to deviate the current from the coil in quench and to dissipate part of the stored energy. Their value has to be kept small to allow the current flowing into them as soon as possible after the switch A is opened, but, at the same time, they can't be too small to avoid a phenomenon of current loop and that the discharge is too slow. The value of R_{EXT} should be high to minimize the time of the discharge of the circuit, but at the same time it is limited by the maximum tension sustainable by the system. The code considers the coupling of each coil with the one symmetric with respect to the mid-plane, because the other couplings are negligible in cases of the magnets designed during this thesis, by introducing the mutual inductances indicated in Figure 7.

Let I_i and I_{EXT} the currents which circulate in each coil and in R_{EXT} respectively. In the hypothesis that a quench starts in the coil 1, the circuit can be described by the system of equations:

$$\begin{cases} L_1 \dot{I}_1 + M_{12} \dot{I}_2 - R_1 (I_{EXT} - I_1) + R_Q I_1 = 0 \\ L_2 \dot{I}_2 + M_{12} \dot{I}_1 - R_2 (I_{EXT} - I_2) = 0 \\ L_i \dot{I}_i + M_{ij} \dot{I}_j - R_i (I_{EXT} - I_i) = 0 \quad i = 2k+1; \quad j = i+1; \quad k = 1,2,3 \\ R_{EXT} I_{EXT} + \sum_{s=1,2,...8} R_s I_s = 0 \end{cases} \tag{25}$$

where $\dot{I}$ is the array of the time derivative of the currents $\dot{I}_i$. The system written in matricial form, substituted I_{EXT} determined from the last equation, becomes:

$$M \dot{I} = A I \tag{26}$$

where M is the matrix of the inductances and the generic element of A is equal to:

$$A_{i,j} = \frac{R_i R_j}{\sum_{k=1}^{8} R_k + R_{EXT}} - \delta_{ij} R_j - \delta_{1j} R_Q \qquad i, j = 1,2,...8 \tag{27}$$

The matricial equation is solved inverting the matrix M to determine $\dot{I}$:

$$\dot{I} = M^{-1} A I \equiv \tilde{M} I \tag{28}$$

and the current at time t_j in function of the one at the time t_{j-1} is given by:

$$I_{t_j} = I_{t_{j-1}} e^{\tilde{M} \Delta t} \tag{29}$$

where the exponential of the matrix $\tilde{M}$ is determined cutting the convergent power expansion at the second order. The currents in the shunt resistances, I_{Ri}, are finally determined imposing the nodes equations:

$$I_{Ri} = I_{EXT} - I_i \quad i = 1,2,...8$$

At each temporal step this calculation is repeated and the resulted currents are used to determine the tensions, the energies in each element of the circuit and to calculate the current density and the quench resistance to be used in the successive iteration.

APPENDIX B

REDUCTION OF THE INTEGRATED ODD MULTIPOLES IN PERIODIC MAGNETS

In periodic magnets, like undulators and wigglers, the integrated even multipoles cancel along each period, whereas the odd ones sum from a pole to the next one. A possible approach to reduce these sources of perturbation for the beam dynamics is to add some jaws at the extremities of the magnets. This solution can decrease a particular order integrated multipole, but it may cause an increase of another order multipole.

A reduction of all the odd integrated multipoles can be obtained by shaping the poles to follow the beam trajectory. In this configuration the odd multipoles would be made null in each transversal section in the poles regions, but the regions between the poles would still give a net integrated multipole.

The new method presented here uses the contributions to the integrals of the odd multipoles of the poles regions to compensate the ones of the regions between the poles. It will be shown that this condition can be achieved by moving the axis of the magnetic field. After the method is described and discussed, its application and optimization on a real magnet are presented.

B.1. Introduction

Integrated multipoles along the beam trajectory must be made as small as possible, because they cause perturbations on the optics of particle accelerators. In this appendix the case of magnets with periodic structure, like undulators and wigglers, is studied.

In this kind of magnets only the integrated odd multipoles in US notation (quadrupole, octupole, dodecapole, …) must be considered, because the contributions of the even ones (dipole, sextuple, decapole, …) are equal in magnitude and opposite in sign from a pole to the next one, so that their integral along each period is null.

A possible approach to minimize a specific integrated multipole consists in adding at the extremities of the magnet some jaws to compensate these terms [1]. A method to minimize all the odd integrated multipoles may consist in shaping the poles to reduce the odd multipoles in each transversal section along the beam trajectory. This can be done trying to improve the uniformity of the field in the transverse dimension or designing the poles to follow the beam trajectory. However in these cases the multipoles in the regions between the poles still give contributions to the integrals which, consequently, can't be made null.

The approach presented in this appendix is to modify the shape of the poles to compensate the contributions to the integrated odd multipoles from the regions between the poles with the ones from the poles regions.

In section B.2. it will be shown that the odd multipoles along the trajectory can be written as the sum of odd multipoles with respect to the magnetic axis (null for the left-right symmetry of the magnet) plus even multipoles multiplied by odd powers of the transverse coordinate of the trajectory with respect to the same axis. The approach, described in section B.2.2. , consists in moving the axis of the magnetic field to change the sign of the transverse coordinate of the beam trajectory in each semiperiod, in such a way that also the contributions containing the even multipoles cancel. By this way all the odd integrated multipoles are reduced and a multipole of a specific order, determined by the particular problem requests, can be made null.

This method has been applied to the wiggler of DAΦNE main ring to make null the integrated octupole with respect to the beam trajectory. The optimization and the calculated results, compared with the present situation, are presented in section B.3. .

B.2. The general method

In section B.2.1. the multipoles with respect to the beam trajectory will be expressed as a function of the ones with respect to the magnetic axis. This expression will be used to show that in a periodic magnet the integrals of the even integrated multipoles with respect to the beam trajectory cancel in the whole wiggler. In section B.2.2. the same expression will be used to show how to reduce the integrated odd multipoles by moving the magnetic axis.

B.2.1. Integrated multipoles in a periodic magnets

Let z the geometric axis of the wiggler, y the vertical transverse dimension and x the other transversal coordinate. The vertical component of the magnetic field B_y at each z can be expanded around the horizontal coordinate of the wiggling trajectory $x_{TR}(z) \equiv x_{TR}$ as:

$$B_y(z, x_{TR}) = \sum_{n=0}^{\infty} \frac{1}{n!} \cdot \left. \frac{\partial^n B_y(z,x)}{\partial x^n} \right|_{x=x_{TR}} \cdot (x - x_{TR})^n \qquad (1)$$

where the derivatives are calculated in x_{TR}. The effect of the k-term on the dynamics of the beam is determined by the integral I_k, defined as:

$$I_k \equiv \frac{1}{k!} \int_{Wiggler} \left. \frac{\partial^k B_y(z,x)}{\partial x^k} \right|_{x=x_{TR}} \cdot dz \quad k = 0,1,... \qquad (2)$$

To better understand the model described in this appendix, it is more convenient to write the integrand of eq. (2) in function of the multipoles calculated with respect to the axis of the magnetic field.

In each section for each z the magnetic field around any point of coordinate (x, y, z) can be expressed in the US notation as:

$$B_y(\underline{z}) = \sum_{n=0}^{\infty} (B_n + i \cdot A_n) \cdot \left(\frac{\underline{z}}{R_{REF}} \right)^n \qquad (3)$$

where A_n and B_n are the skew and the normal multipoles respectively, R_{REF} is a radius of reference and the complex variable $\underline{z}$ is defined as:

$$\underline{z} = x + i \cdot y \qquad (4)$$

Each multipole B'_n and A'_n calculated in a system of reference displaced from the one centered in the axis of the magnetic field can be written as:

$$B_n'+A_n'=\sum_{k=n}^{\infty}\left[(B_k+i\cdot A_k)\cdot\left(\frac{k!}{n!\cdot(k-n)!}\right)^{n-1}\left(\frac{x_0+i\cdot y_0}{R_{REF}}\right)^{k-n}\right] \tag{5}$$

where B_k and A_k are calculated with respect to the axis of the field and x_0 and y_0 are the displacements of the system of reference in the horizontal and in the vertical dimension respectively.

For each z any normal multipole, B'_n, calculated with respect to the trajectory, which represents the system of reference displaced of $x_0 = x_{TR}$ and $y_0 = 0$ with respect to the axis of the magnetic field, can be written as:

$$B'_n=\sum_{k=n}^{\infty}B_k\,\frac{k!}{n!\cdot(k-n)!}\cdot\left(\frac{x_{TR}}{R_{REF}}\right)^{k-n} \tag{6}$$

From eq. (6) the even term of the expansion of the field with respect to the beam trajectory, B'_{2j}, can be written as:

$$B'_{2j}=c_{2j}B_{2j}+c_{2j+1}B_{2j+1}\cdot x_T+c_{2j+2}B_{2j+2}\cdot {x_T}^2+c_{2j+3}B_{2j+3}\cdot {x_T}^3\ldots \tag{7}$$

where $c_{f(j)}$ are positive constants. From eq. (7) it is evident that these integrated multipoles cancel themselves in each period of the wiggler. The terms which contain even multipoles with respect to the axis, in fact, change sign from a pole to the next one, so that the sum of their contribution to the integral is null in each period and the odd multipoles terms are zero because of the left-right symmetry of the magnet.

The odd multipoles with respect to the beam trajectory B'_{2j+1} can be written from eq. (6) as:

$$B'_{2j+1}=c_{2j+1}B_{2j+1}+c_{2j+2}B_{2j+2}\cdot x_T+c_{2j+3}B_{2j+3}\cdot {x_T}^2+c_{2j+4}B_{2j+4}\cdot {x_T}^3\ldots \tag{8}$$

where $c_{f(j)}$ are positive constants. The contributions from the odd multipoles with respect to the axis are still null, but the others do not, because both the even multipoles with respect to the axis and x_{TR} change sign from a pole to the next one, so that their product sum from a pole to the next one.

In conclusion in undulators and wigglers the only integrated multipoles which remain after a period are the odd ones.

B.2.2. Movement of the axis of the magnetic field

In Figure 1 the beam trajectory in a semiperiod of the magnet in the z-x plane is schematically represented. Without any shaping of the pole the geometric and the magnetic axis of the magnet, indicated as G.A. M.A. respectively in Figure 1, coincide.

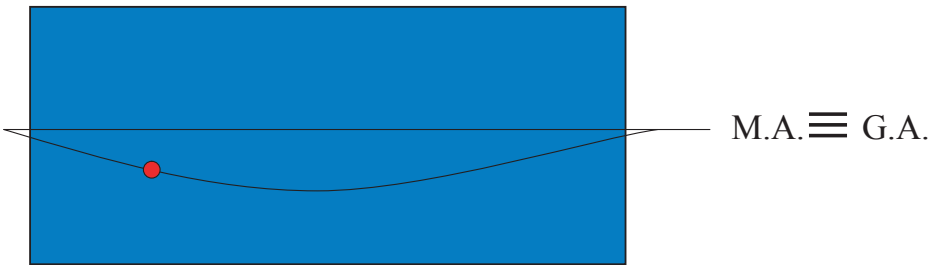

Figure 1. Beam trajectory in a semiperiod of the magnet. Without any shaping of the pole the geometric (G.A.) and the magnetic (M.A.) axis of the magnet coincide.

In this configuration for the whole semiperiod the beam is at the same side with respect to the magnetic axis, so that the sign of x_{TR} doesn't change.

Consider now a configuration where the pole is modified in such a way that the beam trajectory changes side with respect to the magnetic axis, as sketched in Figure 2 and in Figure 3.

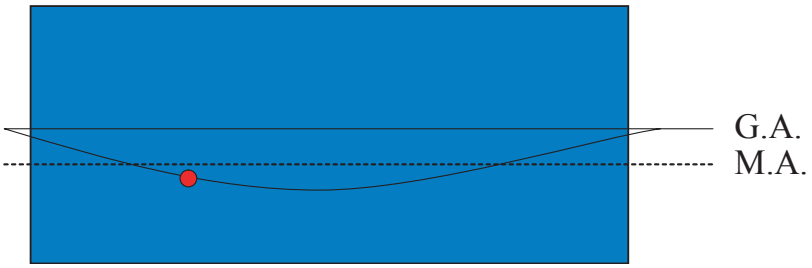

Figure 2. Beam trajectory in a semiperiod of the magnet. The geometric (G.A.) and magnetic (M.A.) axis of the wiggler are separated. In this case the trajectory of the beam is at the right of the magnetic field axis.

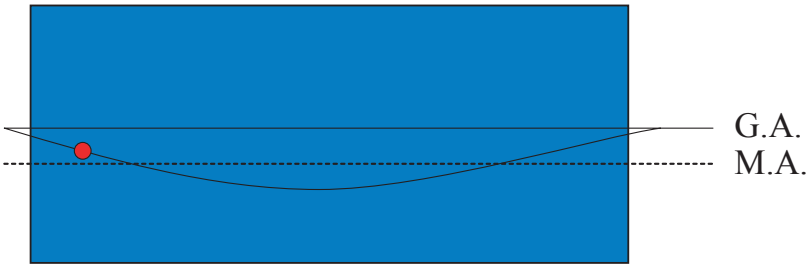

Figure 3. Beam trajectory in a semiperiod of the magnet. The geometric (G.A.) and magnetic (M.A.) axis of the wiggler are separated. In this case the trajectory of the beam is at the left of the magnetic field axis.

In this configuration in each semiperiod the contributions of the terms which contain odd power of x_{TR} in eq. (8) can be changed of sign. By moving the axis it is then possible to reduce all the odd integrated multipoles in a semiperiod and, conveniently choosing the axis, make null one particular order determined by the specific requests of the problem.

This method has been applied to the wiggler in the main ring of DAΦNE (INFN-Frascati) to make null the integrated octupole.

B.3. Application to the wiggler in the main ring of DAΦNE

In the main ring of DAΦNE (Frascati, INFN Laboratory) eight normal conducting wigglers have been installed to reduce the damping time. Since their first operation these magnets were sources of non-linearity for the dynamics of the beam [2], because of the large excursion of the particles with respect to the axis of the wigglers (about 1.3 cm). The specifications of the magnets are summarized in Table 1.

	Full poles	Halves poles
Number of poles	5	2
Current (A)	693	564
Maximum magnetic field (T)	~1.8	~1.5
Period (mm)	640	
Gap (mm)	37	
Pole width (mm)	140	
Particles beam	electrons and positrons	
Beam energy (MeV)	511	

Table 1. Wigglers specifications and most important circulating beams characteristics in DAΦNE.

To reduce the integrated multipoles several interventions oriented to improve the uniformity of the magnetic field in the transverse dimension have been implemented, but, at present, a not negligible parabolic tune shift with respect to the horizontal displacement of the beam, due to the integrated octupole with respect to the beam trajectory, still persists [3].

The approach described in this appendix has been applied to these wigglers to make null this integrated multipole.

B.3.1. Analysis of the present situation

In Figure 4 the scheme of one of the wigglers in the plane (z, x) is shown.

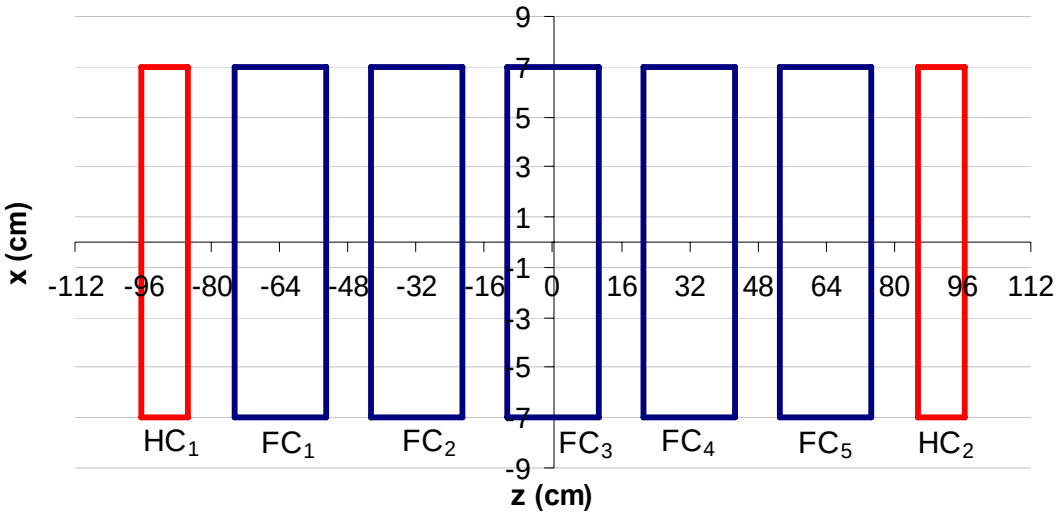

Figure 4. Scheme of the wigglers in the z-x plane.

The vertical component of the magnetic field, $B_y(z, x_{TR})$, given by M. Preger, has been measured in the mid-plane at steps of 1 cm in z from -1.35 m to 1.35 m with respect to the center of the magnet and with the same step in x for the whole width of the poles.

For each z the vertical component of the magnetic field has been fitted in the requested range of field uniformity of ±3 cm around the beam trajectory by a fourth order polynomial:

$$B_y(x - x_{TR}) = b_0 + b_1 \cdot (x - x_{TR}) + b_2 \cdot (x - x_{TR})^2 + b_3 \cdot (x - x_{TR})^3 + b_4 \cdot (x - x_{TR})^4 \qquad (9)$$

The integrals defined in eq. (2) have been calculated both for the central semiperiod, i.e. from z = -16 cm to z = +16 cm with respect to the center of the wiggler, and for the whole magnet. The results are indicated in Table 2.

	I_0 (T.m)	I_1 (T)	I_2 (T/m)	I_3 (T/m^2)	I_4 (T/m^3)
±16 cm	-0.40	-0.09	0.80	-26.5	1448.7
Whole	**0.00**	**-0.09**	**-3.35**	**-139.7**	**1772.2**

Table 2. Integrated coefficients of the transversal expansion calculated with respect to the beam trajectory in the central semiperiod and in the whole wiggler.

In particular in Figure 5 the third order term of the transverse expansion in function of z is plotted.

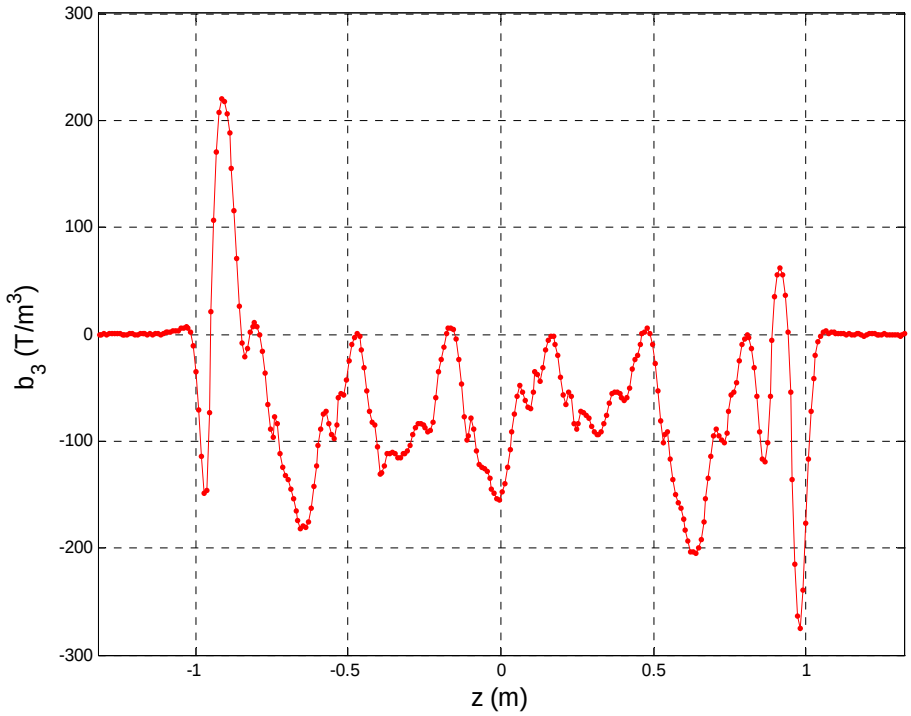

Figure 5. Third order term of the transversal expansion calculated with respect to the beam trajectory in function of z .

The anomalous behavior of the second and the fourth order terms, which don't cancel along the whole magnet, and the asymmetry of b_3 with respect to the center of the wiggler are due to a modification made only on one terminal pole of the wiggler to improve the dynamic aperture of the ring [3].

In the next section the modification of the wiggler and the obtained integrated multipoles will be compared to the values of Table 2.

B.3.2. The modification of the wiggler

After a model of the original configuration of the wiggler has been used to validate the magnetic model, the process of optimization of the modification of the wiggler has been done. It has been done in three steps:

1. Optimization of the position of the magnetic field axis to minimize the integrated octupole
2. Optimization of shims to improve the field uniformity in transverse dimension to reduce the dependence of the solution on the misalignment of the beam trajectory and the wiggler

3. Re-optimization of the optimal position of the magnetic field axis modified by the presence of the shims

Several ways are possible to move the magnetic field axis. In case of superconducting magnets, this condition could be obtained by moving the coils. In the case of a normal conducting wiggler, like the ones of DAΦNE, the modification has to be done on the iron poles.

To have null even multipoles with respect to the beam trajectory integrated in the whole wiggler it is necessary that the even multipoles calculated with respect to the magnetic axis are equal in modulus and opposite in sign from a pole to the next one and that the odd ones with respect to the same axis are still null after the modification.

To obtain the first condition it is necessary to modify the shape of the poles to have a magnetic axis which is displaced with respect to the wiggler geometrical axis of the average horizontal beam trajectory in the pole. The sketch of the cut is shown in Figure 6.

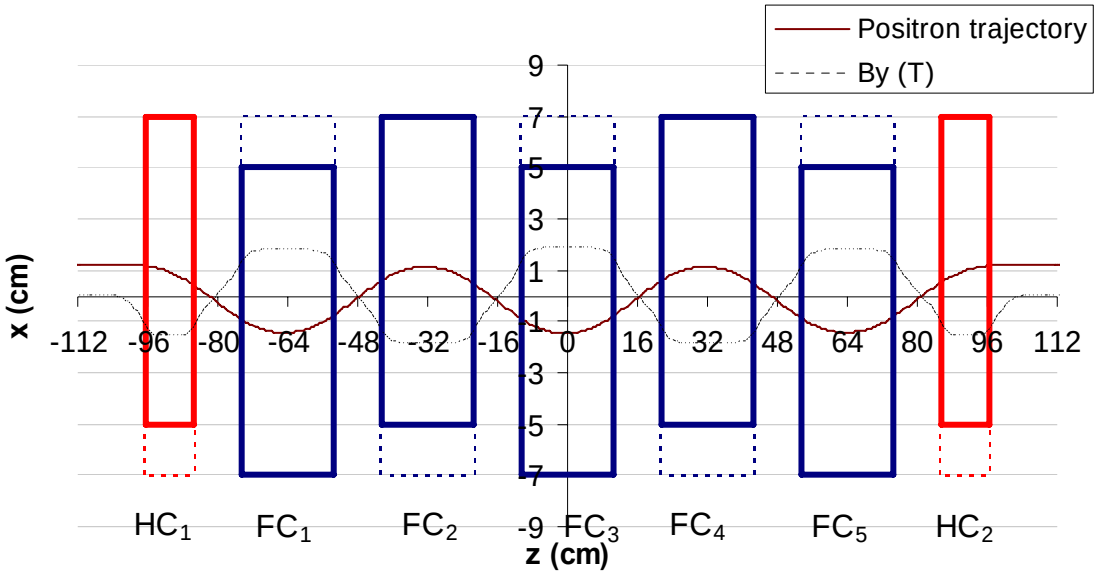

Figure 6. Modified wiggler. The configuration of the poles without any shaping of the pole (dashed lines) and with the cuts (solid lines) are indicated.

All the 3D magnetic models have been calculated with the code OPERA [4]. A preliminary model of the complete wiggler without any shaping of the poles, shown in Figure 7, has been used to calculate the beam trajectory and to validate the magnetic model by comparing the results of the multipolar analysis with the experimental measurements.

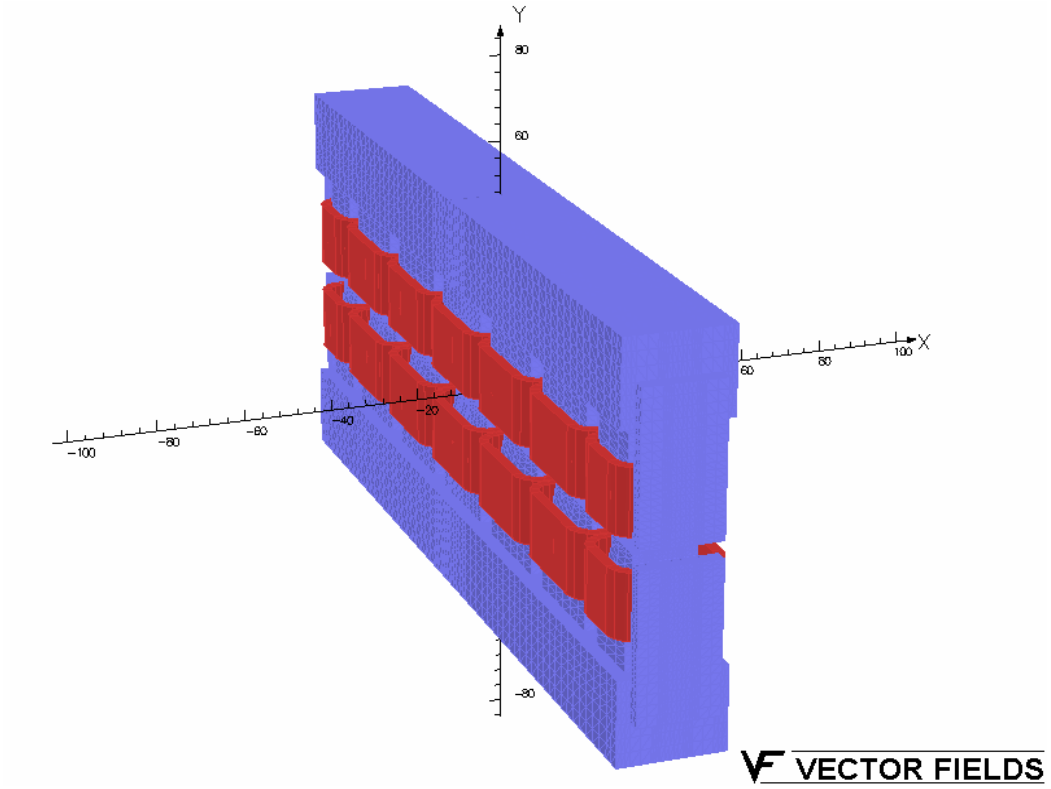

Figure 7. 3D model of the complete wiggler of DAΦNE without any shaping of the poles. Dimensions are in cm. For the symmetry of the wiggler only 1/8 of the magnet has been simulated.

The average trajectory in the pole region has been chosen as the axis with respect to which cut the poles of the wiggler. The average trajectory in each pole is shown in Table 3.

	HC_1	FC_1	FC_2	FC_3
Average beam trajectory (cm)	0.95	-1.01	1.04	-0.97

Table 3. Average beam trajectory in each pole of the wiggler.

To have a unique axis it has then been decided to cut the poles around ±1 cm with respect to the geometric axis of the wiggler. In Figure 8 the shape of the poles in the z-x plane where the average beam trajectory is at negative x, like FC_1, and positive, like FC_2, after the modification is shown.

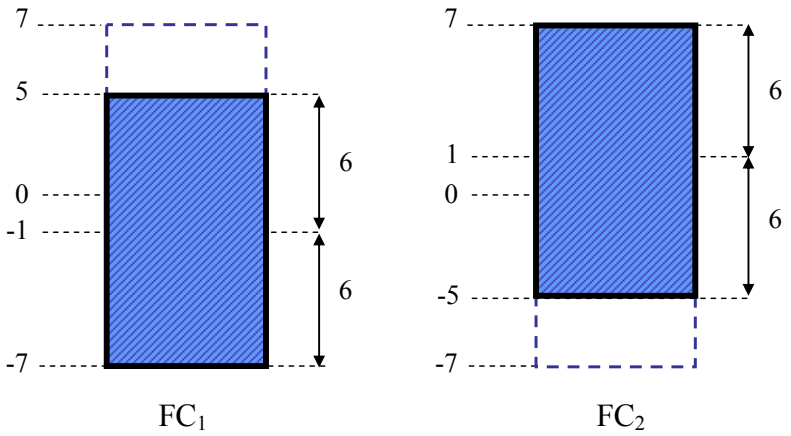

Figure 8. Modified poles. Shape in the z-x plane of the cut of the poles along the average beam trajectory for FC_1, FC_3 and FC_5 and for FC_2, FC_4, HC_1 and HC_2. The shape of the poles without any modification is also indicated (dashed line).

To obtain the condition of null odd multipoles with respect to the magnetic axis the shape of the poles in the plane x-y has been modified in such a way to maintain the left-right symmetric configuration with respect to this axis. The shape of the cut has been determined to have the maximum width of the pole close to the mid-plane to limit the pole saturation and therefore avoid the field reduction. In Figure 9 a section of the equivalent model of the pole in this plane before any modification is shown.

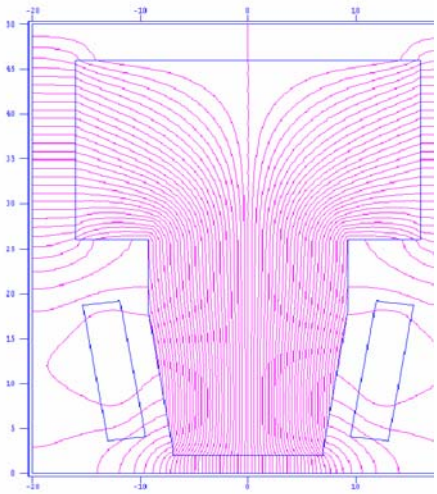

Figure 9. Section of the equivalent model of the pole in the plane (x, y) before any modification.

In Figure 10 the shape of the poles after the modification is shown.

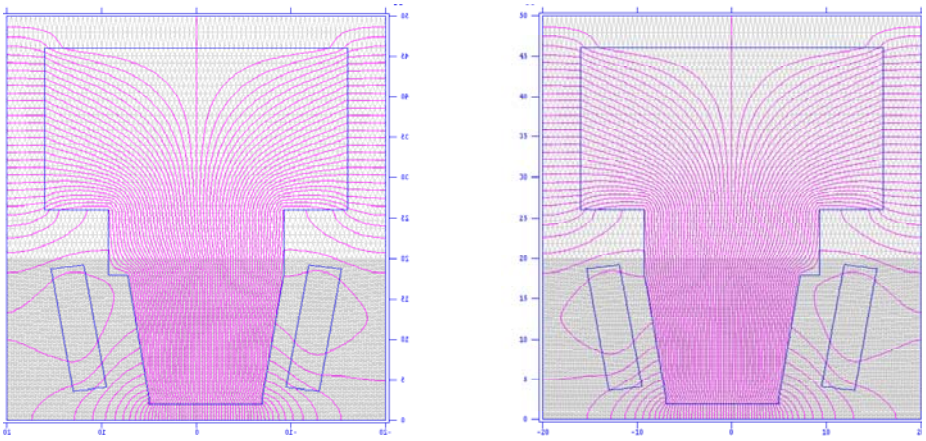

Figure 10. Section of the equivalent model of the pole in the plane x-y after the modification.

A 3D magnetic model of the complete wiggler with the modified poles should be done, but the running time of the simulation would be very long. This because to have a meaningful fit of the magnetic field for the multipolar analysis it is necessary to have a very high number of nodes, and moreover, to simulate 1/4 of the entire wiggler with respect to the 1/8 of the previous model, due to the asymmetry introduced with respect to the plane (y, z). For these reasons an approximated short model of only the central full pole (FC_3) and half of the two closest full ones (FC_2 and FC_4), shown in Figure 11, has been used to make a preliminary optimization, neglecting the effect of the the halves poles. After a preliminary optimization, the model of the complete wiggler to check the results has been done.

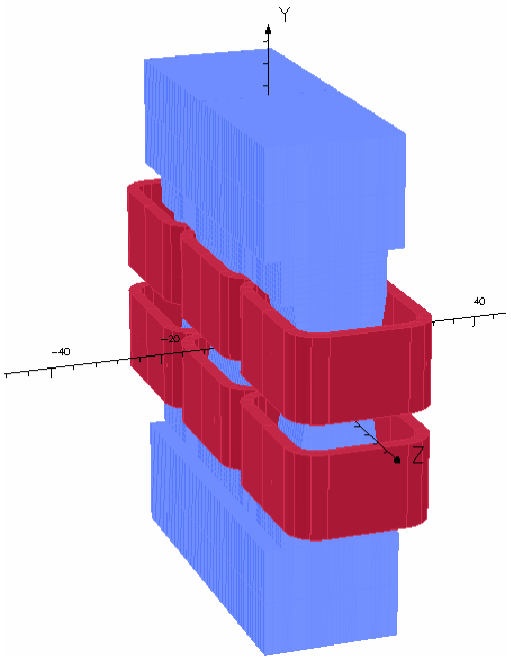

Figure 11. Model of the central full and the half of the two closest ones. Dimensions are in cm.

In Figure 12 the section of this model in the z-x plane is shown.

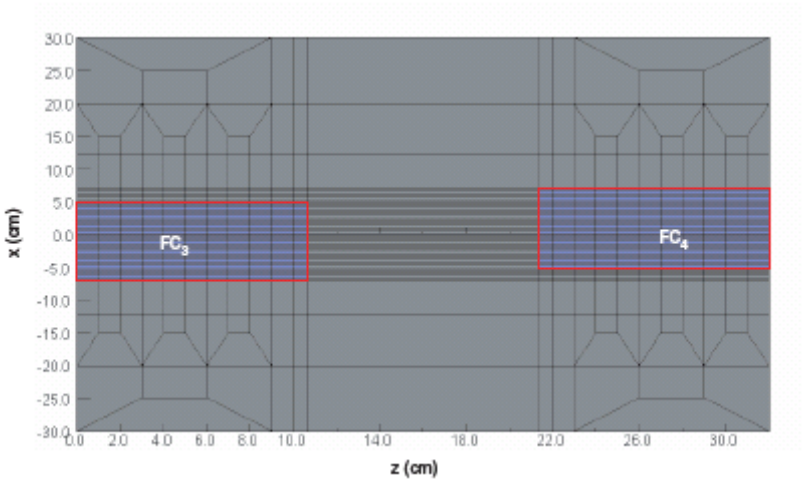

Figure 12. Section in the plane z-x of the model for the optimization. The steps in the region of the poles are of 1 cm in z and 0.4 cm in x. The structure of trapezes from x = ±12.25 cm to x = ±30 cm is to have a high number of nodes in the region of the fit without unnecessarily increasing the ones close to the bounding rectangle of the model.

The analysis of the map of the magnetic field has been performed fitting for each z the vertical component of the field by the fourth order polynomial of eq. (9) in the range of ±3 cm around the beam trajectory and the integrals defined by eq. (2) have been calculated in the central semiperiod (from z = -16 cm to z = +16 cm). The results are shown in Table 4.

	I_0 (T.m)	I_1 (T)	I_2 (T/m)	I_3 (T/m^2)	I_4 (T/m^3)
Modified	0.43	-0.05	-7.62	-1.44	-3141.6
Present	-0.40	-0.09	0.80	-26.5	1448.7

Table 4. Comparison of the integrals of the coefficients of the polynomial expansion of the vertical component of the magnetic field in the configuration with the modified poles and the wiggler in the present configuration calculated in the central semiperiod of the magnet (from z = -16 cm to z = 16 cm).

In particular in Figure 13 the third order coefficient of the polynomial expansion calculated with respect to the beam trajectory in function of z is plotted.

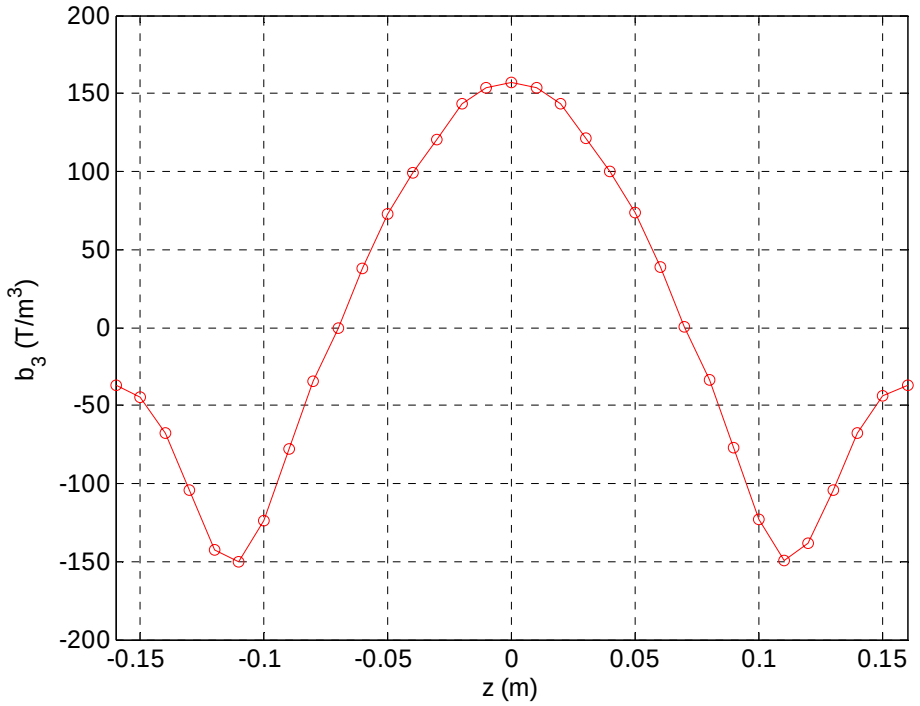

Figure 13. Third order coefficient of the transversal expansion of the vertical component of the magnetic field along the beam trajectory in a semiperiod in function of z .

This modification of the wiggler would allow reducing of a factor 20 the integrated octupole with respect to the present situation. A model of the complete magnet with the poles modified according to it has been simulated. The integrated coefficients of the transversal expansion in the central semiperiod and in the whole wiggler calculated from the complete wiggler model are indicated in Table 5.

	I_0 (T.m)	I_1 (T)	I_2 (T/m)	I_3 (T/m^2)	I_4 (T/m^3)
±16 cm	0.42	-0.05	-7.29	-2.62	-3290.8
Whole	**0.00**	**-0.24**	**-1.04**	**-9.50**	**-20.9**

Table 5. Integrated coefficients of the transversal field expansion calculated from the complete wiggler model with the modified poles in the central semiperiod and in the whole wiggler.

As can be seen from the comparison between Table 4 and Table 5 the integrals of b_3 is higher than the one calculated imposing the symmetry to make the short model of the wiggler. In any case the modification of the poles allows to improve of a factor 10 the present situation. This configuration has then been used for the second step of the optimization.

To verify the impact of a misalignment of the wiggler the analysis has been repeated in the case that the wiggler is shifted in the x direction of ±0.2 cm. The results for the central semiperiod are shown in Table 6.

Δx	I_0 (T.m)	I_1 (T)	I_2 (T/m)	I_3 (T/m^2)	I_4 (T/m^3)
Ideal	0.42	-0.05	-7.29	-2.62	-3290.8
+0.2 cm	0.43	-0.02	-7.34	24.79	-3313.2
-0.2 cm	0.42	-0.08	-7.37	-30.15	-3315.7

Table 6. Effect of a misalignment of the wiggler on the integrated coefficients of the field expansion along the beam trajectory calculated in the central semiperiod. The integrals in the case of ideal positioning of the wiggler are also reported for comparison.

This dependence, which destroys the effect of the modification of the poles in case of a displacement of 0.2 cm, has been reduced by shimming the poles to improve the field uniformity in the transverse horizontal dimension. These shims have to be symmetric with respect to the magnetic axis of the modified poles to maintain null the even integrated multipoles with respect to it and the beam trajectory, and less thick as possible to minimize the reduction of the mid-plane field because of the increase of the gap.

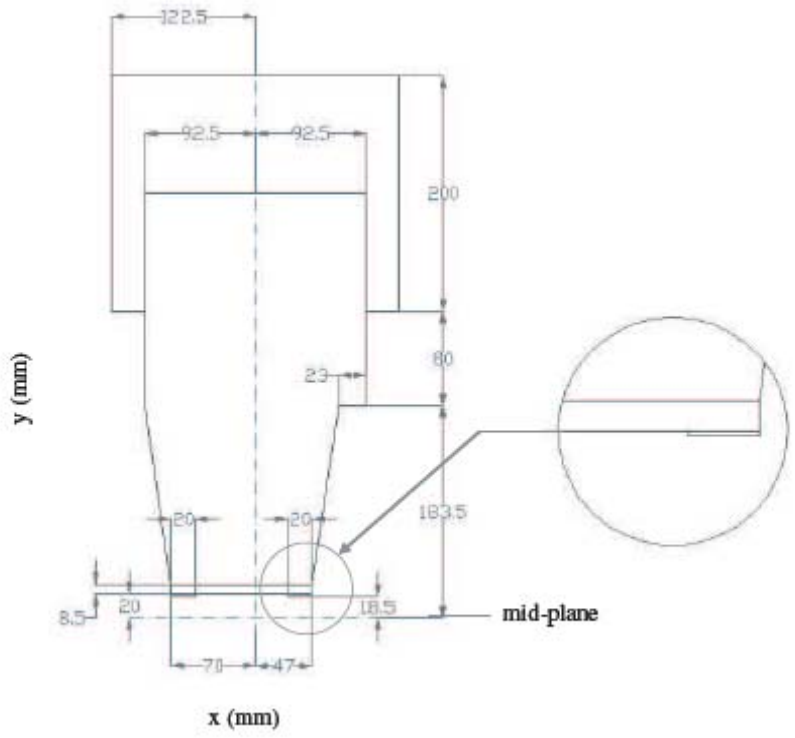

Figure 14. Section in the x-y plane of the poles of the wiggler with also the optimized shims.

The sections of the poles with the optimized shims in the z-x and the x-y plane are shown in Figure 14 and in Figure 15 respectively.

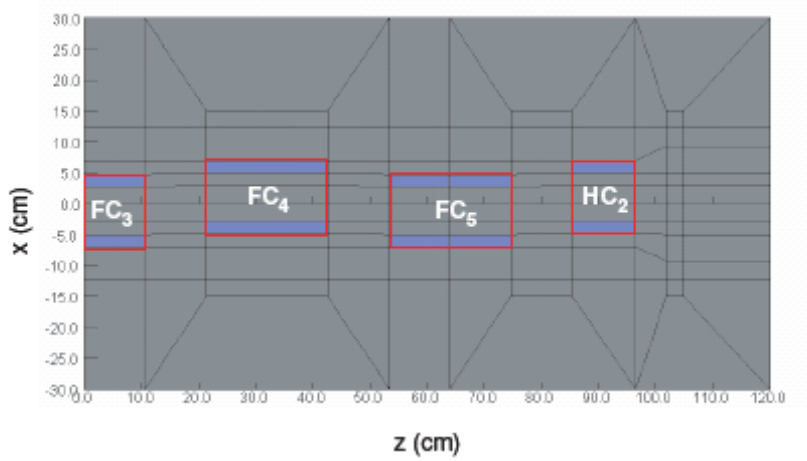

Figure 15. Section in the z-x plane of the poles of the wiggler with also the optimized shims.

The absolute value of the integrated coefficients in the central semiperiod of the field expansion with respect to the beam trajectory for several horizontal displacements of the wiggler in this configuration is shown in Table 7.

Δx	I_0 (T.m)	I_1 (T)	I_2 (T/m)	I_3 (T/m^2)	I_4 (T/m^3)
Nominal	0.42	-0.05	-7.50	-6.70	-596.9
-0.2 cm	0.42	-0.08	-7.57	-1.44	-670.7
+0.2 cm	0.42	-0.02	-7.43	-12.25	-578.1

Table 7. Integrated coefficients of the field expansion calculated in the central semiperiod in the configuration with the cut poles and the shims. The case of the wiggler aligned with the beam trajectory and the cases of a not perfect positioning of ±0.2 cm are shown.

In Figure 16 the absolute value of the integrated third order term of the field expansion in function of the horizontal displacement of the wiggler compared with the configuration without the shims is plotted.

It is evident that the dependence of the integrated third order term of the field expansion from the horizontal displacement of the wiggler is strongly reduced in this configuration, but the shims modify the value of the integral of b_3. It is then necessary to change the position of the magnetic axis to minimize I_3.

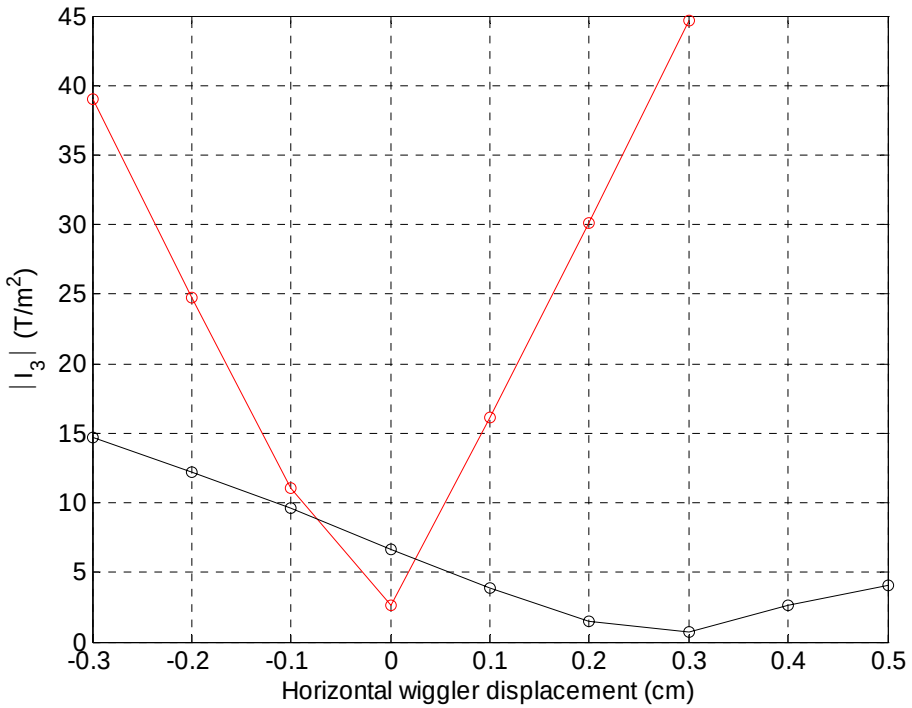

Figure 16. Absolute value of the integrated third order term of the transversal expansion of the vertical component of the magnetic field along the beam trajectory in the central semiperiod as a function of z .

The best position of the magnetic axis in the configuration with also the shims is for an axis moved of + (-) 0.15 cm for the poles as FC_1 (FC_2), as evident from Figure 17.

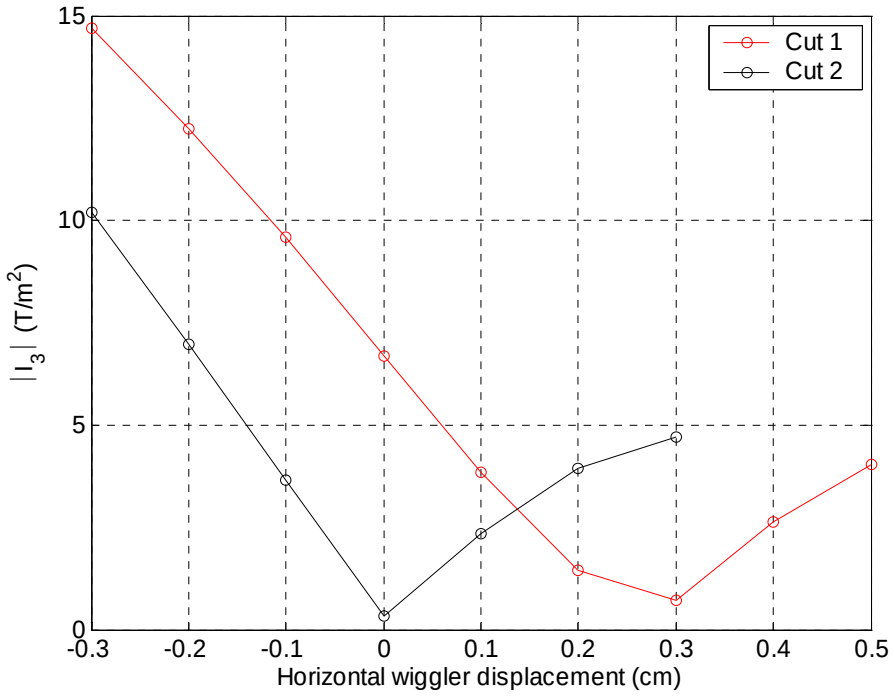

Figure 17. Absolute value of the integral of b_3 in the central semiperiod of the magnet in function of the horizontal displacement of the wiggler in the case of the cut around the average beam trajectory in the pole (Cut 1) and the one with the axis moved of ±0.15 cm with respect to it (Cut 2).

To have a further confirmation of the obtained results the analysis has been repeated increasing the number of subdivisions until the integrated multipoles become independent from it.

	I_0 (T.m)	I_1 (T)	I_2 (T/m)	I_3 (T/m^2)	I_4 (T/m^3)
-0.3 cm	0.42	-0.12	-7.87	6.30	708.9
-0.2 cm	0.42	-0.10	-7.96	5.03	816.6
-0.1 cm	0.42	-0.09	-8.00	2.86	867.7
Perfect	0.42	-0.07	-8.00	-0.29	921.8
0.1 cm	0.42	-0.06	-8.05	-3.89	958.5
0.2 cm	0.42	-0.04	-8.04	-7.67	962.5
0.3 cm	0.42	-0.02	-8.00	-11.45	948.2

Table 8. Integrated coefficients of the field expansion in the central semiperiod in the final configuration with a fine mesh.

From the simulations it results that the optimized configuration of the wiggler of DAΦNE would allow reducing by a factor of about 100 the integrated octupole for the central semiperiod. The contributions of each pole to those integrals and their values for the whole wiggler are indicated in Table 9.

	I_0 (T.m)	I_1 (T)	I_2 (T/m)	I_3 (T/m^2)	I_4 (T/m^3)
FC_3	0.42	-0.0.7	-8.04	-0.29	921.8
FC_4	-0.42	-0.07	8.07	-0.47	-904.1
FC_5	0.42	-0.06	-8.03	-0.16	919.0
HC_2	-0.21	-0.03	2.99	-2.79	-657.1
Whole	**0.00**	**-0.36**	**-1.67**	**-4.13**	**-327.1**

Table 9. Integrals of the coefficients of the field expansion for each pole and for the whole wiggler. The contributions are calculated only for the poles at positive z for the symmetry of the model. For FC_3 the contribution considered is from z = -16 cm to z = +16 cm.

The contributions of all the full poles to the integrals of b_3 are very similar to the one of the central full pole. The halves poles get worse the factor of reduction, which, in any case, remains of the same order (the integrated b_3 is reduced to the 3% of the value of the present configuration considering the whole wiggler with respect to the

1% considering the only central full pole). If necessary these terminal poles can be further modified like done for the full poles.
A modification of the wiggler at DAΦNE according to this optimization and the measurement should be done in 2007.

B.4. Conclusions

In this appendix a method to reduce the integrated odd multipoles and make null one of them has been presented. This approach has been applied to the wiggler of the main ring of DAΦNE to make null the integrated octupole. A straight cut of the poles around the average beam trajectory in the region of the poles allows reducing of about a factor 10 the integrated octupole, but this solution is strongly dependent from the positioning of the wiggler with respect to the trajectory. To improve the field uniformity around the beam trajectory and by this way reducing this dependence, a couple of shims has been added to the poles. They allowed reducing this dependence, but they also modified the best axis around which the poles should be cut. The last step was the re-optimization of this axis. The simulations indicate that in the final configuration the integrated octupole can be reduced to about the 1% with respect to the value of the present configuration considering only the full poles. This reduction becomes of the 3% of the present configuration taking into consideration the whole wiggler because of the terminal halves poles, which can be eventually modified analogously to what done for the full ones. A spare wiggler will be modified according to this model and, if the magnetic field map will be confirmed, the wigglers in the main ring of DAΦNE will be modified in 2007.

CONCLUSIONS

The beam profile measurement on the protons and the lead ions beams in LHC require an undulator which can switch the period from 140 mm for the lead ions to 280 mm for the protons beams.

The magnetic design of the undulator, based on a Nb_3Sn superconducting wire, in 2D and 3D has been completed. The field uniformity in the transverse dimension has been evaluated as well as the influence of the fringing field on the other circulating beam.

A superconducting wire manufactured by OI-ST has been selected. A calibration of the system to form the superconductor has been set-up and calibrated (comparison of the RRR and the critical current density measurements with the manufacturers specifications). Tests of flux jumping instability evidenced the presence of instability at current above 800 A. A modified undulator design with current below this value has then been made.

A dipole split coil has been designed and manufactured to test the performances of coils. This test did not put into evidence flux jumping or mechanical instabilities in the explored region of the magnetic field-current plane, although quenches occurred at current below the expected value. Several tests allowed to identify the heating of a point as the cause of this limitation. Another modification to the design, limiting the current below the maximum measured during the test, has been done.

A quench simulation code has been written and used to design the protection circuit and to evaluate the behavior of the magnet under quench.

A method for the reduction of the integrated octupole in the wigglers of the main ring of DAΦNE has been proposed (in collaboration with the Laboratori Nazionali di Frascati). The simulation indicates a reduction of the integrated octupole to the 3%

with respect to the actual value. This solution will be implemented in a spare wiggler, and, after field measurements confirmation, in the wigglers in the machine.

REFERENCES

Chapter 1

[1] Handbook on Synchrotron Radiation, Volume 1a, Ernst-Eckhard Koch, Ed., North Holland, 1983.

[2] *Characteristics of the radiation emitted by protons and antiprotons in an undulator,* J. Bosser, L. Burnod, R. Coisson, G. Ferioli, J. Mann and F. Meot*,* J. Phys. Lett. 45, L343–351 (1984).

[3] Classical Electrodynamics, 3rd edition (Wiley, New York-1998).

[4] Synchrotron radiation (production and properties), Philip John Duke, Oxford Science publication (2000).

[5] *Introduction to insertion devices*, K. Wille, Proc. European Accelerator School, Grenoble, CERN-98-04 (1998).

[6] *Insertion devices: undulators and wigglers*, R. P. Walker, Proc. European Accelerator School, Grenoble, CERN-98-04 (1998).

[7] *Characteristics of synchrotron radiation*, A. Hofmann, Proc. European Accelerator School, Grenoble, CERN-98-04 (1998).

[8] Internet site
http://public.web.cern.ch/Public/Content/Chapters/AboutCERN/CERNFuture/WhyLHC/WhyLHC-en.html

[9] *Wire Scanners for LHC*,J. Bosser and C. Bovet, LHC Project Note-108 (1997).

[10] *The luminescence profile monitor of the CERN SPS*, G. Burtin, J. Camas, G. Ferioli, R. Jung, J. Koopman, R. Perret, A. Variola and J. M. Vouillot, , CERN-SL-2000-031 BI, presented at European Particle Accelerator Conf., Vienna (Geneva, E.P.S., 2000).

[11] *Ionization profile monitor tests in the SPS*, C. Fischer, J. Koopman, Proc. European article Accelerator Conf., Vienna, 2000, CERN-SL-99-046 BI (2000).

[12] LHC design report, Vol. I, CERN-2004-003.

[13] The LHC 450 GeV to 7 TeV synchrotron radiation profile monitor using a superconducting undulator, R. Jung, P. Komorowski, L. Ponce, D. Tommasini, CERN-SL-2002-015 B1.

[14] *Monitoring lead ion beams in the LHC using a short period SC undulator and BSRT*, R. Jung, CERN internal note, EDMS number 653588.

[15] *Sensors for transverse beam profile monitoring using the SR generated in the LHC BSRT*, R. Jung, CERN internal note, EDMS number 653586.

Chapter 2

[1] *Imphys internet site*, http://www.imphyalloys.com/information_technique/propriete_produit/index.c.3.lng.en.id_categorie.1.html

[2] Opera 3D, TOSCA, Software for Electromagnetic Design, Workstation, version 10.509, Size 3, Vector Fields Ltd., Oxford, England, Vector Fields Inc., Illinois, USA.

[3] *Electromagnetic Design Study of the 5 T Superconducting Undulator for the Proton Synchrotron Light Source and LHC Beam Diagnostics*, P.A. Komorowsky, Cern Technical note 2002-01.

[4] *ZGOUBI user's guide*, F. Méot, S. Valero, DSM/DAPNIA/SEA-01-13, September 2001.

Chapter 3

[1] *An experimental 11.5 T Nb_3Sn LHC type of dipole magnet*, A. den Ouden, S. Wessel, E. Krooshoop, R. Dubbeldam and H.H.J. ten Kate, IEEE Trans. Magn., Vol. 30 No. 4, (1994), pp. 2320–2323.

[2] *Quench characteristics of the 11 T Nb_3Sn model dipole magnet MSUT*, A. den Ouden, H. ten Kate, A. Siemko, P. Sievers, and L. Walckiers, In L. Lianghzhen, S. Guoliao and Y. Lugang (eds.), Proc. of 15th International Conference on Magnet Technology (MT 15), Beijing, China: Science Press, pp. 339–342, 1998.

[3] *HD1: design and fabrication of a 16 Tesla Nb_3Sn dipole magnet*, A.R. Hafalia, S.E. Bartlett, S. Caspi, L. Chiesa, D.R. Dietderich, P. Ferracin, M. Goli, S.A. Gourlay, C.R. Hannaford, H. Higley, A.F. Lietzke, N. Liggins, S. Mattafirri, A.D. McInturff, M. Nyman, G.L. Sabbi, R.M. Scanlan and J. Swanson, Proceedings of the 18th International Conference on Magnet Technology (MT18), Morioka, Japan, October 20-24. 2003.

[4] *Test results for HD1, a 16 Tesla Nb_3Sn dipole magnet*, A.F. Lietzke, S. Bartlett, P. Bish, S. Caspi, L. Chiesa, D. Dietderich, P. Ferracin, S.A. Gourlay, M. Goli, R.R. Hafalia, H. Higley, R. Hannaford, W. Lau, N. Liggens, S. Mattafirri, A. McInturff, M. Nyman, G. Sabbi, R. Scanlan and J. Swanson, Proceedings of the 18th International Conference on Magnet Technology (MT18), Morioka, Japan, October 20-24. 2003.

[5] D. B. Smathers, T. W. C. Albany, Metals handbook, Vol. 2, 10th editon (Properties and Selection), ASM International.

[6] *Limits to Performance of Practical Superconductors*, David Larbalestier, MAS Seminar, CERN.

[7] *Multifilamentary niobium tin magnet conductors*, D.C. Larbalestier, P.E. Madsen, J.A. Lee, M.N. Wilson and J.P. Charlesworth, IEEE Trans. Magn., Vol. MAG-11 No. 2 (1975), pp. 247–250.

[8] *Multifilamentary niobium tin magnet conductors*, D.C. Larbalestier, P.E. Madsen, J.A. Lee, M.N. Wilson and J.P. Charlesworth, IEEE Trans. Magn., Vol. MAG-11 No. 2 (1975), pp. 247–250.

[9] *Composite conductors containing many filaments of Nb_3Sn*, E. Gregory, W.G. Marancik and F.T. Ormand, "," IEEE Trans. Magn., Vol. MAG-11 No. 2 (1975), pp. 295–298.

[10] *Characterization of vanadium diffusion barriers in Nb-Sn composite wires,* D.B. Smathers, P.M. O'Larey, M.B. Sidall and J.R. Peterson, IEEE Trans. Magn., Vol. MAG-23 No. 2 (1987), pp. 1347–1350.

[11] *Improved superconducting critical current density in Modified Jelly Roll Nb_3Sn by the application of niobium (Nb) diffusion barriers*, J.C. McKinnel, D.B. Smathers, M.B. Siddal and P.M. O'Larey, IEEE Trans. Appl. Supercond., Vol. 5 No. 2 (1995), pp. 1768–1772.

[12] Internet site
http://www2.umist.ac.uk/material/research/intmic/phase/cusndiag.htm

[13] *Improvement of critical current density in the bronze-processed Nb_3Sn superconductor*, T. Miyazaki, N. Matsukura, T. Miyatake, M. Shimada, K. Takabatake, K. Itoh, T. Kiyoshi, A. Sato, K. Inoue and H. Wada, Adv. Cryog. Eng. (Materials), Vol. 44(B) (1998), pp. 943–950.

[14] *Very high critical current density of bronze processed (Nb,Ti)3Sn superconducting wire*, H. Sakamoto, M. Higuchi, S. Endoh, A. Kimura, K. Wada, S Meguro and M. Ikeda, IEEE Trans. Appl. Supercond., Vol. 10 No. 1 (2000), pp. 971–774.

[15] Oxford Instruments Technology internet site.

[16] *Method for producing multifilamentary niobium-tin superconductor*, G.W. Marancik, S. Hong and R. Zhou, US Patent No. 5,534,219—filed May 27, 1994, awarded July 9, 1996.

[17] *Composite construction process and superconductor produced thereby*, W.K. McDonald, US Patent No. 4,262,412—filed May 29, 1979, awarded April 21, 1981.

[18] *Internal tin Nb_3Sn conductor development for high energy physics applications* E. Gregory and T. Pyon, Adv. Cryog. Eng. (Materials), Vol. 48(B), pp. 958–967 (2002).

[19] *High field Nb_3Sn conductor development at Oxford Superconducting Technology*, J.A. Parrell, Y. Zhang, M.B. Field, P. Cisek and S. Hong, IEEE Trans. Appl. Supercond., Vol. 13 No. 2 (2003), pp. 3470–3473.

[20] *Composite construction process and superconductor produced thereby*, W.K. McDonald, US Patent No. 4,262,412—filed May 29, 1979, awarded April 21 1981.

[21] *Manufacture and evaluation of Nb_3Sn conductors fabricated by the MJR method* W.K. McDonald, C.W. Curtis, R.M. Scanlan, D.C. Larbalestier, K. Marken, and D.B. Smathers, IEEE Trans. Magn., Vol. MAG-19 No. 3 (1983), pp. 1124–1127.

[22] *Progress with Nb_3Sn conductors at Oxford Instruments, Superconducting Technology*, M. Field, R. Hentges, J. Parell, Y. Zhang and S. Hong, IEEE Trans. Appl. Supercond., Vol. 11 No. 1 (2001), pp. 3692–3695.

[23] *Status of the superconductor development program at Teledyne Wah Chang Albany*, D.B. Smathers, P.M. O'Larey, M. Sidall and W. McDonald, Adv. Cryog. Eng. (Materials), Vol. 34 (1988), pp. 515–522.

[24] *High field Nb_3Sn conductor development at Oxford Superconducting Technology*, J.A. Parrell, Y. Zhang, M.B. Field, P. Cisek and S. Hong, IEEE Trans. Appl. Supercond., Vol. 13 No. 2 (2003), pp. 3470–3473.

[25] *Irreversibility field and critical current density as a function of heat treatment and temperature for a pure niobium powder-in-tube Nb_3Sn conductor*, C. M. Fischer, P. J. Lee and D. C. Larbalestier, accessible from http://www.asc.wisc.edu/

[26] *Progress in the development of an 88-mm-bore 10 T Nb_3Sn dipole magnet*, A. den Ouden, W.A.J. Wessel, G.A. Kirby, T. Taylor, N. Siegel and H.H.J. ten Kate, IEEE Trans. Appl. Supercond., Vol. 11 No. 1 (2001), pp. 2268–2271.

[27] *Investigation of the Relationships Between Superconducting Properties and Nb_3Sn Reaction Conditions in Powder-in-Tube Nb_3Sn Conductors*, C.M. Fischer, M.S. thesis, Univ. of Wisconsin, Madison WI, USA (2002).

[28] *Kinetics of phase growth during the Cu-Sn diffusion process and the Nb_3Sn formation.Optimization of superconducting properties*, Sara Mattafirri, Degree thesis, Universita' degli Studi di Pisa, 2002.

[28] *Insulation systems for Nb_3Sn accelerator magnet coils fabricated by the wind & react technique*, A. Devred, P. Bredy et al., Adv. Cryo. Eng. (Materials), Vol. 46 (2000), pp. 143-150.

[29] *Characterization of bulk and multifilamentary Nb_3Sn and Nb_3Al by diffractometric and resistive measurements*, R. Flükiger, W. Goldacker and R. Isernhagen, "," Adv. Cryog. Eng. (Materials), Vol. 32 (1985), pp. 925–936.

[30] *Observations related to the order of the low temperature structural transformation in V3Si and Nb_3Sn*, R. Mailfert, B.W. Batterman and J.J. Hanak, Phys. Stat. Sol., Vol. 32 (1969), pp. K67–K79.

[31] *Phase transition and superconducting properties of binary and Ti, Ta, Ga and H alloyed Nb_3Sn*, W. Goldacker and R. Flükiger, "," *Physica*, Vol. 135B (1985), pp. 359–363.

[32] *High-field superconducting properties of the composite processed Nb_3Sn with Nb-Ti cores*, K. Tachikawa, T. Asano and T. Takeuchi, "," Appl. Phys. Lett., Vol. 39 (1981) No. 9, pp. 766–768.

[33] *Composite processed Nb_3Sn with titanium addition to the matrix*, K. Tachikawa, H. Sekine and Y. Iijima, "," J. Appl. Phys., Vol. 53 No. 7 (1982), pp. 5354–5356.

[34] *Study of the React and Wind Technique for a Nb_3Sn Common Coil Dipole*, G. Ambrosio, N. Andreev, E. Barzi, P. Bauer, D. Dietderich, K. Ewald, J. Ozelis, G. Sabbi.

[35] *Experimental and theoretical studies of filamentary superconducting composites*, M. N. Wilson, C. R. Walters, J. D. Lewin and P. F. Smith, J. Phys. Appl. Phys., Vol. 3 (1970).

[36] *Stability against flux jumping in sintered Nb_3Sn*, R. Hancox, Physics Letters, Vol. 16, num. 3, pp. 208-209 (1965).

[37] *Enthalpy stabilized superconducting magnets*, R. Hancox, IEEE Transactions on magnets, Vol. Mag. 4, num. 3 (1968).

[38] *Performance boundaries in Nb_3Sn superconductors*, Arno Godeke, PhD Thesis Twente University.

[39] *Superconducting magnets*, M. N. Wilson, Clarendon Press Oxford (1983).

[40] Practical low-temperature superconductors for electromagnets, A. Devred, CERN-2004-006.

Chapter 4

[1] *High field Nb_3Sn conductor development at Oxford Superconducting Technology,* J. Parrell, Y. Zhang, M. B. Field, P. Cisek, S. Hong, IEEE Transactions on Applied Superconductivity, Vol. 13, No. 2, June 2003.

[2] *Kinetics of phase growth during the Cu-Sn diffusion process and the Nb_3Sn formation.Optimization of superconducting properties*, Sara Mattafirri, Degree thesis, Universita' degli Studi di Pisa, 2002.

[3] L.T. Summers, M.W. Guinan, J.R. Miller, P.A. Hahn, *A model for the prediction of Nb_3Sn critical current as a function of field, temperature, strain and radiation damage,* IEEE Trans. Magn., vol. 27 (2), p. 2041-2044 (1991).

[4] *Sumimoto's Nb3Al Jc measurements at the sjort sample tests facility*, E. Barzi, TD-99-004, January 25 1999.

[5] *Electric and magnetic properties of CuSn and CuNi alloys at 4 K,* F. R. Fickett, Cryogenics, vol. 22, p. 135 (1982).

[6] *Oxigen-free copper at 4 K: resistance and magnetoresistance*, F. R. Fickett, IEEE Transactions on magnetics, vol. mag-19, no 3, (1983).

[7] *Test facility for critical current measurement*, Magnet Oxford Instruments, Charles Henri Denarié.

[8] *Magnetization and stability measurements*, M. N. Wilson and C.R. Walters, J. Phys. D: Appl. Phys., vol. 13, p. 1547-1561 (1970).

[9] Nota LASA

[10] *Magnetization of high-Jc Nb_3Sn strands*, D. Turrioni, E. Barzi, M. Bossert, V.V. Kashikhin, A.V. Zlobin

[11] *Effect of temperature and deformation on Nb_3Sn strands instabilities*, E. Barzi, L. Del Frate, D. Turrioni, V. V. Kashikhin A.V. Zlobin

[12] *Studies of Electromagnetic Instabilities in Nb_3Sn Strands and Cables*, Emanuela Barzi, Giorgio Ambrosio, Nicolai Andreev, Licia Del Frate, Vadim V. Kashikhin, Daniele Turrioni, Ryuji Yamada, Alexander V. Zlobin, MT 19 Proceedings, Genova-Italy (2005).

[13] *Investigation of Instability in High Jc Nb_3Sn Strands*, A. K. Ghosh, L. D. Cooley, and A. R Moodenbaugh.

[14] *Dynamic stability threshold in high-performance internal-tin Nb_3Sn superconductors for high field magnets*, AKGhosh1, EA Sperry1, L D Cooley2, A M Moodenbaugh, R L Sabatini and J L Wright, Supercond. Sci. Technol. 18 (2005).

[15] *Measurement of critical current and instability threshold of Rutherford-type Nb_3Sn cables*, G. Ambrosio, N. Andreev, E. Barzi, B. Bordini, C-H Denarie, S. Feher, V. Kashikhin, A. Verweij, A.V. Zlobin, MT 19 Proceedings, Genova-Italy (2005).

Chapter 5

[1] *Manufacture and Test of the Prototype 5T Superconducting Undulator for the LHCSynchrotron Radiation Profile Monitor*, R. Maccaferri, S. Bettoni, D. Tommasini, W. Venturini Delsolaro, MT 19 Proceedings, Genova-Italy (2005).

[2] Internet site http://www.ctd-materials.com/products/electricalins.htm

[3] *Effect of temperature and deformation on Nb_3Sn strands instabilities,* E. Barzi, L. Del Frate, D. Turrioni, V. V. Kashikhin A.V. Zlobin, CEC05 Proceedings.

Appendix A

[1] M. N. Wilson, Superconducting magnets, Oxford Science Publications.

[2] L. Dresner, Stability of Superconductors, Plenung Publishing Corporation, 1985.

[3] About the propagation velocity in superconducting composites, B. Turck, Cryogenics (1980).

[4] Numerical recipes, W. H. Press, B. P. Flannery, W. T. Vetterling, Cambridge.

[5] *Material properties for quench simulation (Cu, NbTi and Nb_3Sn),* Seog-Whan Kim, , FermiLab TD Note 00-041.

[6] Internet site http://www.cryogenics.nist.gov/

[7] *Thermal conductivity of Nb_3Sn*, G. D. Cody and R. W. Cohen, RCA Laboratories, Priceton, New Jersey.

Appendix B

[1] Internet site http://www.cat.ernet.in/technology/accel/atdhome.html

Appendix C

[1] *Nonlinear dynamics in SPEAR wiggler,* J. Safranek, C. Limborg, and A. Terebilo, K. I. Blomqvist Danfysik, P. Elleaume, Y. Nosochkov, Physical review special topics, accelerators and beams, volume 5, 010701 (2002).

[2] *Effects of nonlinear terms in the wiggler of the magnets at DAΦNE*, C. Milardi, D. Alesini, G. Benedetti, S. Bertolucci, C. Biscari, M. Boscolo, S. Di Mitri, G. Di Pirro, A. Drago, A. Ghigo, S. Guiducci, G. Mazzitelli, M. A. Preger, F. Sannibale, A.

Stecchi, C. Vaccarezza, M. Zobov, P. Raimondi, E. A. Perevedentsev, Proceedings of the 2001 Particle Accelerator Conference, Chicago.

[3] *The modified wiggler of the DAΦNE main rings*, A. Battisti, S. Bertolucci, B. Bolli, S. Ceravolo, M. Incurvati, F. Iungo, M. Paris, M. Preger, P. Raimondi, C. Sanelli, F. Sardone, F. Sgamma, M. Troiani, DAΦNE Technical note MM-34 (7th January 2004).

[4] Opera 3D, TOSCA, Software for Electromagnetic Design, Workstation, version 10.509, Size 3, Vector Fields Ltd., Oxford, England, Vector Fields Inc., Illinois, USA.